DTU Library

Modular Underwater Robots - Modeling and Docking Control

Nielsen, Mikkel Cornelius

Publication date:
2018

Document Version
Publisher's PDF, also known as Version of record

Link back to DTU Orbit

Citation (APA):
Nielsen, M. C. (2018). Modular Underwater Robots - Modeling and Docking Control. Technical University of Denmark, Department of Electrical Engineering.

Mikkel Cornelius Nielsen

Modular Underwater Robots - Modeling and Docking Control

Thesis for the joint degree of philosophiae doctor at NTNU and DTU
Trondheim and Lyngby, March 2018

Norwegian University of Science and Technology
Faculty of Information Technology and Electrical Engineering
Department of Engineering Cybernetics

Technical University of Denmark
Department of Electrical Engineering
Automation and Control Group

NTNU
Norwegian University of
Science and Technology

Technical University
of Denmark

DTU

Thesis for the joint degree of philosophiae doctor at NTNU and DTU

Consider yourself fortunate if in the midst of such a whirlwind,
you possess a guiding intelligence within yourself
- Meditations (XII, 14, 4)

Summary

The objective of this thesis is to investigate the modeling and control of modular underwater robots. This objective is motivated by recent events in the offshore industry, where innovative solutions are needed to cope with the upcoming challenges. The vision is to use small-sized modular underwater robots to inspect all areas of offshore structures efficiently, but at the same time maintain the capacity for intervention through morphological changes in the system.

This thesis concerns itself with modeling and docking control of a system composed of modular underwater robots. The first part of the thesis consists of five chapters, which combined investigates the mathematical modeling of a system of modular underwater robots with arbitrary interconnection between them. The first chapter presents the kinematics, the marine vehicle models, and the notation. An essential feature of a Modular Underwater Robot (MUR) system is the ability to reconfigure the morphology of the interconnection. Thereby, the underlying modeling methodology must handle structural changes in the system. The second chapter of the first part introduces different modeling approaches with examples before presenting the chosen modeling approach. Furthermore, the chapter develops a model for the MUR system into a simulator and verifies the implementation by a numerical investigation.

Any dynamic model suffers from imperfect model knowledge, and aggregating multiple models into a large-scale model only magnifies the effect. The subsequent chapter of Part I validates the developed modeling approach by subjecting multibody systems to different experiments. The chapters compare the behavior of the real and the simulated system, respectively, and seeks to quantify the concordance between them.

The automatic modeling method, developed in the first part of the thesis, applies when the MUR gather into a morphology. The second part of this thesis concerns with the MUR system before the aggregation of the MURs. The aggregation of the MURs require them to approach each other, called *Rendezvous*, and then, physically connect to each other, called *docking*. The considered rendezvous and docking problem is assumed to be camera-based, such that, the navigation of the systems utilize cameras for position estimation. The camera introduces line-of-sight conditions that must be kept. Part II proposes to employ distributed predictive control for solving the camera-based rendezvous and docking problem. The predictive controller is capable of embedding the line-of-sight constraint directly in the formulation, while synchronizing the rendezvous pose between the vehicles.

Contents

List of figures

List of tables

List of Acronyms and Abbreviations

ASV Autonomous Surface Vessel

AUV Autonomous Underwater Vehicle

BEM Boundary Element Method

CFD Computational Fluid Dynamics

CoB center of buoyancy

CoM center of mass

DAE Differential Algebraic Equation

DAQ Data Acquisition

DMPC Distributed Model Predictive Control

DOF Degree of Freedom

DP Dynamic Positioning

DTU Technical University of Denmark

DTW Dynamic Time Warping

ECEF Earth-Centered-Earth-Fixed

ECI Earth-Centered-Inertial

ESC Electronic-Speed-Controller

I^{2}C Inter-Integrated Circuit

I-AUV Intervention AUV

IMR Inspection, Maintenance and Repair

ITTC International Towing Tank Conference

KF Kalman Filter

LOS Line-of-Sight

MCLAB Marine Cybernetics Laboratory

MIMO Multiple-Input-Multiple-Output

MPC Model Predictive Control

MSE Mean Square Error

MUR Modular Underwater Robot

NED North-East-Down

NTNU Norwegian University of Science and Technology

NTP Network Time Protocol

ODE Ordinary Differential Equation

PID Proportional-Integral-Derivative

PMM Planar-Motion-Mechanism

PWM Pulse-Width-Modulation

ROS Robot-Operating-System

ROV Remotely Operated Vehicle

RPM Revolutions-Per-Minute

RPS Revolutions-Per-Second

SNAME Society of Naval Architects and Marine Engineers

SVD Singular Value Decomposition

UVMS Underwater Vehicle-Manipulator Systems

WLS Weighted-Least-Squares

Preface

This thesis is submitted in partial fulfillment of the requirements for the degree of philosophiae doctor (PhD) at the Norwegian University of Science and Technology (NTNU). My doctoral study was conducted at the Centre for Autonomous Marine Systems and Operations (NTNU AMOS) at the Department of Engineering Cybernetics (ITK) in the period from August 2014 to March 2018. Funding was provided by the Research Council of Norway through the Centres of Excellence funding scheme, Project number 223254. My supervisors has been Professors Mogens Blanke, and Ingrid Schjølberg.

Acknowledgments

When I saw the opportunity to engage in a Ph.D. at NTNU AMOS, it was almost an instantaneous decision to apply for it. It is safe to say, that the decision has been questioned by myself on multiple occasions since. The last four years have both professionally and personally been an intense and often perilous journey.

Despite the frustrations on the way and perhaps because of them, I have learned much, both technically but especially on a personal level. For that, I would like to thank my supervisor Professor Mogens Blanke for giving me the opportunity to challenge and develop myself. I am confident that the knowledge will translate into success in the years to come.

Furthermore, I want to thank my co-supervisor Professor Ingrid Schjølberg for inspiring hope when prospects seemed dismal. I also want to thank Professor Tor Arne Johansen for his resourceful inputs and guidance which helped tremendously during the project.

During my time as a Ph.D. I was fortunate to encounter many people without whom this project would have found a different end. These people have helped me overcome many challenges over the course of my Ph.D., and for that, I am truly grateful.

I first moved to Trondheim in August of 2014, and incidentally, it would seem most of Norway did the very same thing. I want to thank Jakob Mahler Hansen, Kasper Trolle Borup, Kim Lynge Sørensen, and Signe Moe of the infamous *Danish Asylum* for housing me for the first year, and for providing a base of support without which this journey would not have made it as far as it did.

I am grateful for my office mates Albert Sans Muntadas and Signe Moe. It has been a privilege to share an office with them. I also want to thank Bård Nagy Stovner for always finding time to help me when I was stuck.

The social life at NTNU AMOS was very diverse, and many different topics were discussed during the coffee breaks at the Tyholt kitchen. Thanks to Erlend Kvinge Jørgensen, Claudio Paliotta, and Dennis Belletter for many useful and often political incorrect discussions in the Tyholt kitchen. A special thanks to Claudio and Dennis for saving me from myself during my weekly brainstorm meltdowns. Ph.D. life is often all consuming, and therefore, I want to thank Anna Kohl and Konstanze Kölle for planning ski-trips to both Oppdal and Åre and, by extension, reinforcing my preconceived idea of the German stereotype.

My project was part of a newly established joint degree program between NTNU and DTU, and as such, I spend one year at DTU from summer 2015 to summer 2016. During my time at DTU, I had the pleasure of many good discussions with my friends Dimitrios Papageorgiou and Nicholas Hansen, who provided helpful inputs over the course of my project.

I would like to thank Kristian Klausen for introducing me to the Udwadia-Kalaba Formulation, and for being a superb roommate on my second stay in Trondheim.

The thesis contains a lot of experimental data, and fortunately, I had help in conducting the experiments. I would like to thank Glenn Angell for your fast support and Torgeir Wahl for his support during the trails in MCLAB.

I had the fortune to work alongside Andreas Baldur Hansen in MCLAB during July of 2016. Many engineering solutions were invented during those two weeks.

I further want to thank Ole Alexander Eidsvik for your help with the towing tank tests for identification of the BlueROV, as well as, for conducting the necessary CFD analyses for all my experiments.

Experimental data can be treacherous to interpret, and I would like to thank Eleni Kelasidi for your candid opinion on numerous tough questions.

Moving to another country inevitably puts pressure on established friendships and, therefore, I would like to thank my friends for always finding time to meet when I am in Denmark.

I spent my year in Denmark living with my mother, Lene, and I feel, despite the difficulties I faced in the project, that both of us gained something positive from the experiment. Thank you for your love, encouragement, and support.

To my sister, Mette-Marie, thank you for inviting me to participate in your tournaments around the world, and for your cheer and affection.

To my father, Christer, for your encouragements and support.

Finally, a thanks to all my colleagues, named and unnamed, for all the exciting events and coffee breaks.

Chapter 1

Introduction

1.1 Background and Motivation

Autonomy in the offshore sector is projected to increase rapidly as a result of attempts to, reduce cost, ensure safety and improve production, while continuously expanding into increasingly hostile environments. The future subsea facilities are expected to be located at deeper, colder and more remote locations [75]. The facilities are subject to the harsh conditions of the open ocean. Furthermore, the remote location complicates the logistics and increases the cost of employing surface support vessels.

The current generation of offshore facilities and infrastructures are aging, and the requirement for maintenance and repair is increasing. Todays IMR technology is already struggling to keep up with the performance demands of the industry while maintaining safety and cost levels. The challenges to IMR are many since it involves both safety and cost of personnel, equipment, and environment. These challenges expand into diverse practical problems ranging from corrosion of the structure to logistics of the life-support systems. The annual expenditure for handling the corrosion alone is estimated to be more than 26 billion US Dollars in the United States alone [162] and more than 200 million Danish kroner in Denmark [178].
Today, manually controlled ROVs provide a standard platform for IMR. The ROV technology require manned surface supply vessels in Dynamic Positioning (DP) mode during operations. Safety regulations demand facilities to cease production during ongoing inspections, and thereby adding to the expenditure of the inspection tasks.

The pilots controlling the ROVs inside, and in the vicinity of a subsea facility must navigate in an environment affected by biofouling. The biofouling causes increased hydrodynamic load and metal fatigue in the structures, which accelerates the development of damages, and hides occurrences of these [90, 51]. As industry and legislators have become increasingly aware of the environmental effects associated with usage of chemical agents to counteract biofouling, mechanical solutions, such as pigging has become contenders [169].

Continuous, and consistent quality inspection data is key to synthesizing prognosis models for condition monitoring of subsea facilities [137, 142, 227]. Manually
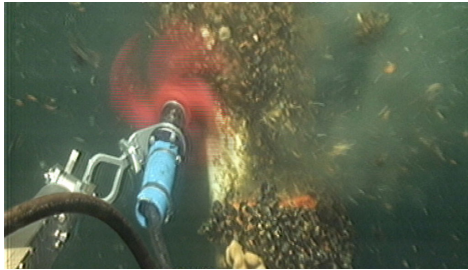
(a) Remotely Operated Vehicle (ROV) mounted mechanical anti-fouling device removing biofouling from pipe.
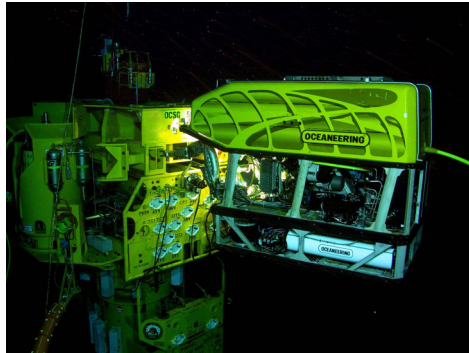
(b) Intervention ROV interacting with a subsea christmas tree.

Figure 1.1: The current subsea intervention technology applied by the industry to conduct IMR on offshore structures. Biofouling is a particular area of interest as the fouling accelerates metal fatigue, and changes the hydrodynamic characteristics of the platform.

controlled inspection impedes the consistency and quality of collected data, and automatic solutions are preferable. Furthermore, reliance on surface support vessels and human operators comes with risk for both deck personnel who handle the ROV and the equipment itself, as accidents most commonly occur during deployment and retrieval of the vehicle [220, 219].

1.1.1 Inspection, Maintenance and Repair (IMR)

The field of IMR has received an increasing focus from around the start of the new millennium. A particularly difficult topic is the study of Underwater Vehicle-Manipulator Systems (UVMS), where interaction between manipulator arm and vehicle is crucial for the precise control of the end-effector pose. The first literature focused on perfect feedback, under the assumption of known dynamic parameters of the arms and vehicles [200]. However, accurate knowledge of dynamic parameters for underwater vehicles and manipulators are tenuous in most realistic cases. In response, researchers explored adaptive control schemes to compensate for the lacking model knowledge [7, 10].

The UVMS always contains redundant Degree of Freedom (DOF)s due to the free motion of the vehicle and exploiting the redundancies using null-space based methods for force control [6], and task-priority management [9].

Multiple larger projects have investigated IMR operations using UVMS.

The RAUVI project was a three-year project spanning from 2009 to 2011. The goal of the project was to develop technology for autonomously performing intervention missions in underwater environments [42]. The project combined a reconfigurable AUV with a 4-DOF manipulator and introduced different control strategies for the interconnection between vehicle and manipulator [152, 195]. The RAUVI project showed successfully results with the localization and retrieval of the black

box from a flight [177, 176].

The TRIDENT project was also a three-year program starting in 2010 and ending in 2012. The project focused on cooperation between an Autonomous Surface Vessel (ASV), and an Intervention AUV (I-AUV) equipped with a multipurpose dexterous manipulator for intervention missions in unstructured and underwater environments [197, 196].

The TRITON project was a natural evolution of the RAUVI and TRIDENT project. The timeline was from 2012 to 2014. The focus of the project was on intervention in structured environments, such as docking and interaction with a subsea panel. The project produced an open-source simulator environment UWSIM [175]. Furthermore, the project managed to dock an I-AUV with a subsea panel, and perform valve turning [153].

The PANDORA project was a European FP7 project running between 2012 and 2014. The goal of PANDORA was to increase autonomy for I-AUVs in structured subsea environments. The autonomy was designed to ensure that failures were detected and handled appropriately [116]. The success metrics of the project were the vehicle's capability for IMR by inspecting, cleaning, and turning valves [154, 131].

The MARIS project was a multi-objective subsea intervention project. The topics
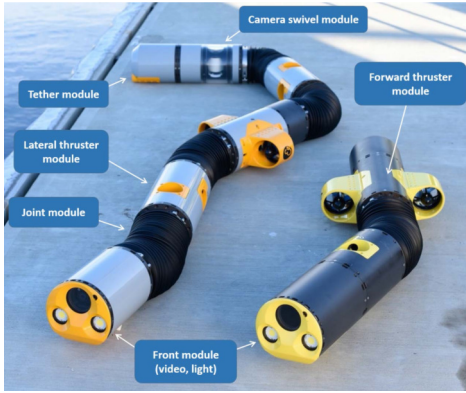
(a) The Underwater Swimming Manipulator concept *Eelume*. Courtesy of [123].
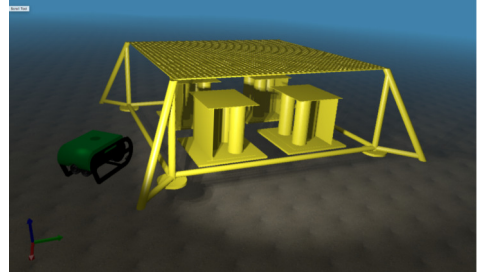
(b) Screenshot from the UWMORSE simulator of the NextGenIMR project. Courtesy of [79].

Figure 1.2: The NTNU initiatives into IMR research.

of the project were dexterous manipulation using multi-DOF manipulators and using multiple vehicles. The project started in 2013 and ended in 2016 [33, 34]. The results of the project were significant improvements to the control framework, the manipulation performance, and the visual navigation systems compared with former projects [202].

The MORPH project was a European framework 7 project [92]. The project started in 2012 and ended in 2016 [94]. The goal of the project was to enhance inspection and mapping of both complex structured and unstructured underwater environment using multiple heterogeneous Autonomous Underwater Vehicle (AUV)s. An interesting aspect of the project was the idea, that the sensor payload of each vehicle could compliment each other to obtain better navigation and mapping perfor-

mance. The project developed a leader-follower style formation control architecture with special focus on communication under severe restrictions [**Abreau2016**, 2, 3]. The resulting vehicle formation was denoted a MORPH Supra-Vehicle, which could reconfigure itself depending on the tasks. The project successfully demonstrated the concept using eight vehicles, seven underwater and one surface vessel), to map an environment [93].

Finally, the DEXROV project is a horizon 2020 project. The project seeks to reduce the burden of conducting intervention missions at offshore locations by tele-operating the ROV from locations on shore [65, 66] while maintaining advanced dexterous manipulation capabilities. The challenge is to maintain performance in the inevitable presence of latency. The proposed solution is to enable a higher level of autonomy on both sides of the control, such that, the communication can be severely reduced [46].

NTNU has approached research on IMR from multiple perspectives. The NextGen-IMR project focused on autonomy in IMR operations [201]. The project kept the pilot-in-the-loop as a supervisor during the mission. The human-machine interaction for IMR operations was explored in Henriksen, Schjølberg, and Gjersvik [78], where pilot fatigue was mitigated by automating parts of the motion control tasks. The project also produced a simulation environment *UW Morse Simulator*, to simulate ROV operations [79]. Fig. 1.2b shows a screenshot from the simulator.

Much of the literature focuses on developing conventional ROVs and AUVs. Standard form Intervention-ROVs comprises of a bulky hull, which in turn, limits the ability to enter specific areas in an offshore structure.

The bioinspired underwater swimming manipulator overcomes the challenges of confined space inspections [212, 213]. Fig. 1.2a shows two configurations of the modular underwater multi-link manipulators. The vehicle is constructed from a series of links with actuation. The hyper-redundancy from the multi-link composition allows for inherent fault-tolerance with low drag forces and accessibility to every place on the subsea structure [123].

1.1.2   The Siri Platform Case

Events in the offshore industry were among the sources of inspiration behind this thesis. The Siri Jacket Platform is located in the Danish part of the North Sea.

Cracks were discovered in the Sponson on the gravity base of the jacket construction support the Caisson of the wellhead during a regular maintenance inspection in August 2009. Fig. 1.3a shows the subsea Sponson extruded on the side of the oil storage compartment. The production ceased immediately upon discovery and remained out of operation for five months before a temporary engineering solution allowed the production to continue. A subsequent inspection, conducted in July 2013, discovered additional cracks in the same Sponson, but this time compromising the integrity of the subsea oil storage compartment. The discovery ceased production on Siri for another six months. In both cases, IMR activities increased to ensure that no further damages had developed. By the account of the pilots conducting the inspections, the environment was difficult to navigate due to obscuring of the structure by biofouling. Furthermore, the intervention tasks conducted to stop further development of the cracks were delicate and complicated due to con-

fined operational space within the interior of the storage tank. Fig. 1.3b shows the Sponson with the interior. The interior of the Sponson is cluttered with support beams and therefor difficult to navigate. The intervention was an ad-hoc solution. A small sized ROV was carrying a subsea power-drill, which obscured the visual feed on the ROV, and required another smaller observation class ROV to act as third-party eyes for navigation through the subsea structure. The ad-hoc intervention solution entailed a significant risk of equipment loss, and significant time was spent on IMR operations. Thereby, the Siri platform represents a case, where the current generation of IMR technology was pushed to the it's limits, and beyond. In

(a) Underwater sponson, and oil storage compartment of Siri.

(b) The sponson compartment with elements of the interior shown. The cluttered interior complicates the navigation inside the sponson.
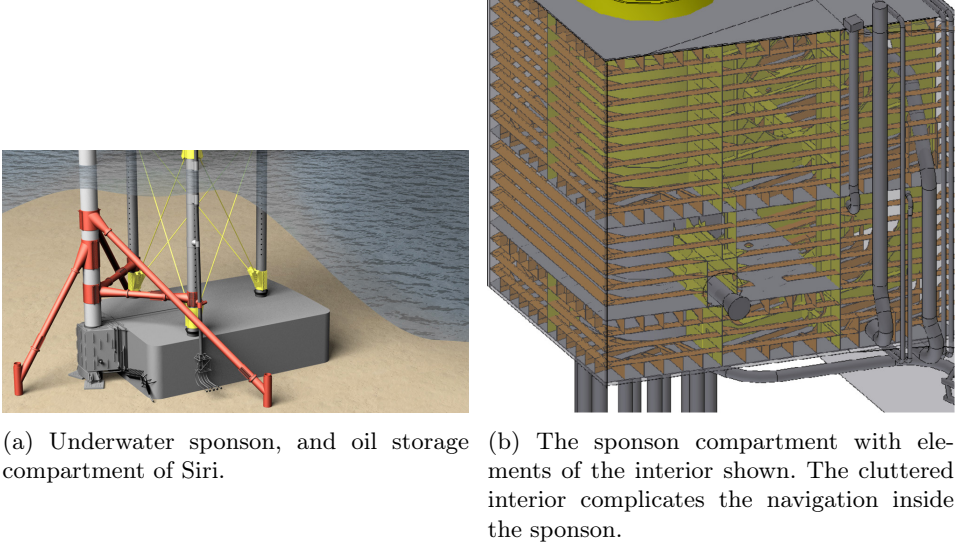
Figure 1.3: The Siri Sponson compartment is located at 65 meters depth.

short, inspection data is critical for condition monitoring, but quality data is difficult to obtain with current IMR technology. Requirements for intervention tasks, such as, maintenance and repair, increases as current generation subsea facilities are aging, and next generation subsea facilities are constructed.

The REMORA project from Technical University of Denmark (DTU) takes inspiration from the events at Siri to propose a different direction of research [38]. The project envisions to employ a swarm of small, and tightly cooperating ROVs for IMR. The reasoning behind the small-sized and tightly cooperating vehicles comes directly from the challenges at the Siri platform, where regular sized ROVs experienced significant difficulty in operating inside the confined space of the Sponson.

The REMORA system is composed of small size modular vehicles with connection capabilities. Individual vehicles can have different instrumentation and actuation. The REMORA concept, hence, comprise of modules with heterogeneous abilities. Fig. 1.4 depicts two cases envisioned for the modular system. Fig. 1.4b shows a ROV deploying a crawler-type vehicle on the hull of the structure. The

vehicles act in concert to different tasks, such as transportation of objects, inspection, and intervention. The connectivity capabilities allow the vehicles to aggregate into larger vehicles such that the systems Fig. 1.4a
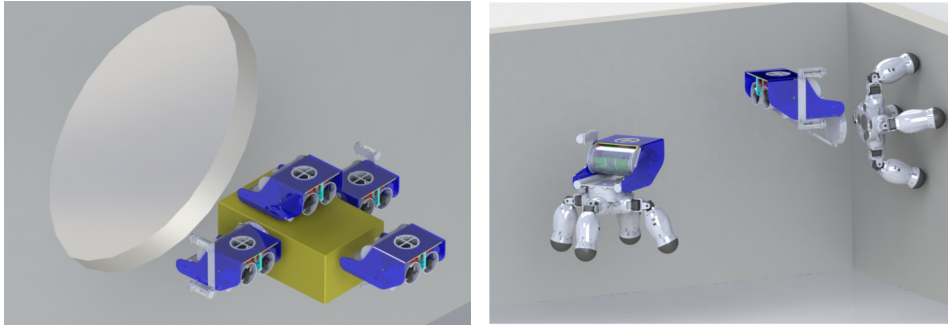
(a) A possible configuration for the modular underwater robotic system, 4 vehicles transport an object through an opening.

(b) The modularity allows vehicles with widely different specializations to better solve tasks cooperatively.

Figure 1.4: The modular underwater robotic system cooperates tightly by attaching themselves together to create a larger system with more capabilities.

1.1.3 Modular Underwater Robots

A MUR is a robot capable of attaching and detaching to other MURs. Modular underwater robots, as a concept, provides a series of solutions, which match the problems perceived in the offshore industry. As opposed to the monolithic IMR-ROV currently employed, the modular underwater robots are small, agile, and specialized to specific tasks. The modular underwater robots possess the ability to self-reconfigure, that is to physical interconnect with each other. The resulting collective system aggregates the specializations to amalgamate their capabilities. Thereby, the system adapts to the tasks as they emerge during a mission.

A practical example would be to reconfigure their interconnection physically. The reconfiguration allows the robots to accomplish the same thrust output with different system morphologies. Fig. 1.5 shows a system of modular underwater robots transporting an object. The morphology changes between Fig. 1.5a, and Fig. 1.5b. The situational awareness and thrust capability change with the morphology of the system. Naturally, a system that adapts to unexpected event contains an inherent fault-tolerance. Modular Robots for underwater vehicles have gained increasing interest in the research community and is closely related to the topic of intervention.

Here there exist multiple groups working in different directions, but most interesting for this project is the MIT Distributed Robotics Lab with the AMOUR system presented in [229, 230], where heterogeneous modular robots dock with each other to share collected environmental data. The focus was small, inexpensive modular robots working in unison to achieve tasks in which AUVs, at the time, could not complete individually.
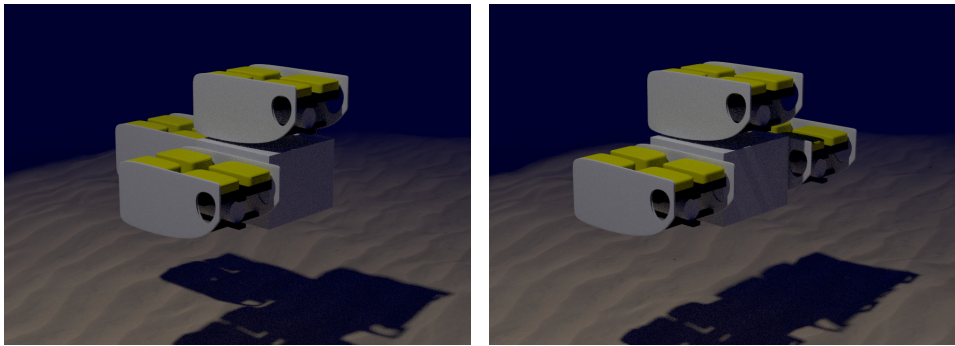
(a) One possible configuration for the modular underwater robotic system.

(b) The vehicle can attach themselves in different positions to produce better thrust capabilities or better utilize individual sensors.

Figure 1.5: The modular underwater robotic system can change configuration depending on the task or on environmental restrictions.

The authors Furno et al. [64] considered self-reconfiguration between multiple ROVs, where the author combined the Theta* algorithm with an energy heuristics to minimize the energy usage in intermediate morphologies during transitions.

Synergy between underwater vehicles and modular robotics is a new field. Stoy, Brandt, and Christensen [209] give a thorough description of the field of modular and self-reconfigurable robots.

1.2 Scope and Objectives

This thesis covers selected topics within the field of Modular Underwater Robotics. A modular underwater robotic system is composed of multiple Modular Underwater Robots. The MURs are connection capable, meaning they can aggregate together and create new systems with different morphology. Given a group of underwater vehicles capable of changing morphology to underwater a new task, automatic control of the cluster should be available to meet the control requirements for the new task and the new morphology.

A new morphology will change the specific dynamic characteristics, as well as, the impact the effect of control forces on the system. Control functionality with prespecified performance requirements must know the behavior of the system and, by extension, the changes to the system behavior due to the morphology.

Research Question 1: Is it feasible to automatically construct a descriptive model of a given morphology for a system composed of Modular Underwater Robots?

This thesis will consider research question 1, to determine model uncertainties that arise due to hydrodynamic phenomena and the general uncertainty that is related to damping, resistance, and validate the modeling approach against model basin tests.

The MURs of the system must physically connect to each other in a given sequence

to form a morphology. The physical connection require that the MURs can rendezvous with each other and subsequently dock. The problem of rendezvous and docking raise the second research question of the thesis,

Research Question 2: How is it possible to conduct rendezvous and docking between multiple vehicles to form a morphology?

This thesis will treat research question 2 considering rendezvous and docking of two MURs, and investigate, how to distribution of control algorithms onto individual vehicles can solve the coordinated control problem of rendezvous and docking of modular robots.

Research questions 1 and 2 are treated in a two-part division of the thesis. Part I investigates research question 1, while Part II considers research question 2.

1.2.1 Modeling of Underwater Multi-Body Systems

The problem of modeling the dynamics of connected vehicles belongs in the category of multi-body dynamics. Specifically, when vehicles connect to each other rigidly, the dynamics of the system changes drastically. Modeling the motion of one vehicle directly influences the motion of the other vehicle through the rigid connection.

This thesis investigates modeling of systems composed of MURs. Since, MUR systems are capable of detaching and reattaching online, the modeling method must be capable of handling structural changes to the system. Multiple Newton-Euler [14], Lagrange's Equations [76], Kane [95, 96], Gibbs-Appell [161], Maggi [112], Udwadia-Kalaba [91] exist for modeling multi-body systems. The authors Bauchau and Laulusa [19] and Laulusa and Bauchau [117] provides an overview of the general topic.

For underwater applications, UVMS constitute a prime example of a multi-body dynamic system in action. Tarn, Shoults, and Yang [217], Tanner and Kyriakopoulos [215], and Yang Ke et al. [240] employs Kane's method for modeling an UVMS. The authors Yang et al. [242] applied Kane's method to model underwater Snake-like robots. Yang et al. [241] modeled a underwater quadruped walking robot using Kane's method.

Evidently, Kane's method is popular for modeling of underwater multi-body systems. The popularity stem, primarily, from the ability to deal with non-trivial constraints using body-fixed velocities. However, Kane's method assumes that the underlying connection between bodies conform to an open-tree topology, and further, requires a root-node in the topology from where the system is derived. Open-tree topology is guaranteed for MUR systems since there are no restrictions on the morphology of the vehicles. Furthermore, derivation from a root-node implies that the model has to be re-derived at every occurring structural change.

Schjølberg and Fossen [200] applied recursive Newton-Euler to model an UVMS system with an n-DOF manipulator, and Santhakumar and Kim [194] used a recursive Newton-Euler to model an UVMS system with a single DOF manipulator. Antonelli, Caccavale, and Chiaverini [7] modeled an UVMS system with an n-DOF manipulator using the Denavit-Hartenberg formalism.

Snake-robots constitute another area where multi-body dynamics provide the framework for modeling. Kelasidi et al. [100] developed a closed-form dynamic model for a snake-robot as a chain of homogeneous interconnected cylinders, and expanded the motion to 3-D in [99]. Kohl et al. [106] applied simplifying assumptions on the model to allow a model tailored for control design. Sverdrup-Thygeson et al. [211] expanded the model with thrusters and heterogeneous sized cylinders. The recursive Newton-Euler and the snake-model require stronger assumptions on the topology, namely that the topology conforms to an open-chain.

To the best of the author's knowledge, no literature exist on the topic of automatic modeling for modular underwater robotic systems. The purpose and contribution of this thesis in regards to research question . is to develop an automatic modeling approach for deriving MUR systems. The automatic modeling constructs an aggregated model based on the morphology of rigidly linked sub-models. Furthermore, the thesis validates the modeling approach through experimental data from model basin tests.

1.2.2 Rendezvous and Docking for Underwater Applications

The rendezvous and docking literature predominantly considers docking for torpedo-shaped AUVs with respect to stationary funnel-type docking stations. In early literature the task of an AUV was primarily long distance subsea-floor surveys and, naturally, the desire for automatic battery recharge lead much of the focus. Furthermore, the computational power of the time did not allow for employment of online computer vision algorithms. Cowen, Briest, and Dombrowski [40] investigated optical guidance inspired by the Sidewinder air-to-air missile system, which uses photo-diodes rather than computer vision.

Technological innovation during the last decades have changed the tasks of AUV from pure surveyers of the large open ocean to active participants in IMR operations. The redesigned tasks also caused redesign in the hulls and thrusters of the vehicles. Typically, the torpedo-shaped AUV design does not allow actuation in all degrees of freedom. The underactuation complicates the control design, and the possible tasks the vehicle can achieve. Thus, modern I-AUVs designs replicate the classical design of the fully-actuated ROV.

Article	Vehicle	Control	Navigation	Result	Docking	Docking Style
[97]	torpedo	fuzzy	acoustic	simulation	stationary	funnel
[184]	torpedo	fuzzy	acoustic	simulation	moving	funnel
[82]	torpedo	pursuit	acoustic	simulation	stationary	-
[234]	torpedo	fuzzy	acoustic	experiment	stationary	funnel
[203]	torpedo	pursuit	acoustic	experiment	stationary	funnel
[40]	torpedo	pursuit	optical	experiment	stationary	funnel
[207]	torpedo	builtin	acoustic	experiment	stationary	funnel
[204]	torpedo	-	acoustic	experiment	stationary	latch
[208]	torpedo	builtin	acoustic	experiment	stationary	funnel
[58]	torpedo	builtin	magnetic	experiment	stationary	funnel
[54]	torpedo	builtin	acoustic	experiment	stationary	platform
[150]	torpedo	iterative	-	simulation	stationary	funnel
[114]	torpedo	builtin	-	experiment	stationary	latch
[155]	torpedo	LQR	optical	simulation	stationary	funnel
[55]	ROV	builtin	hybrid	experiment	stationary	panel
[118]	torpedo	LQR	optical	-	stationary	funnel
[98]	torpedo	builtin	acoustic	experiment	stationary	platform
[84]	torpedo	builtin	acoustic	experiment	stationary	net
[4]	torpedo	builtin	acoustic	experiment	stationary	funnel
[130]	torpedo	builtin	optical	experiment	moving	ASV
[29]	ROV	builtin	hybrid	experiment	stationary	latch
[166]	torpedo	builtin	optical	experiment	stationary	funnel
[86]	torpedo	HOSMC	-	simulation	stationary	funnel

[132]	torpedo	PI	acoustic	experiment	stationary	funnel
[110]	ROV	builtin	hybrid	experiment	stationary	panel
[104]	torpedo	builtin	inertial	experiment	stationary	cradle
[126]	torpedo	builtin	optical	experiment	stationary	latch
[205]	ROV	builtin	optical	simulation	stationary	panel
[167]	torpedo	PD	optical	experiment	stationary	funnel
[236]	torpedo	SMC	hydrid	simulation	stationary	-
[156]	ROV	switching	optical	simulation	stationary	-
[107]	torpedo	builtin	hybrid	experiment	stationary	funnel
[218]	torpedo	fuzzy	acoustic	experiment	stationary	funnel
[237]	ROV	builtin	visual	experiment	stationary	latch
[179]	torpedo	builtin	acoustic	simulation	moving	funnel
[158]	torpedo	switching	visual	simulation	stationary	funnel
[127]	ROV	builtin	hybrid	experiment	stationary	latch
[128]	ROV	iterative	visual	simulation	stationary	funnel
[210]	exotic	fuzzy	optical	experiment	moving	latch
[157]	ROV	hybrid	visual	simulation	stationary	funnel
[89]	torpedo	Adaptive backstep- ping	acoustic	simulation	stationary	funnel
[135]	exotic	fuzzy	magnetic	experiment	moving	funnel
[17]	torpedo	backstepping	-	simulation	stationary	funnel
[193]	torpedo	-	acoustic	simulation	stationary	funnel
[56]	torpedo	PID	acoustic	simulation	stationary	funnel
[239]	ROV	PI/PD	optical	simulation	stationary	funnel
[122]	torpedo	NTSMC	acoustic	simulation	stationary	funnel
[216]	torpedo	P/PID	optical	experiment	stationary	funnel
[124]	ROV	P	optical	experiment	stationary	platform
[120]	torpedo	P/PID	optical	experiment	stationary	funnel
[141]	ROV	P	optical	experiment	stationary	platform
[83]	torpedo	builtin	hybrid	experiment	stationary	cradle
[113]	exotic	builtin	magnetic	experiment	stationary	platform
[198]	ROV	builtin	hybrid	experiment	stationary	platform
[41]	torpedo	Lyapunov	hybrid	experiment	stationary	cradle-platform
[103]	torpedo	PD	optical	experiment	stationary	latch

Table 1.1: Overview of publications related to docking of underwater systems.

Tab. 1.1 provides a summary overview of the publications related to underwater docking. The table divides the shape of the vehicle under investigation into three categories: Torpedo, ROV, and exotic. The torpedo-shaped vehicles often exhibit underactuated behavior, that is they are not capable of actuating all their degrees of freedom, but low hydrodynamic damping. The ROV type vehicle are designed with full actuation, but without regards to the hydrodynamic damping. Exotic type vehicles are consist of biomimetic vehicles and is not covered in this thesis. Evidently, most of the literature considers stationary target docking, where the docking station is located at a known point. Rae and Smith [184] presents one of the earliest works, where the docking station moves. The article considers the problem of recovering a torpedo-shaped AUV using a submarine with a funnel type docking station. Due to the relative size between the submarine and AUV, the paper only considers control of the AUV.

Martins et al. [130] considered recovery of an AUV using an ASV. In contrast to [184], the article considers the ASV as the active member in the system instead of the AUV. The ASV employs computer vision to track the position and attitude of the AUV, such that, the alignment of the ASV allows for docking.

Similarly to [184], Pyle et al. [179] investigated the usage of a large AUV to transport and deploy smaller survey AUVs. The proposed principle bears similarity to the solution from [184], as the small AUV conducted the docking on a funnel type docking station extruded from the larger AUV.

The articles [184, 130, 179] propose a unilateral control strategy, in the sense,

that there is no information sharing between the docking vehicle and the docking station and the control design only considers input of the docking vehicle.

Project AMOUR, described in the articles [229, 230, 49, 50, 228], considered docking in the context of data-muling. The articles employs an AUV named *Starbug* to navigate and dock with an actuated sensor node called *AMOUR*. The docking algorithm utilizes optical navigation based on photo-diodes on the docking rod and hull of the *AMOUR* to home the vehicles into the right positions. The vehicles communicate during the docking procedure, but they share no state information in the process. Effectively, the proposed control strategy belongs to the group of decentralized control algorithms. AMOUR is the first project to enable physical reconfiguration between underwater vehicles.

As part of the ANGELS project, the authors Mintchev et al. [134, 135] considered bio-inspired docking between small-size anguilliform AUVs. The bio-inspired docking approach utilizes electromagnets and electric sensing to navigate and attract each other. The control is a three-phase strategy where phase one aligns and approach the other modules through electrical sensing and thruster control. The second phase employs passive alignment where the electromagnets guides the vehicles together without using thrusters. Finally, the mechanical connection completes the docking by locking the modules together.

Also part of the ANGELS project, the authors Sutantyo et al. [210] considered a bio-inspired docking approach based on optical diodes. The strategy is identical to that of [134] except for replacing the electrical sensing of the first phase with optical photo-diodes. None of the methods in the ANGELS project utilized state-information between the modules during docking.

1.2.3   Outline and Contributions

The following section provides an overview of the outline, as well as, the contributions of each chapter in the thesis.

Chapter 2

Topic: This chapter serves as a preliminary background into the modeling of marine vehicles. The chapter includes; the employed reference coordinate frames, the basic kinematics of the frames with different attitude representations, and the kinetics of marine vehicles. The presented material is based on literature by others [8, 61, 57, 111].

Chapter 3

Topic: The chapter discusses constrained dynamics as a general field of research. The core challenge in constrained dynamics is introduced, and explained with examples. The requirements to automated modelling is formulated and state of the art is discussed in this area.

Contribution: This chapter proposes to use the Udwadia-Kalaba formulation for constrained dynamics to develop a simulator for the modular underwater

robotics system. The system must be able to handle any relative interconnection between the vehicles. Quaternions are chosen as attitude representations for each vehicle to avoid the attitude singularities from the Euler angles. The rigid constraint imposed between connected whiles is derived in quasi-coordinates. The constraint derivation in quasi-coordinates is higher than the generalized coordinate equivalent. However, the quasi-coordinate formulation ensures that the mass matrix stays invertible. The chapter is based on the publications [144], and [146].

Chapter 4

Topic: The chapter seeks to conduct a preliminary experimental validation of the simulator proposed in Chapter 3.

Contribution: The chapter proposes two conceptually simple experiments to evaluate the applicability of the simulator developed in Chapter 3. The first experiment belong to the class of free-decay tests. The interconnected system utilizes the hydrostatic restoring forces from each subsystem in combination with the relative configuration between the subsystems as actuation. The CoB of each subsystem determines the equilibrium of the aggregated system. Manipulation of the relative positions between the CoBs produces damped oscillations until the system comes to rest. The period and magnitude of the oscillations are determined by the inertia and damping of the system. The chapter is based on the publication Nielsen et al. [147].

Chapter 5

Topic: The chapter seeks to identify the dynamic parameters of the BlueROV, as well as, the dynamics of the thrusters.

Contribution: The chapter utilizes towing tank tests to identify the dynamic parameters of the BlueROV vehicle. The identification procedure comprise of two experiments. The first experiment employs drag test of the BlueROV vehicle hull to produce force versus velocity data. Data analysis subsequently identifies the drag coefficients for the *surge*, *sway*, *heave*, and *pitch* DOFs. The second experiments employs drag tests to quantify the level of thrust loss that occurs during motion. measure of thrust loss measured by towing the BlueROV at given velocities Similar to the first experiments, the second experiments tows the BlueROV through the tank, but with thrusters engaged. The comparison between the force data from the first experiment, and the second experiment reveals the thrust loss as a function of velocity. Results of the chapter extends the simulator from Chapter 3 to include better thrust model. The chapter is based on the publication Nielsen et al. [146].

Chapter 6

Topic: The chapter seeks to validate the modular underwater robotic simulator of Chapter 3 using ROV type vehicles.

Contribution: The chapter uses free-motion data from an aggregated system composed of two BlueROV vehicles to evaluate the applicability of the designed simulator. The validation procedure employs two different experiments. The first experiment impress equal thrust surge directed thrusters to produce a straight line trajectory of the aggregated system. The validation relies of comparisons between measured trajectory data and simulated trajectory data. The second experiment impress thrust on only one of the ROV, such that, the second ROV act as dead-weight. The trajectory profile becomes a circular motion and thereby excite both the translational and rotational part of the system. The chapter is based on the publication Nielsen et al. [146].

Chapter 7

Topic: The chapter introduces required preliminaries for Docking Control. The chapter presents the problem and literature of camera-based rendezvous and docking. Furthermore, the chapter presents a basic overview of MPC, as well as, methods for distributing MPCs using dual decomposition.

Chapter 8

Topic: The chapter investigates the rendezvous and docking control for modular underwater robots

Contribution: This chapter investigates the problem of rendezvous and docking with visual constraints in the context of underwater robots with camera-based navigation. The objective is the convergence of the vehicles to a common point while maintaining visual contact. The proposed solution includes the design of a distributed model predictive controller based on dual decomposition, which allows for optimization in a decentralized fashion. The proposed distributed controller enables rendezvous and docking between vehicles while maintaining visual contact. The chapter is based on the publication Nielsen, Johansen, and Blanke [145]

1.3 Publications

The results presented in this thesis is based on the following publications:

[C1] [144] Mikkel Cornelius Nielsen, Mogens Blanke, and Ingrid Schjølberg. "Efficient Modelling Methodology for Reconfigurable Underwater Robots". In: *10th IFAC Conference on Control Applications in Marine Systems CAMS 2016*. Vol. 49. 23. Elsevier B.V., 2016, pp. 74–80

[C2] [147] Mikkel Cornelius Nielsen et al. "Experimental Validation of Dynamic Multi-Body Modelling for Reconfigurable Underwater Robots". In: *Oceans 2016 MTS/IEEE*. 2016, p. 6

[C3] [145] Mikkel Cornelius Nielsen, Tor Arne Johansen, and Mogens Blanke. "Cooperative Rendezvous and Docking for Underwater Robots using Model Pre-

dictive Control and Dual Decomposition". In: *2018 European Control Conference (ECC)*. Limassol, Cyprus: IEEE, 2018, p. 6

[J1] [146] Mikkel Cornelius Nielsen et al. "Constrained multi-body dynamics for modular underwater robots — Theory and experiments". In: *Ocean Engineering* 149.February 2018 (2018), pp. 358–372

Other published work that is not included in this thesis is:

- [77] Nicholas Hansen et al. "Short-range sensor for underwater robot navigation using line-lasers and vision". In: *10th IFAC Conference on Manoeuvring and Control of Marine Craft MCMC 2015*. Vol. 28. 16. Elsevier B.V., 2015, pp. 113–120

- [63] Lidia Furno, Mikkel Cornelius Nielsen, and Mogens Blanke. "Centralised versus decentralised control reconfiguration for collaborating underwater robots". In: *9th IFAC Symposium on Fault Detection, Supervision and Safety for Technical Processes SAFEPROCESS 2015*. Vol. 48. 21. Elsevier Ltd., 2015, pp. 732–739

- [38] David Johan Christensen et al. "Collective Modular Underwater Robotic System for Long-Term Autonomous Operation". In: *IEEE International Conference on Robotics and Automation (ICRA)*. Seattle, Washington: IEEE, 2015

Part I

Modeling

Chapter 2

Modeling of Marine Vehicles

The study of motion of an object consists of both the kinematics - the *geometry of motion* - and the kinetics - the *cause of the motion*. The combination of kinematics and kinetics describe the *dynamics* of the object.

This chapter introduces the basic reference frames and the related kinematics, as well as, the kinetics.

Organization of this Chapter

This chapter is organized as follows. Section 2.1 introduces the frames of references employed in the modeling and control of marine vehicles.

The coordinate transformations between different frames, along with the correpsonding mappings betweetn the quantities in these frames are described in Section 2.2 after the relevant notation is introduced. Section 2.3 completes the chapter by introducing the kinetics of marine vehicles. The material presented in this chapter is based on [61, 57, 111].

This thesis investigates the study of dynamics of rigid-bodies and therefore its appropriate to begin with the definiton of a rigid-body.

Definition 2.1. *Rigid-Body*
  A rigid-body is a collection of particles comprising a solid body. The distance between any two particles in the solid body is invariant with respect to time.

2.1 Reference Frames

Describing motion of rigid bodies requires measurable quantities, such as positions, angles, as well as, velocities and accelerations of these. Such quantities can be measured in relation to different references, two of which will be used in the analysis presented in this thesis. These frames are defined in the following:

> **Definition 2.2.** *Earth-Centered-Inertial (ECI) Frame*
> *The ECI Frame is an inertial frame with an origin $\mathcal{O}_i = [x^i, y^i, z^i]$ centered at the center of mass (CoM) of Earth. The z^i-xis point towards the geographical North Pole, the x^i-axis is directed towards the vernal equinox and the y^i-axis completes the right-handed orthogonality. The x^i and y^i lies in the equatorial plane. The ECI frame does not rotate with the Earth.*

The direct result of using the ECI frame is that objects at rest on the surface of the Earth are moving in the ECI frame. Newton's laws of motion in their the simplest form are defined in an inertial reference frame. A more intuitive way to consider motion on Earth is by fixing the reference frame to Earth.

> **Definition 2.3.** *Earth-Centered-Earth-Fixed (ECEF) Frame*
> *The ECEF frame is a is a rotating frame of reference with origin $\mathcal{O}_e = [x^e, y^e, z^e]$ centered at the CoM of Earth. The x^e-axis is directed to the intersection between the prime meridian of the Earth and the equator, the z^e-axis points to geographical North and the y^e-axis completes the right-handed orthogonality. The rotation rate with respect to the ECI frame is $\omega_{ie} = 7.2921 \cdot 10^{-5}$ rad/s around the z^e-axis.*

Since the ECEF frame follows the earth rotation, it is no longer an inertial frame. In relation to Newton's laws of motion, the rotation of the Earth can be compensated in the equations at the price of higher complexity in the descriptions.

When navigation in a local area on Earth is considered a local geodetic reference frame is usually employed.

> **Definition 2.4.** *North-East-Down (NED) Frame*
> *The NED frame is a local geodetic reference frame. The origin of the reference frame $\mathcal{O}_n = [x^n, y^n, z^n]$ is fixed at a point on the surface of the earth. The curvature of the Earth is approximated to be zero such that a small area around the origin is assumed flat, thus forming a tangent plane. The x^n-axis points towards the North Pole, the z^n-axis points towards the center of the Earth and the y^n-axis completes the right-handed orthogonality.*

The NED frame is often referred to as the *Navigation frame*.

Def. 2.1 states that the rigid-body is a collection of particles that form a solid body. To effectively refer to each point on the body, another reference frame is needed.

> **Definition 2.5.** *Body-Fixed Frame*
> *The body-fixed frame is a moving reference frame. The origin $\mathcal{O}_b = [x^b, y^b, z^b]$ is fixed at a point on the body. Often, but not always, the point chosen is the CoM. The x^b-axis points from aft to fore, the z^b-axis points from origin towards bottom, and the y^n-axis completes the right-handed orthogonality. Fig. 2.2 depicts the three principle axes of the body-fixed frame.*

The four different reference frames are depicted on Fig. 2.1. The z-axis of the ECI and ECEF frames coincide with each other, while the   Fig. 2.1 shows the frames
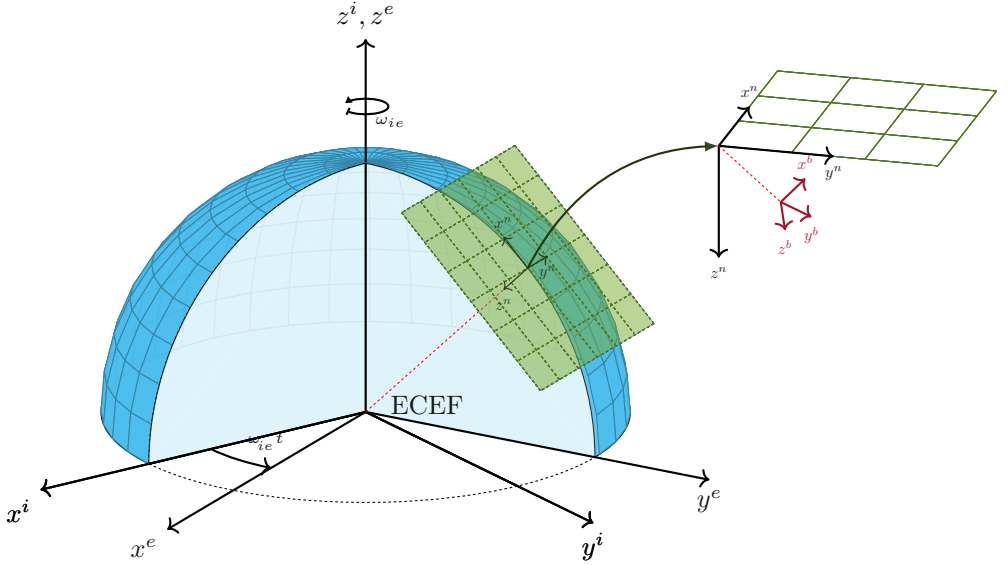
Figure 2.1: The z-axis of the ECI and ECEF frame coincide with each other at all time. The ECEF frame rotates around the z^e-axis with rotation rate ω_{ie}. The NED frame x_n, y_n, z_n is a tangent plane on the Earth, and the body-fixed frame $\{b\}$ is measured relative to the NED frame. inspired by [61, Fig. 2.2].

of reference in relation to the Earth.

2.2 Kinematics

A marine craft moving in the NED frame has 6 DOF, three position coordinates and three rotations around the different axes, together they form the pose of the vehicle. The name of each DOF is defined for marine crafts by Society of Naval Architects and Marine Engineers (SNAME) and can be found in Table 2.1.

Degree of Freedom	Forces/Moments	Linear/Angular Velocities	Positions/Angles
Translation along x-axis (*surge*)	X	u	x
Translation along y-axis (*sway*)	Y	v	y
Translation along z-axis (*heave*)	Z	w	z
Rotation about x-axis (*roll*)	L	p	ϕ
Rotation about y-axis (*pitch*)	M	q	θ
Rotation about z-axis (*yaw*)	N	r	ψ

Table 2.1: SNAME notation for marine vessels

A position of a body-fixed frame $\{b\}$ with respect to the NED frame $\{n\}$ mea-

19
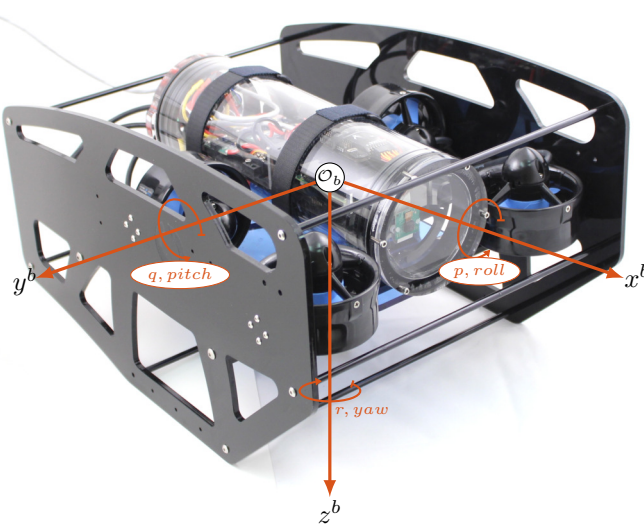
Figure 2.2: The principle axes x^b, y^b, z^b extending out from the origin $\mathcal{O}_b$ of the body-fixed frame. The rotation follow the right-hand convention around each axis.

sured in the NED frame is denoted $\boldsymbol{p}^n_{b/n}$ and defined as

$$\boldsymbol{p}^n_{b/n} = \begin{bmatrix} x^n, & y^n, & z^n \end{bmatrix}^T \in \mathbb{R}^3$$

The attitude of a body-fixed frame $\{b\}$ with respect to the NED frame can be described in different formalisms. Two formalisms are used in this work, namely Euler angle and attitude quaternions.

The Euler Angles describing the rotation from the body-fixed frame $\{b\}$ to the NED frame $\{n\}$ are denoted $\boldsymbol{\Theta}^n_b$

$$\boldsymbol{\Theta}^n_b = \begin{bmatrix} \phi, & \theta, & \psi \end{bmatrix}^T \in \mathbb{R}^3 \tag{2.1}$$

The pose of the body-fixed $\{b\}$ measured in the NED frame is denoted $\boldsymbol{\eta}$ such that

$$\boldsymbol{\eta} = \begin{bmatrix} \boldsymbol{p}^n_{b/n} \\ \boldsymbol{\Theta}^n_b \end{bmatrix} \in \mathbb{R}^6 \tag{2.2}$$

Alternatively if the Quaternions are employed the pose vector becomes $\boldsymbol{\eta} \in \mathbb{R}^7$. The body-fixed linear velocities with respect to the NED frame $\{n\}$ measured in

the body-fixed frame $\{b\}$ is denoted $\boldsymbol{v}_{b/n}^b$ and defined as

$$\boldsymbol{v}_{b/n}^b = \begin{bmatrix} u, & v, & w \end{bmatrix}^T \in \mathbb{R}^3$$

The body-fixed rotational velocities in the body-fixed frame $\{b\}$ relative to NED frame $\{n\}$ are denoted $\boldsymbol{\omega}_{b/n}^b$ and defined as

$$\boldsymbol{\omega}_{b/n}^b = \begin{bmatrix} p, & q, & r \end{bmatrix}^T \in \mathbb{R}^3$$

The linear and rotational body-fixed velocities are combined into the body-fixed velocity vector $\boldsymbol{\nu}$ such that

$$\boldsymbol{\nu} = \begin{bmatrix} \boldsymbol{v}_{b/n}^b \\ \boldsymbol{\omega}_{b/n}^b \end{bmatrix} \in \mathbb{R}^6 \tag{2.3}$$

The body-fixed forces and moments are denoted $\boldsymbol{f}_b^b$ and $\boldsymbol{m}_b^b$ respectively and defined as

$$\boldsymbol{f}_b^b = \begin{bmatrix} X, & Y, & Z \end{bmatrix}^T \in \mathbb{R}^3, \quad \boldsymbol{m}_b^b = \begin{bmatrix} K, & M, & N \end{bmatrix}^T \in \mathbb{R}^3$$

2.2.1 Frame Transformations

In order to properly use the different reference frames a relationship between the NED and body-fixed frames must be established. A vector in one frame of reference can be translated to another frame by a rotation matrix $\boldsymbol{R}$. A matrix $\boldsymbol{R} \in \mathbb{R}^{n \times n}$ is a rotation matrix if and only if it belongs to the *Special Orthogonal Group* $\mathbb{SO}(n)$. In the case of a vehicle moving in three dimensional space, the matrix $\boldsymbol{R} \in \mathbb{R}^{3 \times 3}$ and belong to the $\mathbb{SO}(3)$. The $\mathbb{SO}(3)$ group is defined as every matrix belonging to $\mathbb{R}^{3 \times 3}$ such that its transpose is equal to its inverse and the determinant is postive one:

$$\mathbb{SO}(3) = \{\boldsymbol{R} \in \mathbb{R}^{3 \times 3} | \boldsymbol{R}^T \boldsymbol{R} = \boldsymbol{I} \wedge \det(\boldsymbol{R}) = 1\} \tag{2.4}$$

The rotation matrix $\boldsymbol{R}$ is parameterized by the attitude of the rigid-body with respect to the appropriate frame of reference, in this case the NED frame. Thereby, the linear body-fixed velocities $\boldsymbol{v}_{b/n}^b$ can be transformed into the NED frame by

$$\boldsymbol{v}_{b/n}^n = \boldsymbol{R}_b^n \boldsymbol{v}_{b/n}^b$$

By assumption the NED frame is inertial and time evolution of the origin of the body-fixed frame in the NED frame $\dot{\boldsymbol{p}}_{b/n}^n$ is equal to the linear velocity vector $\boldsymbol{v}_{b/n}^n$ such that

$$\dot{\boldsymbol{p}}_{b/n}^n = \boldsymbol{R}_b^n \boldsymbol{v}_{b/n}^b \tag{2.5}$$

Transforming the rotational velocity of the body-fixed frame $\boldsymbol{\omega}_{b/n}^b$ to attitude rates $\dot{\boldsymbol{\Theta}}_b^n$ is conducted through the transformation matrix $\boldsymbol{T}$

$$\dot{\boldsymbol{\Theta}}_b^n = \boldsymbol{T} \boldsymbol{\omega}_{b/n}^b \tag{2.6}$$

There exist multiple different ways to parameterize a rotation matrix $\boldsymbol{R}_b^n\left(\cdot\right)$ and transformation matrix $\boldsymbol{T}\left(\cdot\right)$ and each method has advantages and disadvantages. Two different parameterizations will be used in this work, namely Euler Angles and Quaternions. The rotation matrix constructed from Euler Angles $\boldsymbol{R}_b^n\left(\boldsymbol{\Theta}_b^n\right)$ is the result of a sequence of rotations around each principle axis.

$$\boldsymbol{R}_{x,\phi} = \begin{bmatrix} 1 & 0 & 0 \\ 0 & \cos\left(\phi\right) & -\sin\left(\phi\right) \\ 0 & \sin\left(\phi\right) & \cos\left(\phi\right) \end{bmatrix}, \quad \boldsymbol{R}_{y,\theta} = \begin{bmatrix} \cos\left(\theta\right) & 0 & \sin\left(\theta\right) \\ 0 & 1 & 0 \\ -\sin\left(\theta\right) & 0 & \cos\left(\theta\right) \end{bmatrix} \tag{2.7}$$

$$\boldsymbol{R}_{z,\psi} = \begin{bmatrix} \cos\left(\psi\right) & -\sin\left(\psi\right) & 0 \\ \sin\left(\psi\right) & \cos\left(\psi\right) & 0 \\ 0 & 0 & 1 \end{bmatrix}$$

The *extrinsic* rotation sequence $z-y-x$ defines the rotation from body-fixed frame $\{b\}$ to NED frame $\{n\}$

$$\boldsymbol{R}_b^n\left(\boldsymbol{\Theta}_b^n\right) = \begin{bmatrix} \cos(\theta)\cos(\psi) & -\cos(\phi)\sin(\psi) + \sin(\phi)\sin(\theta)\cos(\psi) & \sin(\phi)\sin(\psi) + \cos(\phi)\cos(\psi)\sin(\theta) \\ \cos(\theta)\sin(\psi) & \cos(\phi)\cos(\psi) + \sin(\phi)\sin(\theta)\sin(\psi) & -\sin(\phi)\cos(\psi) + \cos(\phi)\sin(\theta)\sin(\psi) \\ -\sin(\theta) & \sin(\phi)\cos(\theta) & \cos(\phi)\cos(\theta) \end{bmatrix}$$

The transformation of body-fixed angular velocities $\boldsymbol{\omega}_{n/b}^b$ to attitudes rates $\dot{\boldsymbol{\Theta}}_b^n = [\dot\phi, \dot\theta, \dot\psi]$ is related by the transformation matrix $\boldsymbol{T}_\Theta$

$$\boldsymbol{T}_\Theta\left(\boldsymbol{\Theta}_b^n\right) = \begin{bmatrix} 1 & \sin\left(\phi\right)\tan\left(\theta\right) & \cos\left(\phi\right)\tan\left(\theta\right) \\ 0 & \cos\left(\phi\right) & -\sin\left(\phi\right) \\ 0 & \sin\left(\phi\right)/\cos\left(\theta\right) & \cos\left(\phi\right)/\cos\left(\theta\right) \end{bmatrix} \tag{2.8}$$

The three Euler Angles are a *minimal representation* needed to describe all possible rotations. However, the division with $\cos\left(\theta\right)$ in Eq. (2.8) yields a singularity at $\theta \pm 90°$. A solution to the singularity problem in Eq. (2.8) is to represent the attitude by another parametrization such as the attitude quaternions. The attitude quaternion $\boldsymbol{q}$ consists of four componens:

$$\boldsymbol{q}_b^n = \begin{bmatrix} \eta, & \varepsilon_1, & \varepsilon_2, & \varepsilon_3 \end{bmatrix}^T. \tag{2.9}$$

The sub-vector $\boldsymbol{\varepsilon} = [\varepsilon_1, \varepsilon_2, \varepsilon_3]^T$ is known as the Euler axis vector. Since any rotation in three dimensions belong to the Special Orthogonal group $\mathbb{SO}\left(3\right)$, the quaternion must be constrained. The rotation matrix parameterized by the attitude quaternions can now be constructed as

$$\boldsymbol{R}_b^n\left(\boldsymbol{q}\right) = \boldsymbol{I}_3 + 2\eta\boldsymbol{S}\left(\boldsymbol{\varepsilon}\right) + 2\boldsymbol{S}^2\left(\boldsymbol{\varepsilon}\right), \tag{2.10}$$

where the skew-symmetric matrix $\boldsymbol{S}\left(\boldsymbol{\varepsilon}\right)$ is defined as follows,

$$\boldsymbol{\lambda} \times \boldsymbol{a} = \boldsymbol{S}\left(\boldsymbol{\lambda}\right)\boldsymbol{a} = \begin{bmatrix} 0 & -\lambda_3 & \lambda_2 \\ \lambda_3 & 0 & -\lambda_1 \\ -\lambda_2 & \lambda_1 & 0 \end{bmatrix} \begin{bmatrix} a_1 \\ a_2 \\ a_3 \end{bmatrix}, \tag{2.11}$$

such that $\boldsymbol{S}\left(\boldsymbol{\varepsilon}\right)^T = -\boldsymbol{S}\left(\boldsymbol{\varepsilon}\right)$. The resulting rotation matrix $\boldsymbol{R}_b^n\left(\boldsymbol{q}\right)$ can be written on component form as follows

$$\boldsymbol{R}_b^n = \begin{bmatrix} 1 - 2\left(\varepsilon_2^2 + \varepsilon_3^2\right) & 2\left(\varepsilon_1\varepsilon_2 - \varepsilon_3\eta\right) & 2\left(\varepsilon_1\varepsilon_3 + \varepsilon_2\eta\right) \\ 2\left(\varepsilon_1\varepsilon_2 + \varepsilon_3\eta\right) & 1 - 2\left(\varepsilon_1^2 + \varepsilon_3^2\right) & 2\left(\varepsilon_2\varepsilon_3 - \varepsilon_1\eta\right) \\ 2\left(\varepsilon_1\varepsilon_3 - \varepsilon_2\eta\right) & 2\left(\varepsilon_2\varepsilon_3 + \varepsilon_1\eta\right) & 1 - 2\left(\varepsilon_1^2 + \varepsilon_2^2\right) \end{bmatrix} \tag{2.12}$$

The attitude quaternion rate $\dot{\boldsymbol{q}}$ is related to the body-fixed rotational velocity $\boldsymbol{\omega}_{b/n}^b$ as

$$\dot{\boldsymbol{q}} = \boldsymbol{T}_q\boldsymbol{\omega}_{b/n}^b \tag{2.13}$$

where the $\boldsymbol{T}_q\left(q\right)$ matrix is defined as

$$\boldsymbol{T}_q = \frac{1}{2}\boldsymbol{H}^T = \frac{1}{2}\begin{bmatrix} -\varepsilon_1 & -\varepsilon_2 & -\varepsilon_3 \\ \eta & -\varepsilon_3 & \varepsilon_2 \\ \varepsilon_3 & \eta & -\varepsilon_1 \\ -\varepsilon_2 & \varepsilon_1 & \eta \end{bmatrix} \in \mathbb{R}^{4\times3} \tag{2.14}$$

such that the $\boldsymbol{H}$ matrix is

$$\boldsymbol{H} = [-\boldsymbol{\varepsilon},\ \eta\boldsymbol{I}_3 - \boldsymbol{S}\left(\boldsymbol{\varepsilon}\right)] \in \mathbb{R}^{3\times4} \tag{2.15}$$

where $\boldsymbol{a}$ is an arbitrary vector in $\mathbb{R}^3$. For convenience the transformations of the linear and angular velocities onto the time evolution of the position and attitude can be represented by a combined pose transformation matrix $\boldsymbol{J}_q$ as follows

$$\dot{\boldsymbol{\eta}} = \boldsymbol{J}_q\boldsymbol{\nu} \tag{2.16}$$

where $\boldsymbol{J}_q$ is the block diagonal matrix composed of the rotation matrix $\boldsymbol{R}_b^n\left(\boldsymbol{q}\right)$ and the angular transformation matrix $\boldsymbol{T}_q\left(\boldsymbol{q}\right)$ such that

$$\boldsymbol{J}_q = \begin{bmatrix} \boldsymbol{R}_b^n & \boldsymbol{0}_{3\times3} \\ \boldsymbol{0}_{4\times3} & \boldsymbol{T}_q \end{bmatrix} \tag{2.17}$$

The unit condition for the attitude quaternion imposes the constraint on the following form [111],

$$\boldsymbol{q}^T\boldsymbol{q} = 1 \tag{2.18}$$

Numerical errors in integration procedures cause drift of the constraints. The numerical errors violates the constraint, such that $\boldsymbol{q}^T\boldsymbol{q} \neq 1$. Constraint drift is a recognised problem in the literature. The authors, Braun and Goldfarb [27] investigated methods for constraint drift removal in the Udwadia-Kalaba equations. The unity constraint on the quaternions can be imposed continuously from the following equation given in [61].

$$\dot{\boldsymbol{u}} = \boldsymbol{T}_u\left(\boldsymbol{u}\right)\boldsymbol{\omega}_{b/n}^b + \frac{\gamma}{2}\left(1 - \boldsymbol{u}^T\boldsymbol{u}\right)\boldsymbol{u} \text{ for } \gamma \geq 0 \tag{2.19}$$

2.3 Kinetics

The previous section considered the kinematics of the motion. This section will continue with the cause of the motion, the kinetics. Using Fossen's robot-like vectorial description the kinetics of the marine vehicle can be represented on the following form

$$\boldsymbol{M}\dot{\boldsymbol{\nu}} + \boldsymbol{D}(\boldsymbol{\nu})\boldsymbol{\nu} + \boldsymbol{C}(\boldsymbol{\nu})\boldsymbol{\nu} + \boldsymbol{g}(\boldsymbol{\eta}) = \boldsymbol{\tau} \tag{2.20}$$

where $\boldsymbol{M}$ is the system inertia, $\boldsymbol{D}(\boldsymbol{\nu})$ is the damping coefficient matrix, $\boldsymbol{C}(\boldsymbol{\nu})$ is the Coriolis-centripetal matrix[61, p. 53], $\boldsymbol{g}(\boldsymbol{\eta})$ is the hydrostatic vector and $\boldsymbol{\tau}$ is the applied thruster forces and moments. The inertia matrix $\boldsymbol{M}$ is composed of both the rigid-body inertia $\boldsymbol{M}_{RB}$ and the added mass $\boldsymbol{M}_A$ due to water.

$$\boldsymbol{M} = \boldsymbol{M}_{RB} + \boldsymbol{M}_A \tag{2.21}$$

The damping affecting the underwater vehicle is composed of the skin friction and Vortex Shedding. Furthermore, the frequency dependency of the skin friction damping can be neglected due to lack of waves. These two damping contributions are estimated together as a quadratic function in the body-velocity $\boldsymbol{\nu}$ such that

$$\boldsymbol{D} = \boldsymbol{D}_L\boldsymbol{\nu} + \boldsymbol{D}_{NL}(\boldsymbol{\nu})\boldsymbol{\nu} \tag{2.22}$$

It is common for underwater vehicles to only consider the diagonal elements of the damping matrices $\boldsymbol{D}_L$ and $\boldsymbol{D}_{NL}$ such that

$$
\begin{aligned}
\boldsymbol{D}_L &= \mathrm{diag}\left(X_u, Y_v, Z_w, K_p, M_q, N_r\right), \\
\boldsymbol{D}_{NL} &= \mathrm{diag}\left(X_{|u|u}, Y_{|v|v}, Z_{|w|w}, N_{|p|p}, M_{|q|q}, N_{|r|r}\right)
\end{aligned} \tag{2.23}
$$

The inertia matrix $\boldsymbol{M}$ can be decomposed into four sub-matrices such that

$$\boldsymbol{M} = \begin{bmatrix} \boldsymbol{M}_{11} & \boldsymbol{M}_{12} \\ \boldsymbol{M}_{21} & \boldsymbol{M}_{22} \end{bmatrix} \tag{2.24}$$

The coriolis-centripetal force matrix is constructed from the sub-matrices of the $\boldsymbol{M}$ such that

$$\boldsymbol{C}(\boldsymbol{\nu}) = \begin{bmatrix} \boldsymbol{0}_{3\times3} & -\boldsymbol{S}\left(\boldsymbol{M}_{11}\boldsymbol{v}^b_{b/n} + \boldsymbol{M}_{12}\boldsymbol{\omega}^b_{b/n}\right) \\ -\boldsymbol{S}\left(\boldsymbol{M}_{11}\boldsymbol{v}^b_{b/n} + \boldsymbol{M}_{12}\boldsymbol{\omega}^b_{b/n}\right) & -\boldsymbol{S}\left(\boldsymbol{M}_{21}\boldsymbol{v}^b_{b/n} + \boldsymbol{M}_{22}\boldsymbol{\omega}^b_{b/n}\right) \end{bmatrix} \tag{2.25}$$

The hydrostatic vector $\boldsymbol{g}(\boldsymbol{\eta})$ is constructed based on the difference between the CoB and CoM.

$$\boldsymbol{g}(\boldsymbol{\eta}) = -\begin{bmatrix} \boldsymbol{R}^b_n\left(\boldsymbol{f}^n_g + \boldsymbol{f}^n_b\right) \\ \boldsymbol{r}^b_g \times \boldsymbol{R}^b_n\boldsymbol{f}^n_g + \boldsymbol{r}^b_b \times \boldsymbol{R}^b_n\boldsymbol{f}^n_b \end{bmatrix} \tag{2.26}$$

The vector between the CoM and the origin of the body-fixed frame is denoted $\boldsymbol{r}^b_g$. The gravity force acting on the CoM is denoted $\boldsymbol{f}^n_g$. The vector between the CoB and the origin of the body-fixed frame is denoted $\boldsymbol{r}^b_b$. The restoring force acting on

the CoB is denoted $\boldsymbol{f}_b^n$. In this thesis, the origin of the body-fixed frame is always assumed to intersect with the CoM. The assumption is not restrictive, since the formulations can without loss of generality be transformed to any other point on the vehicle. Consequently $\boldsymbol{r}_g^b \equiv 0$ throughout the thesis.

In the end, a marine vehicle can be described by combining Eq. (2.16) and Eq. (2.20) into the following

$$
\begin{aligned}
\dot{\boldsymbol{\eta}} &= \boldsymbol{J}_{(\cdot)}\boldsymbol{\nu} \\
\boldsymbol{M}\dot{\boldsymbol{\nu}} + \boldsymbol{D}\left(\boldsymbol{\nu}\right)\boldsymbol{\nu} + \boldsymbol{C}\left(\boldsymbol{\nu}\right)\boldsymbol{\nu} + \boldsymbol{g}\left(\boldsymbol{\eta}\right) &= \boldsymbol{\tau},
\end{aligned}
\tag{2.27}
$$

where $_{(\cdot)}$ denotes the parameterization, e.g., Euler angles Θ, or $\boldsymbol{q}$.

2.4 Chapter Summary

The chapter presented an overview of important notions associated with dynamics of marine vehicles and introduced the relevant notation, which is followed throughout the entire thesis. The problem related to attitude representation, singularity descriptions and constraint maintenance was introduced. Chapter 3 continues by introducing the the problems related to the analsis and control of contrained dynamics.

Chapter 3

Constrained Dynamical Systems

There exist many different formulations for the derivation of motion, and each of them has advantages and disadvantages. The specific characteristics of the underlying system dynamics often indicate, which methods are more suitable to employ. Though formulations may differ, the trajectories they produce are identical. The specific equations of motion related to unconstrained marine vehicles were presented in Chapter 2. This chapter introduces modeling methods for constrained multi-body methods and the derivation of a multi-body model for modular underwater robots.

Contribution

The contribution of this chapter is an overview of the field of constrained dynamics and the derivation of the model for the modular underwater robotic systems. Numerical simulations are also provided.

Organization of this chapter

The organization of the chapter is as follows: Section 3.1 defines the notation and concepts used for modeling of constrained dynamic systems. Section 3.2 discusses approaches to eliminate Lagrange's multipliers. Section 3.3 presents the formulation used in the modeling of the modular underwater robotic system. Section 3.4 presents the constraint formulation used for the modular underwater robotic system and the necessary derivations to arrive at the desired constraint form. Section 3.6 presents a numerical study of the developed model. Finally, Section 3.7 summarises the chapter.

Publications

The material used in this chapter is based on the publication

[C1] Mikkel Cornelius Nielsen, Mogens Blanke, and Ingrid Schjølberg. "Efficient Modelling Methodology for Reconfigurable Underwater Robots". In: *10th IFAC Conference on Control Applications in Marine Systems CAMS 2016*. Vol. 49. 23. Elsevier B.V., 2016, pp. 74–80

[J1] Mikkel Cornelius Nielsen et al. "Constrained multi-body dynamics for modular underwater robots — Theory and experiments". In: *Ocean Engineering* 149.February 2018 (2018), pp. 358–372

3.1 Dynamics

Describing the motion of bodies through forces and moments is the foundation of *Classical Mechanics*. Newton's laws of motion describe the motion of unconstrained mechanical systems using differential notation, and are represented in an Ordinary Differential Equation (ODE) form as:

$$\dot{\boldsymbol{x}} = \boldsymbol{f}\left(t, \boldsymbol{x}\right), \qquad (3.1)$$

where $\boldsymbol{x}$ is the state-vector - typically comprised of the pose and velocity - and t is the time. When a mechanical system is subject to constraints, the formulation of the system contains algebraic relations between the states and the problem is then called a Differential Algebraic Equation (DAE) system. Formally a DAE is defined as follows:

> **Definition 3.1.** *Differential Algebraic Equation (DAE)*
>   *An equation system on the form*
>
> $$\boldsymbol{f}\left(t, \dot{\boldsymbol{x}}, \boldsymbol{x}\right) = 0, \qquad (3.2)$$
>
> *is said to be a DAE system if $\frac{\mathrm{d}f}{\mathrm{d}\dot{x}}$ is rank-deficient [28, 133, 70].*

The form in Eq. 3.2 is the implicit form, and it is evident from Eq. 3.1 that any ODE can be re-written on the implicit form.
A vector of parameters can describe the configuration of a rigid-body. These configuration parameters are denoted the *Generalized Coordinates* and defined as follows

> **Definition 3.2.** *Generalized Coordinates*
>   *The generalized coordinates of a system are the parameters that uniquely describe the configuration of a given system.*

In this work, generalized coordinates are denoted $\boldsymbol{\xi}$ for a vector of coordinates and ξ_i for a particular coordinate. Definition. 3.2 does not require the parameters to be independent of each other, but the minimal cardinality of a set of generalized coordinates is equal to the number of DOF of the system, and if this is the case the generalized coordinates are independent of each other.

> **Definition 3.3.** *Degree of Freedom (DOF)*
>   *The DOF of a mechanical system correspond to the number of independent parameters required to define its configuration.*

Degrees of freedom	Possible system
One	Simple piston
Two	Particle on plane
Three	Particle in space or rigid body on a plane
Four	Surface Marine Vehicle with Roll
Five	Two particles at constant distance to each other
Six	Rigid body moving freely in space

Table 3.1: Degrees of freedom/Minimal number of generalized coordinates for different systems.

Table 3.1 lists a couple of example systems based on their DOFs. The consequence of Definition 3.2 and 3.3 is that quaternions are considered a valid, but no minimal, set of generalized coordinates when representing attitude. In other words, the quaternion parameters are *dependent* of each other rather than *independent*.

The dependency between the generalized coordinates imposes additional dynamical behavior described by a relation between coordinates and in case of the quaternions the unit constraint of Eq. (2.18) is precisely that. However, a constraint is not limited to just coordinates as the following definition will expand on:

> **Definition 3.4.** *Mechanical Constraint*
> *A mechanical constraint c is an algebraic relation between coordinates and momenta.*

The rest of the thesis will use the terms "mechanical constraint" and "constraint" interchangeably. Different constraint classifications exist depending on their parameterizations. The most common classifications are *holonomic*, and *non-holonomic* constraints and further subdivisions exist, such as *scleronomic* and *rheonomic* constraints.

> **Definition 3.5.** *Holonomic Constraint*
> *A constraint c is said to be* holonomic *iff it can be represented independently of the generalised velocities $\dot{\boldsymbol{\xi}}$ such as in the following equation*
>
> $$c\left(\boldsymbol{\xi}\right) = 0. \tag{3.3}$$
>
> *If time appears explicitly in the formulation*
>
> $$c\left(\boldsymbol{\xi}, t\right) = 0, \tag{3.4}$$
>
> *the constraint is called scleronomic, otherwise the constraint is rheonomic.*

From Definition 3.5 it is evident that the *non-holonomic* constraint is merely all constraints that do not abide by the definition. The importance of the holonomic classification comes from the way such constraints are handled in the derivation of the equations of motion.

A holonomic constraint limits the configuration space of the system, thereby the number of DOFs are reduced.

A system with n_ξ number of independent generalized coordinates subjected to n_c number of independent holonomic constraints will have $n_\xi - n_c$ number of DOFs. Non-holonomic constraint does not decrease the number of DOFs in the system. Instead, the non-holonomic constraints restrict the evolution of the configuration parameters. The parameterizations of non-holonomic constraint can in principle be anything. However, in this thesis the constraints will be limited to constraints on the velocity form:

$$\mathbf{\Phi}\dot{\boldsymbol{\xi}} - b = 0. \tag{3.5}$$

The velocity form parametrization of Eq. (3.5) commonly occurs in mechanical systems [18]. The non-holonomic constraints are a more general class of constraints compared to holonomic constraints. A holonomic constraint can be transformed into a non-holonomic, sometimes denoted a pseudo non-holonomic constraint, by time differentiation. The non-holonomic constraints are non-integrable and thus cannot be transformed into a holonomic constraint. Non-holonomic constraints occurs in many conventional systems, and consequently, a vast amount of research has investigated ways to incorporate the constraints into the equation of motions.

Newtons laws of motion define the relationship between the forces and the sub-
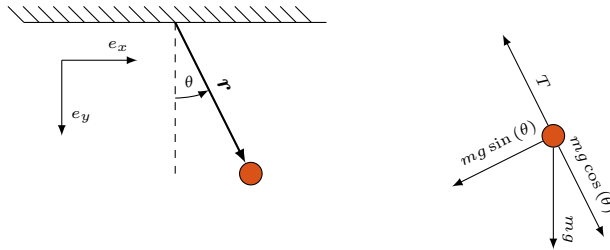
Figure 3.1: The simple pendulum along with a force diagram.

sequent motion for bodies. However, the Newtonian formulation produces some difficulty when the systems under investigation are subjected to constraints. The primary problem with a constrained Newtonian system is the requirement of the first and third law, namely, to identify all forces interacting with the body and the reaction forces induced by the constraint. There is no systematic way to obtain the reaction force of the constraint. That is to say, while Newtons laws of motion are fundamental to any body under the influence of forces, the laws themselves do not yield a procedure to obtain the equations of motion of a given system. The following example clarifies the unwieldiness of the vector-based Newtonian approach for systems subjected to constraints:

Example 3.1: Simple Pendulum using Newton

The Newtonian approach to finding the equations of motion is to consider all the forces acting on the bob. By inspection of Fig. 3.1 yields the following forces

$$m\ddot{\boldsymbol{r}} = -T\frac{\boldsymbol{r}}{|\boldsymbol{r}|} + mg\boldsymbol{e}_y. \tag{3.6}$$

The problem is then to find the rope tension T. The motion of the bob is circular and thus the tension in the rope consists of the centripetal force F_c and the radial component of the gravity $\frac{mg}{l}y$.

$$F_c = m\frac{v^2}{l} \ : \ T = m\frac{\dot{x}^2 + \dot{y}^2}{\sqrt{x^2 + y^2}} + \frac{mg}{\sqrt{x^2 + y^2}}y.$$

Inserting the tension into Eq. (3.6) and decomposing into Cartesian coordinates the equations of motion yields

$$\ddot{x} = -\frac{\left(\dot{x}^2 + \dot{y}^2\right)x + gxy}{x^2 + y^2},$$

$$\ddot{y} = -\frac{\left(\dot{x}^2 + \dot{y}^2\right)y - gx^2}{x^2 + y^2},$$

where $v^2 = \dot{x}^2 + \dot{y}^2$ and $l = ||\boldsymbol{r}||_2$.

The first thing to notice from Example 3.1 is that the problem only has one DOF, but uses two coordinates in the derivations. Thus there exist an implicit constraint between the coordinates, in this case, the constraint is:

$$c\left(\boldsymbol{\xi}\right) = x^2 + y^2 - l^2. \tag{3.7}$$

The tension T is the force maintaining the constraint. Thus the constraint is maintained on force level rather than the position level. Identifying T is challenging because there is no systematic way of deriving it. In a static case, where the bob is at rest at the equilibrium $\theta = 0$, the tension in the rope is merely the gravity force. However, when motion occurs, the centripetal forces due to the circular motion are also applied in the rope.

Lagrangian Mechanics is a reformulation of mechanics focusing on the system energy instead of the forces and moments. The advantage of the energy-based formulation is the ability to systematically derive the equations of motions for both constrained and unconstrained systems.

Given a system with only holonomic constraints and a minimal vector of generalized coordinates $\boldsymbol{\xi}$ it is possible to derive the system *Lagrangian L*.

$$L = T - V, \tag{3.8}$$

where T is the *kinetic energy* and V is the potential energy. Then the equations of motion of the system can be derived by Lagrange's Equations of the second kind,

$$\frac{\mathrm{d}}{\mathrm{d}t}\frac{\mathrm{d}}{\mathrm{d}\dot{\xi}_i}L - \frac{\mathrm{d}}{\mathrm{d}\xi_i}L = 0 \text{ for } i \in \boldsymbol{\xi}. \tag{3.9}$$

The following example applies Lagrange's Equations of the second kind to the problem of the simple pendulum.

Example 3.2: Lagrangian with generalized coordinates

The generalized coordinate ξ is chosen as the angle θ. Looking at the problem from an energy perspective allows us to setup a Lagrangian L consisting of kinetic and potential energy

$$L = \frac{1}{2}ml^2\dot{\theta}^2 + mgl\cos(\theta).$$

Using Lagrange's equations of the second kind yields a single equation of motion

$$ml^2\ddot{\theta} + mg\sin(\theta) = 0. \tag{3.10}$$

The resulting equation of motion is both more elegant and simple than the ones derived by the direct Newton approach.

Example 3.2 uses polar coordinates as generalized coordinates. The radius is fixed at length l. Hence the angle θ is the only dynamic variable. Since there is only one DOF, θ is the minimal set of generalized coordinates. The reduction in coordinates eliminated the dependency and, by extension, the requirement of identifying tension T.

The disadvantage of generalized coordinates is that even though the number of DOFs is known, there is no systematic way of obtaining the generalized coordinates. Moreover, in systems containing non-holonomic constraints, there is no set of generalized coordinates with cardinality equal to the number of DOF that describe the motion of the system. Reiterating Example 3.2 using Cartesian coordinates would yield two ODEs with an algebraic relation between the coordinates, i. e., a DAE system.

Many systems, mechanical and otherwise, naturally form a DAE system. There exist different classes of DAE systems, but standard for all of them are the algebraic relations that complicate the evaluation of the ODE. The most common classification of DAE systems is the *Differential Index*.

Definition 3.6. *Differential Index*
Given a semi-explicit DAE system on the following form,

$$\dot{\boldsymbol{x}} = \boldsymbol{f}\left(\boldsymbol{x}, \boldsymbol{y}\right), \tag{3.11}$$

$$0 = \boldsymbol{c}\left(\boldsymbol{y}\right). \tag{3.12}$$

The differential index of the DAE system is the number of times that the algebraic part must be differentiated before an explicit ODE is obtained[28, 70, 133]

In [214] the authors state that the difficulty in solving a DAE increases with the Differential Index. The authors Gear and Petzold [71] suggested that an index reduction is necessary for indices higher than one. A rigid constraint between two vehicles can be defined solely based on the generalised coordinates. Hence, it is a holonomic constraint, and both coordinate reduction and constraint enforcement are possible strategies for reducing the Differential Index. In such cases, the constraints require explicit handling. The fundamental way of handling constraint explicitly is by using Lagrange's equations of the first kind.

$$\frac{\mathrm{d}}{\mathrm{d}t}\frac{\mathrm{d}}{\mathrm{d}\dot{\xi}_i}L - \frac{\mathrm{d}}{\mathrm{d}\xi_i}L - \lambda\frac{\mathrm{d}}{\mathrm{d}\xi_i}c\left(\boldsymbol{\xi}\right) = 0 \text{ for } i \in \boldsymbol{\xi}. \tag{3.13}$$

Eq. (3.13) implements the constraint $c\left(\boldsymbol{\xi}\right)$ into the equation by employing Lagrangian multipliers λ.

> **Example 3.3: Lagrangian: Simple Pendulum with Cartesian Coordinates**
>
> The Lagrangian L of the problem in Cartesian coordinates reads,
>
> $$L = \frac{1}{2} m \left(\dot{x}^2 + \dot{y}^2 \right) + mg \left(l - y \right). \tag{3.14}$$
>
> The pendulum constraint restated as follows,
>
> $$c \left(\boldsymbol{\xi} \right) = x^2 + y^2 - l^2 = 0. \tag{3.7 restated}$$
>
> Using Eq. (3.13) the following two equations are obtained
>
> $$\ddot{x} = \frac{2x}{m} \lambda,$$
> $$\ddot{y} = \frac{2y}{m} \lambda + mg. \tag{3.15}$$
>
> The constraint has to be imposed on acceleration level, so the constraint Eq. (3.7) is differentiated
>
> $$\ddot{c} \left(\boldsymbol{\xi}, \dot{\boldsymbol{\xi}}, \ddot{\boldsymbol{\xi}} \right) \ : \ \ddot{x}x + \dot{x}^2 + \ddot{y}y + \dot{y}^2 = 0. \tag{3.16}$$
>
> Substituting the accelerations from Eq. (3.15) into the constraint yields an expression for λ
>
> $$\lambda = - \frac{mgy + mv^2}{l^2}. \tag{3.17}$$

The multiplier expression of Eq. (3.17) is the same as was obtained in Example 3.1. However, unlike the Newtonian approach, the procedure to include the constraint was directly deducted from the equations.

The system derived by Lagrange's Equations of the first kind Eq. (3.15) along with the constraint Eq. (3.7) contains the Lagrangian multiplier as an independent algebraic variable. Bringing the expression to implicit form yields:

$$\boldsymbol{f} \left(\dot{\boldsymbol{x}}, \boldsymbol{x}, \lambda \right) = 0. \tag{3.18}$$

In the context of the differential index of Def. 3.6, the λ belongs to the state vector $\boldsymbol{x}$. Effectively, this means the system is a DAE that contains no information on $\dot{\lambda}$. The system equations Eq. (3.15) combined with the constraint Eq. (3.7) constitute a DAE of index 3. A mechanical system with holonomic constraints often exhibits a specific structure classification called Hessenberg DAE of Index-3.

$$\dot{\boldsymbol{x}} = \boldsymbol{f} \left(\boldsymbol{x}, \boldsymbol{y} \right),$$
$$\dot{\boldsymbol{y}} = \boldsymbol{k} \left(\boldsymbol{x}, \boldsymbol{y}, \boldsymbol{z} \right), \tag{3.19}$$
$$0 = \boldsymbol{c} \left(\boldsymbol{x} \right).$$

The DAE of Example 3.3 is a Hessenberg DAE of Index-3 of Eq. (3.19) with $\boldsymbol{x} = [x, y]$, $\boldsymbol{y} = [\dot{x}, \dot{y}]$ and $z = \lambda$. In Example 3.3 the constraint was differentiated

twice to reduce the system to an index-1 formulation. The solution to the index-1 formulation is then obtained by either differentiating the constraint one more time and thereby derive a direct expression for $\dot{\lambda}$. Otherwise, the Lagrangian multiplier λ is isolated and eliminated from the ODE part of the system.

Unfortunately, the process of transforming a system from index-3 to index-1 requires differentiation, which removes information from the system. Instead of imposing the constraint on configuration level, the constraint is transformed into its acceleration equivalent. From a geometric perspective, a holonomic constraint $\boldsymbol{c}\left(\boldsymbol{\xi}\right)$ and its derivatives $\dot{\boldsymbol{c}}\left(\boldsymbol{\xi},\dot{\boldsymbol{\xi}}\right)$ and $\ddot{\boldsymbol{c}}\left(\boldsymbol{\xi},\dot{\boldsymbol{\xi}},\ddot{\boldsymbol{\xi}}\right)$ can be seen as manifolds as follows:

$$
\begin{aligned}
\mathcal{M} &= \{\boldsymbol{\xi} \mid \boldsymbol{c}\left(\boldsymbol{\xi}\right) = 0\}, \\
\dot{\mathcal{M}} &= \{\boldsymbol{\xi},\dot{\boldsymbol{\xi}} \mid \dot{\boldsymbol{c}}\left(\boldsymbol{\xi},\dot{\boldsymbol{\xi}}\right) = 0\}, \\
\ddot{\mathcal{M}} &= \{\boldsymbol{\xi},\dot{\boldsymbol{\xi}},\ddot{\boldsymbol{\xi}} \mid \ddot{\boldsymbol{c}}\left(\boldsymbol{\xi},\dot{\boldsymbol{\xi}},\ddot{\boldsymbol{\xi}}\right) = 0\}.
\end{aligned}
\tag{3.20}
$$

The Lagrangian multipliers act on the system such that it maintains the acceleration constraint $\ddot{\boldsymbol{c}}\left(\boldsymbol{\xi},\dot{\boldsymbol{\xi}},\ddot{\boldsymbol{\xi}}\right) = 0$. In a sense, the Lagrangian multiplier acts as a controller that steer the acceleration $\ddot{\boldsymbol{\xi}}$ to the manifold $\ddot{\mathcal{M}}$. The initial conditions are within the respective manifolds $\boldsymbol{\xi}_0 \in \mathcal{M}$ and $\dot{\boldsymbol{\xi}}_0 \in \dot{\mathcal{M}}$ then the manifolds are invariant[18]. However, due to numerical inaccuracies in the integration procedure, this is not achievable. Since the constraints are only enforced on acceleration level any perturbation away from the manifolds $\mathcal{M}$ and $\dot{\mathcal{M}}$ will result in the system never returning to the manifold again.

The index reduction and subsequent elimination of the Lagrangian multipliers effectively ensure the enforcement of the acceleration level constraint. The acceleration level constraint is assumed to be Pfaffian [238], such that,

$$
\boldsymbol{\Phi}\ddot{\boldsymbol{\xi}} = \boldsymbol{b}.
\tag{3.21}
$$

If the constraint complies with the restriction, then the system can be written in matrix form as follows:

$$
\overbrace{\begin{bmatrix} \boldsymbol{M} & \boldsymbol{\Phi}^T \\ \boldsymbol{\Phi} & \boldsymbol{0} \end{bmatrix}}^{\bar{\boldsymbol{M}}} \begin{bmatrix} \ddot{\boldsymbol{\xi}} \\ \boldsymbol{\lambda} \end{bmatrix} = \begin{bmatrix} \boldsymbol{X} \\ \boldsymbol{b} \end{bmatrix},
\tag{3.22}
$$

where $\boldsymbol{X}$ is the generalized forces acting on the system. A solution to the system of Eq. (3.22) would be an inversion of the matrix $\bar{\boldsymbol{M}}$. In that case, the following expression determines the Lagrangian multiplier vector:

$$
\boldsymbol{\lambda} = -\left(\boldsymbol{\Phi}\boldsymbol{M}^{-1}\boldsymbol{\Phi}^T\right)^{-1}\left(\boldsymbol{b} - \boldsymbol{\Phi}\boldsymbol{M}^{-1}\boldsymbol{X}\right).
\tag{3.23}
$$

Two things are evident; the constraint matrix $\boldsymbol{\Phi}$ must be full row rank, and the matrix $\boldsymbol{M}$ must be non-singular. The matrix $\boldsymbol{M}$ is non-singular and invertible for mechanical systems. However, depending on the parameterizations of the system the otherwise non-singular mass matrix can become singular. The rank condition of the matrix $\boldsymbol{\Phi}$ is necessary for matrix $\bar{\boldsymbol{M}}$ to be invertible [148].

The invertibility condition on the mass matrix appears trivially fulfilled in mechanical systems. However, this is not always the case as reported by Betsch and Siebert [22], and as exemplified here:

Example 3.4: Singularity of Inertia Matrix

The Quaternion rotation parametrization was introduced in Chapter 2.
The kinetic energy associated with the angular dynamics is defined as follows,

$$T = \frac{1}{2} \left(\boldsymbol{\omega}_{b/n}^b \right)^T \boldsymbol{I}_g \boldsymbol{\omega}_{b/n}^b, \tag{3.24}$$

where $\boldsymbol{I}_g$ is the is the inertia tensor. The transformation between the body angular velocities were defined in Eq. (2.13) and the inverse operation is defined as,

$$\boldsymbol{\omega}_{b/n}^b = 2\boldsymbol{H}\dot{\boldsymbol{q}}. \tag{3.25}$$

From Eq. (3.25) and (2.13) the kinetic energy of the angular dynamics can be re-written as,

$$T = 2\dot{\boldsymbol{q}}^T \overbrace{\boldsymbol{H}^T \boldsymbol{I}_g \boldsymbol{H}}^{\boldsymbol{I}_g^n} \dot{\boldsymbol{q}}, \tag{3.26}$$

where $\boldsymbol{I}_g^n$ is the inertia tensor in the inertial frame. As the matrices $\boldsymbol{H}$ and $\boldsymbol{I}_g$ are rank three, the rank of their product can only become less than or equal of rank, i. e., three or less. However, the dimension of $\boldsymbol{I}_g^n$ is four by four, which means it's rank deficient, singular and not invertible. Thus the inertia matrix $\bar{\boldsymbol{M}}$ can become singular.

Example 3.4 shows that the invertibility of the inertia matrix depends on the parameterizations of the attitude. It is interesting to note that the very parametrization employed to avoid singularities in the transformation matrix $\boldsymbol{T}$ is causing the singularity in the transformed inertia tensor.

Example 3.4 also reveals, how employing generalized coordinates can complicate the derivation of the equations of motion. Eq. (3.26) eliminated the body-fixed angular velocities $\boldsymbol{\omega}_{b/n}^b$ in favor of an expression depending on the generalized velocities $\dot{\boldsymbol{q}}$. However, the transformation $\boldsymbol{T}$ required for this substitution complicates the resulting equations of motion. The introduction of *quasi-velocities* allows for a reformulation that reduces the complication of the terms.

Definition 3.7. *Quasi-Velocities [160, 31, 87, 24]*
There exists a linear transformation parameterized in the general coordinates $\boldsymbol{\xi}$, such that,

$$s^j \sum_{i=1}^{n} a_i^j \dot{\xi}^i + a_{n+1}^j \; for \; j \in \{1, \ldots, m\}, \tag{3.27}$$

where s^j is the jth index of the quasi-velocities.

Hamel [76] was one of the first to formulate the quasi-velocities in the form of Eq. (3.27). However, according to Whittaker [235], quasi-coordinates were already known to Euler and Lagrange for special cases.

Definition 3.7 allows a change of velocity coordinates. However, the newly obtained velocities are not integrable. Thereby, $\int s dt$ cannot be integrated to yield a complete configuration - a set of generalized coordinates - of the system in the global frame. Hence, the transformed velocities are called *quasi*-velocities since they are velocities of quasi-coordinates.

Concerning the marine vehicle modeling of Chapter 2, the vector $\boldsymbol{\eta}$ denotes the configuration of a marine vehicle, and $\boldsymbol{\nu}$ denotes the body-fixed velocities. In the notation of mechanics, the generalized coordinates are equal to the pose vector $\boldsymbol{\xi} = \boldsymbol{\eta}$, and the body-fixed velocities are equal to the quasi-velocities $\boldsymbol{s} = \boldsymbol{\nu}$.

3.2 Elimination of Lagrange's multipliers

The problem of constrained dynamics has received much attention since the introduction of Lagrange's equations of the first kind. Section 3.1 introduced some of the fundamental ideas of constrained dynamics. Specifically, it showed the application of Lagrange's Equations of the first kind and the subsequent elimination of the multipliers from the equations of motion. The elimination procedure presented so far is sometimes called the *index-1 method* [117].

$$\boldsymbol{M}\ddot{\boldsymbol{\xi}} + \boldsymbol{\Phi}^T \boldsymbol{\lambda} = \boldsymbol{F}. \tag{3.28}$$

Many different approaches have been proposed to describe motion of mechanical systems with non-holonomic constraints. One early method was developed by Maggi [125], who proposed to employ quasi-velocities to split the system into a matrix system as follows:

$$\begin{bmatrix} \boldsymbol{0} \\ \boldsymbol{s} \end{bmatrix} = \begin{bmatrix} \boldsymbol{\Phi} \\ \boldsymbol{G}(\boldsymbol{\xi}) \end{bmatrix} \dot{\boldsymbol{\xi}} + \begin{bmatrix} \boldsymbol{b} \\ \hat{\boldsymbol{b}} \end{bmatrix}, \tag{3.29}$$

where $\boldsymbol{s}$ is a vector of kinematic characteristics, $\boldsymbol{G}(\boldsymbol{\xi})$ is a transformation matrix in the generalized coordinates $\boldsymbol{\xi}$. The vector $\boldsymbol{s}$ fulfills the requirements of quasi-velocities from Def. 3.7. The top-row equation is the constraint on the differential form (non-holonomic form) such that

$$\boldsymbol{\Phi}\dot{\boldsymbol{\xi}} + \boldsymbol{b} = \boldsymbol{0}. \tag{3.30}$$

The matrix composed of $\boldsymbol{\Phi}$ and $\boldsymbol{G}\left(\boldsymbol{\xi}\right)$ is assumed invertible and the inverted matrix can be split into

$$\begin{bmatrix} \boldsymbol{\Phi} \\ \boldsymbol{G}\left(\boldsymbol{\xi}\right) \end{bmatrix}^{-1} = \begin{bmatrix} \boldsymbol{\Gamma}_1 & \boldsymbol{\Gamma}_2 \end{bmatrix}. \tag{3.31}$$

Following the standard properties of the product between a matrix and their invertible maps yields:

$$\begin{bmatrix} \boldsymbol{\Phi} \\ \boldsymbol{G}\left(\boldsymbol{\xi}\right) \end{bmatrix} \begin{bmatrix} \boldsymbol{\Gamma}_1 & \boldsymbol{\Gamma}_2 \end{bmatrix} = \begin{bmatrix} \boldsymbol{\Phi}\left(\boldsymbol{\xi}\right)\boldsymbol{\Gamma}_1 & \boldsymbol{\Phi}\left(\boldsymbol{\xi}\right)\boldsymbol{\Gamma}_2 \\ \boldsymbol{G}\left(\boldsymbol{\xi}\right)\boldsymbol{\Gamma}_1 & \boldsymbol{G}\left(\boldsymbol{\xi}\right)\boldsymbol{\Gamma}_2 \end{bmatrix} = \begin{bmatrix} \boldsymbol{I} & \boldsymbol{0} \\ \boldsymbol{0} & \boldsymbol{I} \end{bmatrix}. \tag{3.32}$$

The $\boldsymbol{\Phi}\left(\boldsymbol{\xi}\right)\boldsymbol{\Gamma}_2 = \boldsymbol{0}$ implies that the columns of $\boldsymbol{\Gamma}_2$ lie in the Null-space of the constraint Jacobian $\boldsymbol{\Phi}$, which is a central property of Maggi's method.

$$\dot{\boldsymbol{\xi}} = \boldsymbol{\Gamma}_2\boldsymbol{s} - \overbrace{\left(\boldsymbol{\Gamma}_1\boldsymbol{b} + \boldsymbol{\Gamma}_2\hat{\boldsymbol{b}}\right)}^{\boldsymbol{d}}. \tag{3.33}$$

Differentiating the $\dot{\boldsymbol{\xi}}$ yields an expression for the accelerations of the generalized coordinates $\ddot{\boldsymbol{\xi}}$:

$$\ddot{\boldsymbol{\xi}} = \dot{\boldsymbol{\Gamma}}_2\boldsymbol{s} + \boldsymbol{\Gamma}_2\dot{\boldsymbol{s}} - \dot{\boldsymbol{d}}, \tag{3.34}$$

and by inserting into Eq. (3.28) to obtain:

$$\boldsymbol{M}\left(\dot{\boldsymbol{\Gamma}}_2\boldsymbol{s} + \boldsymbol{\Gamma}_2\dot{\boldsymbol{s}} - \dot{\boldsymbol{d}}\right) = \boldsymbol{F} - \boldsymbol{\Phi}^T\left(\boldsymbol{\xi}\right)\boldsymbol{\lambda}. \tag{3.35}$$

From Eq. (3.32), the $\boldsymbol{\Gamma}_2$ was orthogonal to the constraint matrix $\boldsymbol{\Phi}$, as the matrix belongs to the null-space. Hence, pre-multiplying Eq. (3.35) with $\boldsymbol{\Gamma}_2^T$ eliminates the Lagrangian multiplier,

$$\boldsymbol{\Gamma}_2^T\boldsymbol{M}\dot{\boldsymbol{\Gamma}}_2\boldsymbol{s} + \boldsymbol{\Gamma}_2^T\boldsymbol{M}\dot{\boldsymbol{\Gamma}}_2\dot{\boldsymbol{s}} = \boldsymbol{\Gamma}_2^T\boldsymbol{M}\dot{\boldsymbol{d}} + \boldsymbol{\Gamma}_2^T\boldsymbol{F}. \tag{3.36}$$

One advantage of Maggi's method is the ability to maintain constraints on a velocity-level as opposed to other methods that impose the constraint on acceleration level. Thereby, Maggi's method handles systems described on index-2 formulations, which adds stability compared to other methods. The disadvantage of Maggi's method is the non-uniqueness of the kinematic characteristics, which are often difficult to find [67]. Furthermore, finding the null-space basis $\boldsymbol{\Gamma}_2$ is costly, yet this problem has been addressed in the literature [67]. Several other methods exist and have been described by [117], and all of them depend on the elimination of the Lagrangian multipliers.

Maggi's method is uncommon in the control literature. However, the method was rediscovered by [95, 96] under the name *Kane's Equation*.

All modeling approaches lead to the same trajectories, and as such, the different approaches can often be derived from each other as noted in a series of papers discussing the equivalence between Kane's Equations and the Gibbs-Appell Equations [44, 45, 189, 119, 81, 15, 43, 173]. Subsequently, Borri, Bottasso, and Mantegazza [25] showed the equivalence between Kane's method and Maggi's method.

Section 3.1 discussed the foundation of constrained dynamics, namely Lagrange's Equation of the First Kind. However, it also showed that Lagrange's basic formulation could lead to issues such as non-unique multipliers or even no solution depending on the mass matrix.

3.3 Gauss' Principle of Least Constraint

Gauss' Principle of least constraint is a reformulation of classical mechanics [69]. The principle provides the foundation for the derivation of the Udwadia-Kalaba Formulation of constrained dynamics [91]. The principle of least constraint has not received much attention, despite the fact, that it provides a more general formulation than that of d'Alembert [159].

The principle states that the constrained acceleration $\ddot{\boldsymbol{\xi}}$ is the acceleration which minimizes the *Zwang* of the system, where the Zwang Z is the sum of square error between the constrained acceleration and the unconstrained acceleration $\ddot{\boldsymbol{\xi}}_u$.

$$Z = \sum_{i=1}^{n} m_i \left(\ddot{\xi}_i - \ddot{\xi}_{u,i} \right)^2,$$

(3.37)

where n is the number of coordinates. Minimizing Z across all possible accelerations that are in concordance with the system constraint yields the actual constrained accelerations,

$$\ddot{\boldsymbol{\xi}} = \arg\min_{\ddot{\boldsymbol{\xi}} \in \mathcal{X}} Z,$$

(3.38)

where $\mathcal{X}$ is the set of accelerations that abide by the constraints of the system. The extremum of the Z-function defines the equations of motion across the free variables:

$$\frac{\partial}{\partial \ddot{\xi}_i} Z = 0 \ \forall i \in [1, N].$$

(3.39)

Example 3.5: Pendulum using Gauss' Principle

Starting with the pendulum constraint from Eq. (3.7) on acceleration form as follows,

$$\ddot{c} \; : \; x\ddot{x} + y\ddot{y} + \dot{x}^2 + \dot{y}^2 = 0. \qquad\qquad (3.16 \text{ restated})$$

The accelerations are dependent, and isolation of $\ddot{x}$ reveals the relationship,

$$\ddot{x} = \frac{-y\ddot{y} - \dot{x}^2 - \dot{y}^2}{x}.$$

Choosing the generalized accelerations as follows, $\boldsymbol{\xi} = [x, y]^T$, the Z-function becomes,

$$
\begin{aligned}
Z &= \frac{1}{2} m \left(\ddot{\xi}_1 \right)^2 - \frac{1}{2} m \left(\ddot{\xi}_2 - g \right)^2, \\
&= \frac{1}{2} m \left(\frac{-y\ddot{y} - \dot{x}^2 - \dot{y}^2}{x} \right)^2 - \frac{1}{2} m \left(\ddot{y} - g \right)^2.
\end{aligned}
\qquad (3.40)
$$

The elimination of $\ddot{x}$ means that only one free variable is available, and thus Eq. (3.39) is only evaluated in $\ddot{y}$ as follows:

$$\frac{\partial Z}{\partial \ddot{y}} = \frac{ym}{x^2} \left(y\ddot{y} + \dot{x}^2 + \dot{y}^2 \right) + m \left(\ddot{y} - g \right) = 0.$$

Solving for the $\ddot{y}$ and subsequently Eq. (3.16) to obtain $\ddot{x}$ yields:

$$
\begin{aligned}
\ddot{y} &= -\frac{\left(\dot{x}^2 + \dot{y}^2 \right) y - g x^2}{x^2 + y^2}, \\
\ddot{x} &= -\frac{\left(\dot{x}^2 + \dot{y}^2 + yg \right) x}{x^2 + y^2}.
\end{aligned}
\qquad (3.41)
$$

The equations of motion obtained from Gauss' Principle is exactly the same as those of Example 3.1.

Example 3.5 shows the principle applied to the simple pendulum. The constraint manifolds define the set of consistent accelerations $\mathcal{X}$ for the pendulum. Fig. 3.2 shows an example of the constraint manifolds for a specific point. The manifold $\mathcal{M}$ is the set of all allowable configurations of the pendulum, that is anywhere on the circle with radius l. Evaluating the tangent manifold at the specific point $x = 0, y = l$ yields a tangent to the circle at the point. The tangent space of every point in the configuration manifold yields the tangent manifold $\dot{\mathcal{M}}$,

$$\dot{\mathcal{M}} \Big|_{\substack{y=l, \\ x=0}} = \{ \dot{x}, \dot{y} \mid l\dot{y} = 0 \} \; \rightarrow \dot{x} \in \mathbb{R}, \; \dot{y} = 0. \qquad (3.42)$$

The tangent constraint requires $\dot{y}$ to be zero, but $\dot{x}$ is not constrained. Evaluating the double time derivative of the tangent manifold at the specific configuration

imposed by the constraint manifolds $\mathcal{M}$ and $\dot{\mathcal{M}}$ yields the acceleration in the acceleration-space which abide by the constraints $\mathcal{X}$.

$$\mathcal{X} = \ddot{\mathcal{M}}\Big|_{\substack{y=l \\ x=0 \\ \dot{y}=0}} = \{\ddot{x}, \ddot{y} \mid l\ddot{y} + \dot{x}^2 = 0\} \ \rightarrow \ddot{x} \in \mathbb{R}, \ \ddot{y} = -\frac{\dot{x}^2}{l}. \tag{3.43}$$

Eq. (3.43) shows the $\ddot{x}$ to be unconstrained while $\ddot{y}$ is constrained by $-\frac{\dot{x}^2}{l}$. Minimizing Z over allowable $\ddot{x}$ and $\ddot{y}$ yields:

$$\ddot{x} = 0, \ \ddot{y} = -\frac{\dot{x}^2}{l}.$$

The results obtained in Eq. (3.41) are identical when using the position and velocities that are consistent with the constraints. Gauss' Principle of Least Constraint
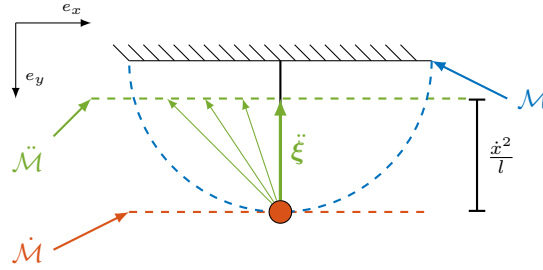
Figure 3.2: Constraint manifolds for the simple pendulum.

is a true minimum principle, and the formulation holds for non-holonomic, as well as, holonomic constraints [115]. Commonly, the Gibbs-Appell Equations is cited as an implementation of Gauss' Principle. However, it was Gibbs who derived the equations using Gauss' Principle, while Appell deduced them from Lagrange's principle [161].

3.3.1 Udwadia Kalaba Formulation

The Udwadia-Kalaba Formulation is derived based on Gauss' Principle of Least Constraint. For convenience, the Z-function is formulated in vector form as follows:

$$Z = \left(\ddot{\boldsymbol{\xi}} - \ddot{\boldsymbol{\xi}}_u\right)^T \boldsymbol{M} \left(\ddot{\boldsymbol{\xi}} - \ddot{\boldsymbol{\xi}}_u\right). \tag{3.44}$$

The constraints are expressed on acceleration level to identify the

$$\boldsymbol{\Phi}\ddot{\boldsymbol{\xi}} = \boldsymbol{b}. \tag{3.21 restated}$$

Any holonomic constraint can be expressed linearly in the accelerations. The expression of Z can be significantly simplified by introducing scaled error accelerations on the form:

$$\boldsymbol{e} = \boldsymbol{M}^{1/2} \left(\ddot{\boldsymbol{\xi}} - \ddot{\boldsymbol{\xi}}_u\right). \tag{3.45}$$

Thus the new Z-function to minimize can be written as:

$$Z = \boldsymbol{e}^T \boldsymbol{e}. \tag{3.46}$$

Inverting the relationship in Eq. (3.45) yields:

$$\ddot{\boldsymbol{\xi}} = \boldsymbol{M}^{-1/2} \left(\boldsymbol{e} + \ddot{\boldsymbol{\xi}}_u \right), \tag{3.47}$$

and inserting into the constraint equation Eq. (3.21) yields:

$$\boldsymbol{\Phi} \boldsymbol{M}^{-1/2} \boldsymbol{e} = \boldsymbol{b} - \boldsymbol{\Phi} \ddot{\boldsymbol{\xi}}_u. \tag{3.48}$$

The solution to Eq. (3.48) is readily given by the pseudo-inverse of the $\boldsymbol{\Phi} \boldsymbol{M}^{-1/2}$:

$$\boldsymbol{e} = \left(\boldsymbol{\Phi} \boldsymbol{M}^{-1/2} \right)^+ \left(\boldsymbol{b} - \boldsymbol{\Phi} \ddot{\boldsymbol{\xi}}_u \right). \tag{3.49}$$

The pseudo-invers exist for any matrix [168], and thus Eq. (3.49) always exhibit a solution. Transforming back into accelerations yields the Udwadia-Kalaba Formulation:

$$\ddot{\boldsymbol{\xi}} = \ddot{\boldsymbol{\xi}}_u + \boldsymbol{M}^{-1/2} \left(\boldsymbol{\Phi} \boldsymbol{M}^{-1/2} \right)^+ \left(\boldsymbol{b} - \boldsymbol{\Phi} \ddot{\boldsymbol{\xi}}_u \right). \tag{3.50}$$

The advantage of the Udwadia-Kalaba Formulation is that use of the pseudo-inverse determines the projection onto the manifold. The properties of the pseudo-inverse ensure that a solution always exists, even if the constraint formulation contains redundancies. The price of the Moore-Penrose pseudo-inverse is the computational demand, which is often calculated using Singular Value Decomposition (SVD). In other words, the computational requirement of the Udwadia-Kalaba method is higher than comparable methods. However, Laulusa and Bauchau [117] noted that the full rank Choleksy factorization method [39] reduce the required computational time of the pseudo-inverse.

The Udwadia-Kalaba Equations formulated in Eq. (3.50) employs generalized coordinates. As was shown in Example 3.4, the mass-matrix of a system can become singular when parameterized in more than the minimum number of generalized coordinates. Udwadia and Phohomsiri [222] considered the problem of the singular mass matrix, and specifically for Quaternions in Udwadia and Schutte [226, 225]. In both cases, the performed constraint derivation takes place in the global frame. The authors Udwadia and Phohomsiri [223] note that sometimes it's convenient to express the system on quasi-form, and so the Udwadia-Kalaba was extended to quasi-accelerations and quasi-velocities [223, 224]. Handling the kinetic part of the system in the local body-fixed frame ensures the parameters of $\boldsymbol{D}$, $\boldsymbol{M}$ and $\boldsymbol{g}$ are time-invariant, and the inertia matrix M does not become singular.

In the following, the notation will revert to that of Chapter 2, where $\boldsymbol{\eta} = \boldsymbol{\xi}$, $\boldsymbol{\nu} = \boldsymbol{s}$. The transformation matrix $\boldsymbol{J}(\boldsymbol{\eta})$ from Eq. (2.16) is the quasi-velocity transformation from Def. 3.7.

$$\boldsymbol{M} \dot{\boldsymbol{\nu}}_u = \boldsymbol{f}_b^b. \tag{3.51}$$

The subscript $(\cdot)_u$ denotes the unconstrained quantities, such that, $\dot{\boldsymbol{\nu}}_u$ is the vector of unconstrained quasi-accelerations, $\boldsymbol{M} \in \mathbb{R}^{n_\nu \times n_\nu}$ is the inertia matrix, and $\boldsymbol{f}_b^b \in \mathbb{R}^{n_\nu}$ is the generalized forces vector acting on the body. It is important to notice, that the model is equivalent to the model of Eq. (2.27) for single vehicle systems. However, the model of Eq. (3.51) also applies to multi-vehicle systems with $\boldsymbol{M}$ being a block-diagonal matrix. The formulation in Eq. (3.51) can be transformed to a constrained formulation when exposed to constraints by merely augmenting it with an additional term:

$$\boldsymbol{M}\dot{\boldsymbol{\nu}}_c = \boldsymbol{f}_b^b + \bar{\boldsymbol{f}}_b^b, \tag{3.52}$$

where $\bar{\boldsymbol{f}}_b^b \in \mathbb{R}^{n_\nu}$ is a vector of constraint forces. The challenge is then to calculate $\bar{\boldsymbol{f}}_b^b$ such that both the system dynamics and the constraints are respected. The Udwadia-Kalaba Equations require the constraint formulation to be on acceleration level and in this case quasi-accelerations.

$$\boldsymbol{\Phi}\left(\boldsymbol{\eta},\boldsymbol{\nu}\right)\dot{\boldsymbol{\nu}} = \boldsymbol{b}\left(\boldsymbol{\eta},\boldsymbol{\nu}\right). \tag{3.53}$$

Following Eq. (3.49), the compensation force $\bar{\boldsymbol{f}}_b^b$ is identified by the following equation:

$$\bar{\boldsymbol{f}}_b^b = \boldsymbol{M}^{1/2}\left(\boldsymbol{\Phi}\boldsymbol{M}^{-1/2}\right)^+ \left(\boldsymbol{b} - \boldsymbol{\Phi}\dot{\boldsymbol{\nu}}_u\right). \tag{3.54}$$

The constrained quasi-accelerations is then identified by substituting into Eq. (3.52) and solving for $\dot{\boldsymbol{\nu}}_c$ as follows,

$$\dot{\boldsymbol{\nu}}_c = \dot{\boldsymbol{\nu}}_u + \underbrace{\boldsymbol{M}^{-1/2}\left(\boldsymbol{\Phi}\boldsymbol{M}^{-1/2}\right)^+ \left(\boldsymbol{b} - \boldsymbol{\Phi}\dot{\boldsymbol{\nu}}_u\right)}_{\boldsymbol{g}(\dot{\boldsymbol{\nu}}_u,\ \boldsymbol{\nu}_c,\ \boldsymbol{\eta})}. \tag{3.55}$$

Three observations are evident from Eq. (3.55). First, the constrained acceleration $\dot{\boldsymbol{\nu}}_c$ is the sum of the unconstrained acceleration $\dot{\boldsymbol{\nu}}_u$ and a constraining term that depends on the unconstrained acceleration. Secondly, it is clear that the Udwadia-Kalaba framework requires global knowledge of all states, which have implications when applied in a control context.

Thirdly, by setting $\boldsymbol{M} = \boldsymbol{I}$ in Eq. (3.55) it becomes evident, that the $\boldsymbol{g}\left(\dot{\boldsymbol{\nu}}_u,\ \boldsymbol{\nu}_c,\ \boldsymbol{\eta}\right)$ is a projection onto the constraint manifold,

$$\dot{\boldsymbol{\nu}}_c = \dot{\boldsymbol{\nu}}_u + \left(\boldsymbol{\Phi}\right)^+ \left(\boldsymbol{b} - \boldsymbol{\Phi}\dot{\boldsymbol{\nu}}_u\right), \tag{3.56}$$

where $\left(\boldsymbol{\Phi}\right)^+ \boldsymbol{\Phi}$ is the orthogonal projector onto the range of $\boldsymbol{\Phi}^T$. The following section will define and derive the constraint necessary for describing the multibody system.

3.4 Modeling of Modular Underwater Robots

The Udwadia-Kalaba Formulation facilitates a modular approach to synthesizing a model and allows easy swapping of the constraints. The existence and robustness

of the constraint forces, even under rank deficiency in the constraint matrix, makes the method very attractive.

The modular concept of the underwater robots allows them to attach and detach from each other. The connection between them is rigid and, thereby, suppresses all relative motion.

Def. 3.8 formulates the definition of the rigid constraint.
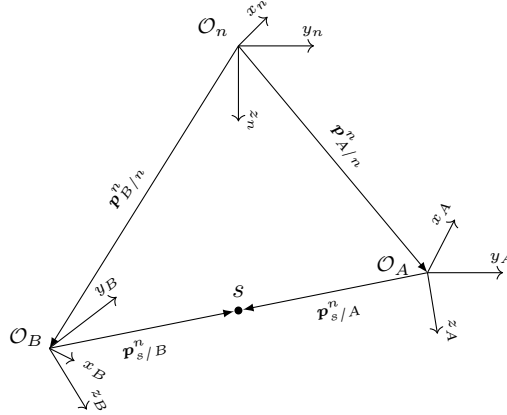
Figure 3.3: Constraint vector loop, $\mathcal{O}_n$ is the origin of the inertial space, $\mathcal{O}_i$ for $i \in \{A, B\}$ the origin of each vehicle. The point s is a common connection point between the vehicles.

Definition 3.8. *Rigid Constraint*
A rigid constraint is a constraint which restricts all relative motion between two rigid bodies.

In essence, the definition means that the two rigid bodies become one rigid body and the necessary number of constraints to formulate is all six relative DOFs. The rigid constraint fulfills Def. 3.5 of the holonomic constraints, and thus in principle, a coordinate reduction is possible. However, any change in the system structure as a consequence of detachment and re-attachment at another location would require synthesizing new sets of equations. The Udwadia-Kalaba formulation handles the structural change directly through the constraint matrix rather than through the dynamic equations themselves.

3.4.1 Rigid Constraint Formulation

Two vehicles denoted $\{A\}$ and $\{B\}$ respectively are introduced to support the derivation of the constraint, each with a local body-fixed frame attached. Since the rigid constraints restrict all relative motion, it is a purely geometric constraint. The constraint defines a relative distance and orientation between the two vehicles.

For the relative distance, the two vehicles maintain a distance to a mutual point s defined in the inertial frame. The relative distance formulation allows for the development of a loop-closure as shown in Fig. 3.3

The rotational constraint maintains a relative orientation between the vehicles. As the orientation is parametrized using quaternions, the relative orientation between them is the Hamilton product $\otimes$ between the quaternion of vehicle A and the conjugate quaternion of vehicle B. The constraints are summarized as follows:

$$c_1 \; : \; \boldsymbol{p}_{A/n}^n + \boldsymbol{p}_{s/A}^n - \boldsymbol{p}_{B/n}^n - \boldsymbol{p}_{s/B}^n = 0, \tag{3.57}$$

$$c_2 \; : \; \boldsymbol{q}^{(A)} \otimes \left(\boldsymbol{q}^{(B)}\right)^* = \tilde{\boldsymbol{q}}, \tag{3.58}$$

where $\boldsymbol{q}^{(A)}$ is the unit quaternion of vehicle A, $\left(\boldsymbol{q}^{(B)}\right)^*$ is the quaternion conjugate of vehicle B, and $\tilde{\boldsymbol{q}}$ is the relative rotation between vehicle A and B. As was shown in Sec. 3.3.1 the constraint formulation is required and enforced on acceleration level.

To bring the constraints of Eq. (3.57) and (3.58) on the form of (3.21) a double derivate with respect to time is required. Conducting the first time-differentiation on Eq. (3.57) and recalling that $\dot{\boldsymbol{R}}_b^n = \boldsymbol{S}(\boldsymbol{\omega}_{b/n}^n)\boldsymbol{R}_b^n$ yields:

$$\dot{\boldsymbol{p}}_{A/n}^n = \boldsymbol{R}_A^n \boldsymbol{\nu}_{A/n}^A, \tag{3.59}$$

$$\dot{\boldsymbol{p}}_{s/A}^n = \boldsymbol{\omega}_{A/n}^n \times \boldsymbol{p}_{s/A}^n. \tag{3.60}$$

Performing the first time derivative of the expressions (3.59) and (3.60) yields:

$$\ddot{\boldsymbol{p}}_{A/n}^n = \boldsymbol{R}_A^n \dot{\boldsymbol{\nu}}_{A/n}^A + \boldsymbol{\omega}_{A/n}^n \times \boldsymbol{R}_A^n \boldsymbol{\nu}_{A/n}^A,$$

$$\ddot{\boldsymbol{p}}_{s/A}^n = \dot{\boldsymbol{\omega}}_{A/n}^n \times \boldsymbol{p}_{s/A}^n + \boldsymbol{\omega}_{A/n}^n \times \left(\boldsymbol{\omega}_{A/n}^n \times \boldsymbol{p}_{s/A}^n\right).$$

For brevity, this section only shows the derivation of the constraint for vehicle A. However, due to symmetry, the derivation of the constraint for vehicle B mirrors that of vehicle A with but with opposite signs. Adding together the expressions allows for the synthesis of the constraint matrix $\boldsymbol{\Phi}$ for constraint c_1

$$\boldsymbol{\Phi}_1 = \begin{bmatrix} \boldsymbol{R}_A^n & -\boldsymbol{S}(\boldsymbol{p}_{s/A}^n) & -\boldsymbol{R}_B^n & \boldsymbol{S}(\boldsymbol{p}_{s/B}^n) \end{bmatrix} \tag{3.61}$$

The remaining terms of the expression form the constraint vector $\boldsymbol{b}$

$$\begin{aligned} \boldsymbol{b}_1 = &-\boldsymbol{\omega}_{A/n}^n \times (\boldsymbol{R}_A^n \boldsymbol{\nu}_{A/n}^A + \boldsymbol{\omega}_{A/n}^n \times \boldsymbol{p}_{s/A}^n) \\ &+ \boldsymbol{\omega}_{B/n}^n \times (\boldsymbol{R}_B^n \boldsymbol{\nu}_{B/n}^B + \boldsymbol{\omega}_{B/n}^n \times \boldsymbol{p}_{s/B}^n) \end{aligned} \tag{3.62}$$

Moving to the orientation constraint c_2, the Hamilton product between the unit quaternion of A and the conjugate of the unit quaternion of B yields the relative rotation between the vehicles. The time-differentiation of the attitude constraint yields:

$$\dot{\boldsymbol{q}}^{(A)} \otimes \left(\boldsymbol{q}^{(B)}\right)^* + \boldsymbol{q}^{(A)} \otimes \left(\dot{\boldsymbol{q}}^{(B)}\right)^* = \boldsymbol{0}$$

Conducting the second time derivative of the constraint along with a reduction yields:

$$\ddot{\boldsymbol{q}}^{(A)} \otimes \left(\boldsymbol{q}^{(B)}\right)^* + \boldsymbol{q}^{(A)} \otimes \left(\ddot{\boldsymbol{q}}^{(B)}\right)^* + 2\left(\dot{\boldsymbol{q}}^{(A)} \otimes \left(\dot{\boldsymbol{q}}^{(B)}\right)^*\right) = \boldsymbol{0} \qquad (3.63)$$

To express the resulting terms on the form in Eq. (3.21) a change of frame is necessary such that the quaternion change is in the quasi-velocity form

$$\ddot{\boldsymbol{q}} = \boldsymbol{T}_q \dot{\boldsymbol{\omega}}_{b/n}^b + \dot{\boldsymbol{T}}_q \boldsymbol{\omega}_{b/n}^b \qquad (3.64)$$

For convenience, the $\bar{\boldsymbol{H}}$ matrix is introduced as follows:

$$\bar{\boldsymbol{H}}^{(i)} = \begin{bmatrix} -\boldsymbol{\varepsilon}^{(i)} & \eta^{(i)} \boldsymbol{I}_3 + \boldsymbol{S}\left(\boldsymbol{\varepsilon}^{(i)}\right) \end{bmatrix} \text{ for } i \in \{A, B\}, \qquad (3.65)$$

notice the sign of the skew-symmetric matrix in $\bar{\boldsymbol{H}}$ has implications for the frame of rotation. The $\boldsymbol{H}$ matrix of Eq. (2.15) rotates the quaternion from global frame to the angular velocity of the local frame, while $\bar{\boldsymbol{H}}$ rotates from global frame to the angular velocity of the local frame relative to the global frame axes as follows,

$$\boldsymbol{\omega}_{b/n}^b = 2\boldsymbol{H}\dot{\boldsymbol{q}},$$
$$\boldsymbol{\omega}_{b/n}^n = 2\bar{\boldsymbol{H}}\dot{\boldsymbol{q}}.$$

The newly defined matrix allows for re-writing the relative rotation between two quaternions into linear form as follows:

$$\boldsymbol{q}^{(A)} \otimes \left(\boldsymbol{q}^{(B)}\right)^* = \begin{bmatrix} \left(\boldsymbol{q}^{(B)}\right)^T \\ \bar{\boldsymbol{H}}^{(B)} \end{bmatrix} \boldsymbol{q}^{(A)} = \boldsymbol{G}^{(B)}\boldsymbol{q}^{(A)}$$
$$= \begin{bmatrix} \left(\boldsymbol{q}^{(A)}\right)^T \\ -\bar{\boldsymbol{H}}^{(A)} \end{bmatrix} \boldsymbol{q}^{(B)} = \boldsymbol{G}^{(A)}\boldsymbol{q}^{(B)}. \qquad (3.66)$$

Applying the linear form to and combining the expressions in Eq. (3.63) and (3.64) yields:

$$2\left(\dot{\boldsymbol{q}}^{(A)} \otimes \left(\dot{\boldsymbol{q}}^{(B)}\right)^*\right) = 2\begin{bmatrix} \left(\boldsymbol{T}_q^{(B)}\boldsymbol{\omega}_{B/n}^B\right)^T \\ \dot{\bar{\boldsymbol{H}}}^{(B)} \end{bmatrix} \boldsymbol{T}_q^{(A)}\boldsymbol{\omega}_{A/n}^A$$
$$= 2\dot{\boldsymbol{G}}^{(B)}\boldsymbol{T}_q^{(A)}\boldsymbol{\omega}_{A/n}^A. \qquad (3.67)$$

The terms containing the second time derivative of the quaternions are brought into a linear form to accommodate the requirement of Eq. (3.21) as follows:

$$\ddot{\boldsymbol{q}}^{(A)} \otimes \left(\boldsymbol{q}^{(B)}\right)^* = \boldsymbol{G}^{(B)}\boldsymbol{T}_q^{(A)}\dot{\boldsymbol{\omega}}_{A/n}^A + \boldsymbol{G}^{(B)}\dot{\boldsymbol{T}}_q^{(A)}\boldsymbol{\omega}_{A/n}^A,$$
$$\boldsymbol{q}^{(A)} \otimes \left(\ddot{\boldsymbol{q}}^{(B)}\right)^* = \boldsymbol{G}^{(A)}\boldsymbol{T}_q^{(B)}\dot{\boldsymbol{\omega}}_{B/n}^B + \boldsymbol{G}^{(A)}\dot{\boldsymbol{T}}_q^{(B)}\boldsymbol{\omega}_{B/n}^B.$$

Finally, the matrix and vector $\boldsymbol{A}_2$ and $\boldsymbol{b}_2$ associated with the constraints of $\boldsymbol{c}_2$ becomes:

$$\boldsymbol{\Phi}_2 = \begin{bmatrix} \boldsymbol{0}_{4\times3} & \boldsymbol{G}^{(B)}\boldsymbol{T}_q^{(A)} & \boldsymbol{0}_{4\times3} & \boldsymbol{G}^{(A)}\boldsymbol{T}_q^{(B)} \end{bmatrix} \tag{3.68}$$

$$\boldsymbol{b}_2 = -\boldsymbol{G}^{(A)}\dot{\boldsymbol{T}}_q^{(B)}\boldsymbol{\omega}_{B/n}^B - \left(\boldsymbol{G}^{(B)}\dot{\boldsymbol{T}}_q^{(A)} + 2\dot{\boldsymbol{G}}^{(B)}\boldsymbol{T}_q^{(A)} \right)\boldsymbol{\omega}_{A/n}^A \tag{3.69}$$

Every rigid constraint between two bodies in the system consist of the matrices $\boldsymbol{\Phi}_1$ and $\boldsymbol{\Phi}_2$ and vectors $\boldsymbol{b}_1$ and $\boldsymbol{b}_2$ parameterized using the state vectors of the respective bodies.

3.5   Simulator Development

Up to now, the focus has been on the individual models that comprise the entire system. A simulator is needed to evaluate and compare the behavior of the multi-body system. Since the applied modeling method relies on force compensation, the simulator keeps track of the complete state vector for all vehicles. The vectors containing all the states and inputs of the system are defined as follows:

$$\dot{\boldsymbol{\nu}}_u = [\dot{\boldsymbol{\nu}}_u^{(1)}, \dots, \dot{\boldsymbol{\nu}}_u^{(i)}] \quad \dot{\boldsymbol{\nu}}_c = [\dot{\boldsymbol{\nu}}_c^{(1)}, \dots, \dot{\boldsymbol{\nu}}_c^{(i)}]$$
$$\boldsymbol{\nu}_c = [\dot{\boldsymbol{\nu}}_c^{(1)}, \dots, \dot{\boldsymbol{\nu}}_c^{(i)}] \quad \dot{\boldsymbol{\eta}}_c = [\dot{\boldsymbol{\eta}}_c^{(1)}, \dots, \dot{\boldsymbol{\eta}}_c^{(i)}]$$
$$\boldsymbol{u} = [\boldsymbol{u}^{(1)}, \dots, \boldsymbol{u}^{(i)}]$$

where $\boldsymbol{u}^{(i)}$ is the input vector containing the actuation forces and moments $\boldsymbol{\tau}$ for vehicle i, $\dot{\boldsymbol{\nu}}_u^{(i)}$ is the vector of unconstrained acceleration of vehicle i, $\dot{\boldsymbol{\nu}}_c^{(i)}$ is the vector of constrained acceleration of vehicle i. The vehicle subsystems are build from the dynamic model of Eq. (2.27). For clarity, a vheicle subsystem is denoted $\mathcal{H}_i$ with i being the vehicle index and is defined as follows,

$$\mathcal{H}_i \ : \Big\{ \ \boldsymbol{M}^{(i)}\dot{\boldsymbol{\nu}}_u^{(i)} + \boldsymbol{D}^{(i)}(\boldsymbol{\nu}_c^{(i)})\boldsymbol{\nu}_c^{(i)} + \boldsymbol{C}^{(i)}(\boldsymbol{\nu}_c^{(i)})\boldsymbol{\nu}_c^{(i)} + \boldsymbol{g}^{(i)}(\boldsymbol{\eta}_c^{(i)}) = \boldsymbol{\tau}^{(i)} \quad \text{Eq. (2.27)}$$
$$\tag{3.70}$$

Fig. 3.4 shows a block diagram of the simulator. First, each vehicle receives an input vector $\boldsymbol{u}$, the constrained state vector $\boldsymbol{\eta}_c$ and the constrained velocity vector $\boldsymbol{\nu}$, which is then simulated without constraints to obtain the unconstrained accelerations $\dot{\boldsymbol{\nu}}_u$. Secondly, the Udwadia-Kalaba is invoked to calculate the constrained accelerations $\dot{\boldsymbol{\nu}}_c$, which is then integrated to obtain the constrained body-velocities $\boldsymbol{\nu}_c$. After that, the body-velocities are transformed using the kinematic transformation to obtain the constrained state derivates $\dot{\boldsymbol{\eta}}_c$. Finally, another integration yields the constrained state vector $\boldsymbol{\eta}_c$.

3.6   Simulation Verification

The simulator is implemented and requires verification. Two simulations are conducted to test the constraint maintenance and infer if the behavior is as expected. The two cases denoted **Case A**, and **Case B** are:
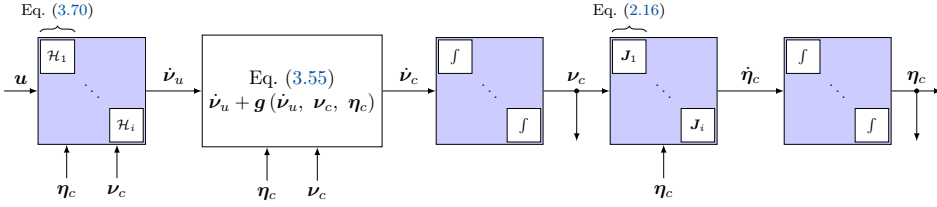
Figure 3.4: Block diagram of the simulation setup. The input vector $\boldsymbol{u}$ containing the thruster PWM signals is fed to the system in Eq. (3.70), which calculate the unconstrained accelerations $\dot{\boldsymbol{\nu}}_u$. The unconstrained accelerations is then used in the Udwadia-Kalaba Formulation to produce the constrained accelerations $\dot{\boldsymbol{\nu}}_c$.

Case A: Hydrostatic Simulation

Case B: Open-Loop Maneuver Simulation

The first simulation is a hydrostatic simulation, where force inputs $\boldsymbol{\tau}$ are zero, and only the restoring force vector $\boldsymbol{g}(\boldsymbol{\eta})$ is actuating the system. The second simulation is in open-loop arbitrary force input $\boldsymbol{\tau}$, and the dynamic parameters of the vehicles are varied.

Table 3.2: Initial conditions and thrust output for each vehicle in each simulation

Cases	Initial States	Thrust
Case A	$\boldsymbol{\eta}^{(A)} = [0, 0, 0, 1, 0, 0, 0]$ $\boldsymbol{\eta}^{(B)} = [0, l, 0, 0.707, 0.707, 0, 0]$	$\boldsymbol{\tau}^{(A)} = [0, 0, 0, 0, 0, 0]$ $\boldsymbol{\tau}^{(B)} = [0, 0, 0, 0, 0, 0]$
Case B	$\boldsymbol{\eta}^{(A)} = [0, 0, 0, 1, 0, 0, 0]$ $\boldsymbol{\eta}^{(B)} = [0, 1, 0, 1, 0, 0, 0]$	$\boldsymbol{\tau}^{(A)} = [1, 0, 0, 0, 0, 0]$ $\boldsymbol{\tau}^{(B)} = [1, 0, 0, 0, 0, 0]$

The configuration of the subsystems composing the interconnected system is shown in Fig. 3.5a and Fig. 3.5b for case A & B respectively.

3.6.1 Case A: Hydrostatic Simulation

Case A simulates two vehicles A and B connected by a massless rod of length l with relative attitude of 90° around the roll axis. The mass of each vehicle is 20kg, the buoyancy point $\boldsymbol{r}_b^b = [0, 0, -0.1]$ in each vehicles local frame and both vehicles are neutrally buoyant. The initial attitude of vehicle B is 90° around the roll axis. Hence, the initial attitude of vehicle A is 0° roll. The relative angular displacement between the vehicles is 90° in the relative roll. Since the dynamic profile is the same for both vehicles, the restoring forces will exert an equal and opposite torque on each vehicle when the roll angles are equal and opposite. In the specific case, this angle is $\phi_A = -45°$ and $\phi_B = 45°$. Furthermore, the period of the roll oscillations depends on the distance between the vehicles. A comparison between the simulator and an analytical solution offers some insight into the accuracy of the simulator. The symmetric design of the experimental setup allows for the derivation of an

(a) Hydrostatic Test Configuration: Vehicle B is rotated relative to vehicle A such that axis y_A and z_B coincide.

(b) Hydrodynamic Test Configuration: The attitude of both vehicles are identical such that axis y_A and y_B coincide.
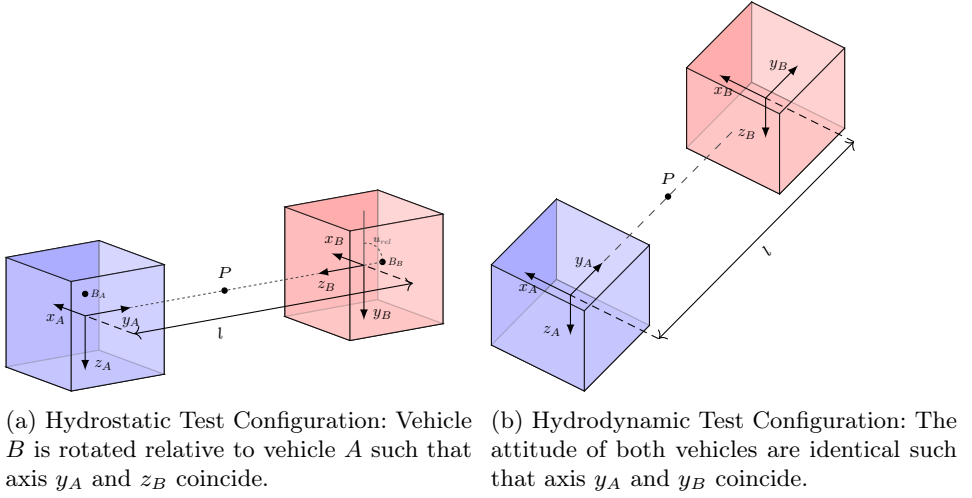
Figure 3.5: Two configurations containing two vehicles denoted A and B. In both configurations vehicle A is colored blue and vehicle B is colored red.

Table 3.3: Dynamic Parameters used in the hydrostatic simulation

$X_{\dot{u}}$ $[kg]$	2.5	X_u $\left[\frac{kg}{s}\right]$	5
$Y_{\dot{v}}$ $[kg]$	2.5	Y_v $\left[\frac{kg}{s}\right]$	5
$Z_{\dot{w}}$ $[kg]$	2.5	Z_w $\left[\frac{kg}{s}\right]$	5
$K_{\dot{p}}$ $[kgm]$	0.0005	K_p $\left[\frac{kgm}{s}\right]$	0.001
$M_{\dot{q}}$ $[kgm]$	0.0005	M_q $\left[\frac{kgm}{s}\right]$	0.001
$N_{\dot{r}}$ $[kgm]$	0.0005	N_r $\left[\frac{kgm}{s}\right]$	0.001
m $[kg]$	20	I_{xx} $[m^2kg]$	0.001
I_{yy} $[m^2kg]$	0.001	I_{zz} $[m^2kg]$	0.001
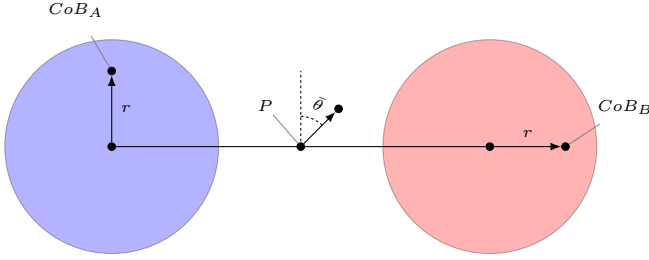
Figure 3.6: The hydrostatic equilibrium is the product of the relative location of the resulting CoB with respect to the location of the resulting CoM. The expected equilibrium angle is denoted $\bar{\theta}$ relative to baseline.

equivalent analytical solution for comparison. The point P of Fig. 3.6 is the CoM of the system, and it is equivalent to the center of rotation occurring as a result of the gravity actuation. Thereby, the system is re-modeled as a pendulum-like system as shown in Fig. 3.7. The multi-body problem is formulated using Gibbs-Appell's Equations.

The resulting motion is both rotational and translational. The hydrodynamic damping acts tangentially to the motion of the pendulum. For this reason, it is advantageous to model the motion in polar coordinates as follows,

$$\boldsymbol{r} = [r\cos(\theta),\ r\sin(\theta)]^T. \tag{3.71}$$

The radial and tangential coordinate frames are thereby:

$$\hat{\boldsymbol{r}} = \frac{\frac{\partial \boldsymbol{r}}{\partial r}}{\left\|\frac{\partial \boldsymbol{r}}{\partial r}\right\|} = [\cos(\theta),\ \sin(\theta)]^T, \hat{\boldsymbol{\theta}} = \frac{\frac{\partial \boldsymbol{r}}{\partial \theta}}{\left\|\frac{\partial \boldsymbol{r}}{\partial \theta}\right\|} = [-\sin(\theta),\ \cos(\theta)]^T. \tag{3.72}$$

The acceleration of the bob in the polar coordinates is then:

$$\frac{\mathrm{d}^2\boldsymbol{r}}{\mathrm{d}t^2} = \ddot{r} - r\dot{\theta}^2\hat{\boldsymbol{r}} + 2\dot{r}\dot{\theta} + r\ddot{\theta}\hat{\boldsymbol{\theta}}. \tag{3.73}$$

The radial DOF is unimportant for the analysis, and only the tangential part of the system is derived.

$$\ddot{\xi}_1 = r\ddot{\theta}\hat{\boldsymbol{\theta}} \tag{3.74}$$

The Z of the system is then defined as:

$$Z = \frac{m}{2}\ddot{\xi}_1^2 - (Q_1 + R_1)\ddot{\xi}_1, \tag{3.75}$$

where Q_1 and R_1 are the generalized forces, and constraint forces acting on the DOF. The restoring force vector acts on the bob. However, the point of rotation is at the point P. The restoring torque in the idealized case is:

$$\tau_\theta = \tilde{r}_y^b mg\cos(\theta) - \tilde{r}_z^b mg\sin(\theta), \tag{3.76}$$

where $\tilde{r}_y^b$, and $\tilde{r}_z^b$ is the y and z components of the difference between the CoM and CoB of the bob. The damping forces acting on the bob in the tangential direction is the linear and quadratic drag, and no constraints affect the tangential axis,

$$Q_1 = \frac{\tau_\theta}{r} - D_L r \dot{\theta} - D_Q r^2 |\dot{\theta}|\dot{\theta}, \ R_1 = 0. \tag{3.77}$$

Inserting Eq. (3.74) into Eq. (3.75) and applying Eq. (3.39) with respect to $\ddot{\theta}$ yields:

$$\frac{\partial Z}{\partial \ddot{\theta}} = m r^2 \ddot{\theta} + \tau_\theta - D_L r^2 \dot{\theta} - D_Q r^3 |\dot{\theta}|\dot{\theta} = 0.$$

Isolating the rotational acceleration $\ddot{\theta}$ yields the equation of motion:

$$\begin{aligned}
\ddot{\theta} &= -\frac{\tau_\theta}{ml^2} - \frac{D_Q l |\dot{\theta}|\dot{\theta} + D_L \dot{\theta}}{m}, \\
&= -\frac{g}{l^2}\left(\tilde{r}_y^b \cos(\theta) - \tilde{r}_z^b \sin(\theta)\right) - \frac{D_Q l |\dot{\theta}|\dot{\theta} + D_L \dot{\theta}}{m}. \tag{3.78}
\end{aligned}$$

The rotational point P in Fig. 3.7 is the same point P as in Fig. 3.6. The relation
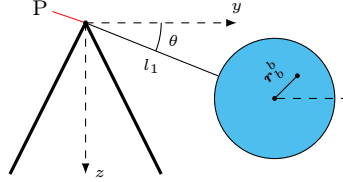
Figure 3.7: The equivalent pendulum formulation, where the dynamics of the two spheres are combined into a single sphere. The position of the CoM is l_1 distance away from the hinge at angle θ, and the CoB is positioned at $\boldsymbol{r}$ from the CoM.

between the length of l_1 of Fig. 3.7 and l of Fig. 3.5a is $l_1 = \frac{1}{2}l$. The mass m_1 of the pendulum-like formulation is equal to the combined mass of both subsystems. The CoB of the combined systems is then:

$$\begin{aligned}
\boldsymbol{r}_b^b &= \frac{m_1 \boldsymbol{r}_{b_1}^b + m_2 \boldsymbol{r}_{b_2}^b}{m_1 + m_2}, \\
&= [0.05\ , -0.05].
\end{aligned}$$

The comparison between the simulation and the analytical solution showcases the first occurring peak in the time series data. For each simulation the distance l between the vehicle changes such that $l \in \{0.5, 1, 1.5, 2, 2.5, 3\}$. Fig. 3.8 shows the roll angle of vehicle A. The roll angle is actuated negatively towards $-45°$ as was expected.
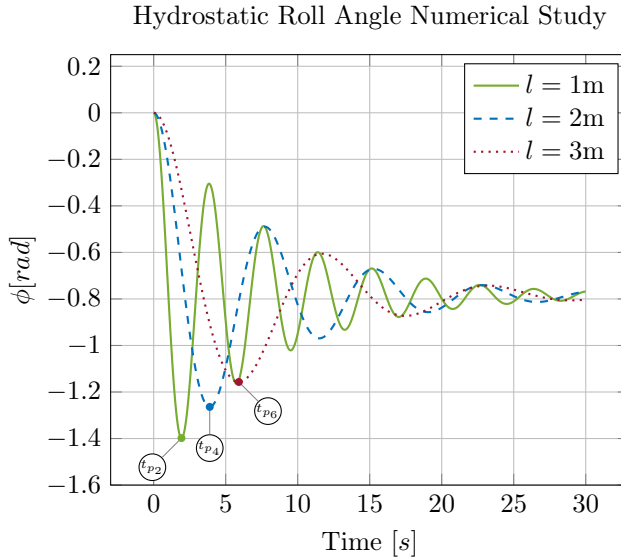
Figure 3.8: Roll angle ϕ of vehicle A for three different rod lengths l. Peak times for vehicle A are marked and coincide with those of vehicle B.

Table 3.4: Comparison of peak times between analytical approximation and Udwadia-Kalaba simulation.

Distance $[m]$	0.50	1.00	1.50	2.00	2.50	3.00
Peak Time	t_{p_1}	t_{p_2}	t_{p_3}	t_{p_4}	t_{p_5}	t_{p_6}
Simulator $[s]$	0.970	1.931	2.901	3.891	4.892	5.912
Analytical $[s]$	0.980	1.951	2.931	3.921	4.932	5.972

The time of the first peak is measured for both simulations to determine if the oscillation period is equivalent. Table 3.4 shows the resulting peak times. The simulations conducted on the Udwadia-Kalaba simulator uses full rigid-body models, whereas the analytical solution does not take into account rotational inertia of the rigid bodies. The deviation of the peak times is attributed to the missing rotational inertia in the analytical solution.

Fig. 3.9a shows the heave velocity w for vehicle A at three different distances to vehicle B. As expected the oscillation period increases as a function of the distance. The increase in oscillation period is reasonable since the inertia of the system increases as a function of distance due to the Huygens-Steiner Theorem [61, p. 50]. Fig. 3.9b shows the sway velocity v for vehicle B under the same distance as for A. The sway velocities are equal magnitude and opposite sign compared to the heave velocity of vehicle A. The results are in agreement with the expected behavior. As vehicle B is rotated $90°$ in relative roll angle in the configuration
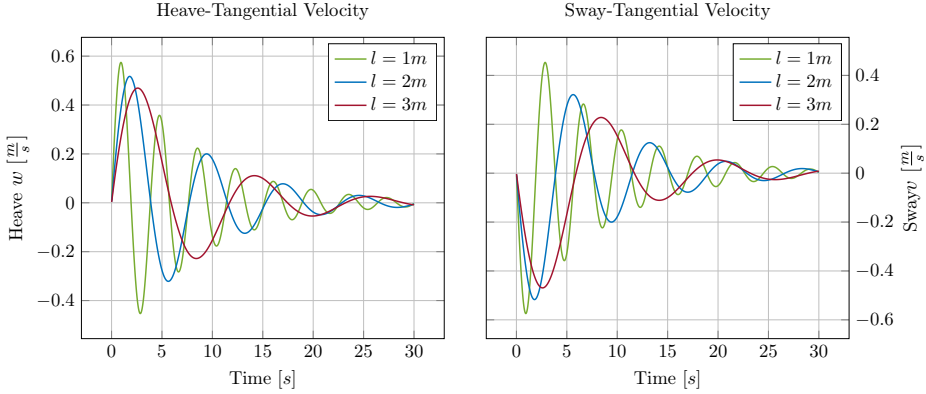
(a) Resulting heave w trajectory of vehicle A for three different distances. As expected the oscillation period increase with distance as the rotational inertia increases as a result of the Huygens-Steiner Theorem [61, p. 50].

(b) The sway velocity v of vehicle B is equal and opposite of the heave velocity of vehicle A as expected. This is agreement with the interconnection of the two vehicles.

Figure 3.9: The tangential velocity of vehicle A and B. Fig. 3.9a shows the heave velocity of vehicle A, which coincides with the tangential motion on the circle. Fig. 3.9b shows the sway velocity of vehicle B, which is tangential with the motion on the circle.

between the vehicles, the tangential axis of the circular motion is aligned with the heave and sway of vehicle A and B respectively.

3.6.2 Case B: Hydrodynamic Simulation

Case B simulates two vehicles A and B connected by a massless rod of length 1 with 0 relative attitudes. Fig. 3.5b shows the connection between the vehicles. Both vehicles exert force in positive surge direction x_b of each vehicle. As with Case A, the simulation is conducted multiple times with increasing surge damping X_u of vehicle B. The purpose of the simulation is to test the interaction between the vehicles when changes in the damping occur. The surge damping of vehicle B is chosen as $X_u \in \{5, 10, 15\}$. Fig. 3.10 shows the resulting trajectories of the simulations with three different drag parameters on vehicle B. The CoM of the connected systems is right between the vehicles, denoted with P in Fig. 3.5b. Given their identical hydrodynamic behavior, both vehicles will act on the CoM with equal and opposite torques and, hence, the sum of torques is zero. The result is a straight trajectory.

Doubling the surge damping X_u of vehicle B and conducting another simulation yields the results of Fig. 3.10 labeled Trial 2. Evidently, the trajectory diverges toward starboard. The increased surge damping of vehicle B, which is the east positioned vehicle, induces a higher yaw torque on the CoM and as expected, the trajectory drags eastwards.
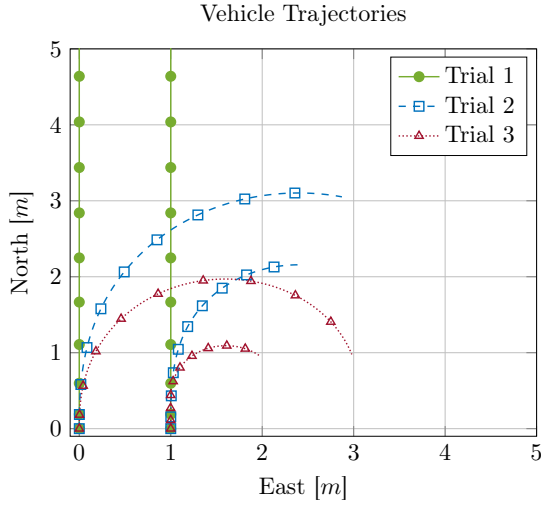
Figure 3.10: Three trajectories of open-loop simulations with varying surge damping of vehicle B.

Finally, with the damping increased threefold on vehicle B the trajectory diverges toward starboard at a higher rate. As is expected from the previous argumentation, the starboard turn increases more compared to the case when the drag is lower.

3.7   Chapter Summary

The chapter introduced the topic of constrained dynamics along with different methods for simulating systems with special structure. Furthermore, the chapter reviewed the Udwadia-Kalaba Formulation, defined and derived the rigid constraint in quasi-coordinates to comply with the requirements on the constraint formulation. The derived rigid-constraint was implemented using the Udwadia-Kalaba formulation, and a numerical study based on simulations was presented to show the validity of the implementation.

Chapter 4

Preliminary Experimental Validation

The constrained multi-body dynamics method presented in Chapter 3 couples the dynamics of multiple subsystems into an overall model that captures the main dynamics. Hence, the subsystem models must be identified for validating the overall modeling methodology.

Contribution

The contribution of this chapter is a preliminary experimental investigation, on a system comprised of two subsystems with low complexity dynamics. Two experiments are proposed and executed: A hydrostatic experimental test, where the restoring forces of the system actuate the system, and an open-loop maneuvering experiment, where exogenous force actuates the system. The analysis of both experiments compares the simulated model-equivalent motion to the measured motion. CFD analysis is employed to obtain the dynamic parameters of the modules.

The experiments were conducted at the MCLAB in June 2016.

Organization of this chapter

The organization of the chapter is as follows: Section 4.1 introduces the hull-drag and thruster model. Section 4.2 describes the implementation of the hardware in the MCLAB. Section 4.3 outlines the hydrostatic experiment and presents the results. Section 4.4 describes the open-loop maneuvering test and the results. Finally, Section 4.5 presents the chapter summary.

Publications

The material used in this chapter is based on the following publications

[C2] Mikkel Cornelius Nielsen et al. "Experimental Validation of Dynamic Multi-Body Modelling for Reconfigurable Underwater Robots". In: *Oceans 2016 MTS/IEEE*. 2016, p. 6

4.1 Validation Design

The preliminary experimental validation considers a simple system, in a hydrodynamic sense, to establish if the multi-body modeling methodology of Chapter 3 is applicable for underwater application.

The modeling methodology aggregates sub-models to build a larger combined model based on the interaction between the subsystems. The dynamic parameters of a model Any model is inevitably subject to uncertainty in the dynamic parameters and aggregating subsystems with uncertain model parameters affect the aggregated model behavior. Therefore, simplifying the dynamics of the subsystems diminishes the likelihood of errors otherwise introduced by subsystems with high complexity dynamic behavior, such as, ROVs.

The following assumptions are imposed to reduce the complexity of the subsystems:

Assumption 4.1 (Symmetry). *Subsystems contains three planes of symmetry*

Assumption 4.1 is essential as it enables the usage of drag and added mass matrices on a diagonal form. Another common assumption imposed on underwater systems is the submersion assumption

Assumption 4.2 (Submersion). *The subsystem is submerged far below the free surface.*

Assumption 4.2 removes the frequency dependent potential damping and further simplifies the individual model description. Hence, the total drag force for each degree of freedom can approximated as a linear and quadratic term shown in [61] as follows,

$$D(v) = D_L v + D_Q |v| v. \tag{4.1}$$

The purpose of the experiment is to conduct a preliminary investigation of the modeling approach before committing to a larger scale test. The validation scheme comprises of two investigations, namely an investigation into the hydrostatic behavior, and an investigation into the open-loop maneuvering behavior. The hydrostatic test is inspired by the ideas of [53], where gravity is the acting force on the system. Changes to the hydrostatic equilibrium of each subsystem will cause the aggregated system to behave like a pendulum. Thereby, the amplitude and frequency of oscillation is a result of the inertial properties of each subsystems.

The open-loop maneuvering experiment is inspired by the idea of using maneuvers to obtain data for identification [61, p. 354].
Applying a known thrust to the subsystems forms a trajectory by the aggregated system depending on the relative interconnection of the subsystems. The trajectory obtained through experimental results and simulations respectively allows for inference on the accuracy of the modeling method.

Conducting the experiments require knowledge of the actuation of each subsystem and the subsystem itself. The task is partitioned into three parts

1. **Model** Identify Drag

2. **Model** Identify Added Mass

3. **Actuator** Identify Actuator Parameters

The identification of model drag and added mass is conducted through CFD, whereas bollard pull experiments are condcuted to indetify the parameters of the actuators.

4.1.1 Identification of Hull Parameters

The identification of hull parameters includes drag coefficients and added mass coefficients. The diagonal elements of the damping matrices are determined numerically by CFD using SolidWorks Flow Simulation using the Morison equation as follows,

$$f(v) = \underbrace{\frac{1}{2}C_d\rho A\, v^2}_{D_Q},$$ (4.2)

where C_d is the drag coefficient, A is the cross-section of the vehicle, v is the velocity of the fluid across the surface, $f(v)$ is the drag force as a function of the velocity and D_Q is a collective term for the quadratic drag. The problem of determining the linear skin friction is discussed in Eidsvik and Schjølberg [52], where the authors proposes to approximate it using the scaled quadratic drag as was done by Eng et al. [53].

The scaling constant of the linear drag employed here is 16% of the quadratic drag for the translational DOF:

$$D_L = 0.16 D_Q.$$ (4.3)

For the rotational DOFs, the authors use the following relation based on [61]:

$$D_L = 2\xi m\sqrt{\frac{r}{m + m_a}},$$ (4.4)

where ξ is a damping factor in the region $2\% - 10\%$, m is the mass of the vehicle, m_a is the added mass and r is the restoring force. The restoring force r is the result of the restoring force vector $\boldsymbol{g}(\boldsymbol{\eta})$. Using the Computer-Aided-Design (CAD) model of the vehicles the CoB is determined to lie vertically above the CoM. Hence, the restoring force vector $\boldsymbol{g}(\boldsymbol{\eta})$ can be described as below [61].

$$\boldsymbol{g}(\boldsymbol{\eta}) = [0, 0, 0, \overline{BG}_z W\cos(\theta)\sin(\phi), \overline{BG}_z\sin(\theta)\cos(\phi), 0]^T,$$ (4.5)

where $\overline{BG}_z$ is the vertical distance from CoM to CoB and W is the weight of the vehicle. Since yaw has no restoring force component, the authors in [52] proposed to use the following relation,

$$N_r \approx \frac{K_p}{K_{|p|p}}N_{|r|r},$$ (4.6)

where N_r is the linear drag coefficient for the yaw-axis, K_p is the linear drag coefficient of the roll-axis, $K_{|p|p}$ is the quadratic drag of the roll-axis and $N_{|r|r}$ is the quadratic drag of the yaw-axis using the SNAME notation.

Tab. 4.1 shows the estimated hydrodynamic parameters of the hull with thruster attached. It is worth noticing that the surge damping $X_{|u|u}$ is estimated to be only

Table 4.1: Estimated dimensional parameters for the spheres in the open-loop simulation

$X_{\dot{u}}$ [kg]	6.49	$X_{|u|u}$ $[\frac{kg}{m}]$	3.8	X_u $[\frac{kg}{s}]$	0.61
$Y_{\dot{v}}$ [kg]	8.1	$Y_{|v|v}$ $[\frac{kg}{m}]$	18.9	Y_v $[\frac{kg}{s}]$	3
$Z_{\dot{w}}$ [kg]	7.41	$Z_{|w|w}$ $[\frac{kg}{m}]$	12.1	Z_w $[\frac{kg}{s}]$	1.9
$K_{\dot{p}}$ [kgm]	0.0074	$K_{|p|p}$ [kgm]	0.0082	K_p $[\frac{kgm}{s}]$	0.05
$M_{\dot{q}}$ [kgm]	0.0317	$M_{|q|q}$ [kgm]	0.05	M_q $[\frac{kgm}{s}]$	0.0353
$N_{\dot{r}}$ [kgm]	0.0453	$N_{|r|r}$ [kgm]	0.108	N_r $[\frac{kgm}{s}]$	0.0764
I_{xx} $[kgm^2]$	0.13	I_{yy} $[kgm^2]$	0.16	I_{zz} $[kgm^2]$	0.02
ξ $[-]$	0.02	$\overline{BG}_z$ [m]	-0.0114	m [kg]	14.3

20% of that of a pure sphere. Modeling flow-separation is challenging, and the reduced surge damping could be the result of this.

4.1.2 Thruster Identification

The thruster used by each subsystem is the T-200 Thruster from BlueRobotics. The expression of the thrust produced by the thruster is a quadratic function of the rotational velocity of the propeller shaft [48, 174]: :

$$f = K_T \rho D^4 |\omega|\omega, \tag{4.7}$$

where ω is the rotational velocity of the propeller shaft in Revolutions-Per-Second (RPS), D is the diameter of the propeller, ρ is the water density, and K_T is the non-dimensional propeller thrust coefficient.

Unfortunately, the T-200 thruster is not equipped to measure the RPS of the propeller. However, the input voltage to the motors can be used as a substitute variable instead of the RPS. Moreover, in Caccia, Indiveri, and Veruggio [32] the authors suggest that the dynamics of the electrical motors driving thrusters is neglectable.

Experimental bollard pull data for the T-200 thruster is available from BlueRobotics. Fig. 4.1 shows the fitting of Eq. (4.7) to the available data. The fitting shows that the model is not in agreement with the data.

Avila et al. [13] also documented the model mismatch and proposed to use the following second order polynomial without bias function:

$$\tau = K_\omega \omega + K_{|\omega|\omega}|\omega|\omega. \tag{4.8}$$

Fig. 4.1 shows the T-200 data from BlueRobotics, as well as, fittings of the models from Eq. 4.7 and Eq. (4.8). BlueRobotics produced bollard pull data by submerging
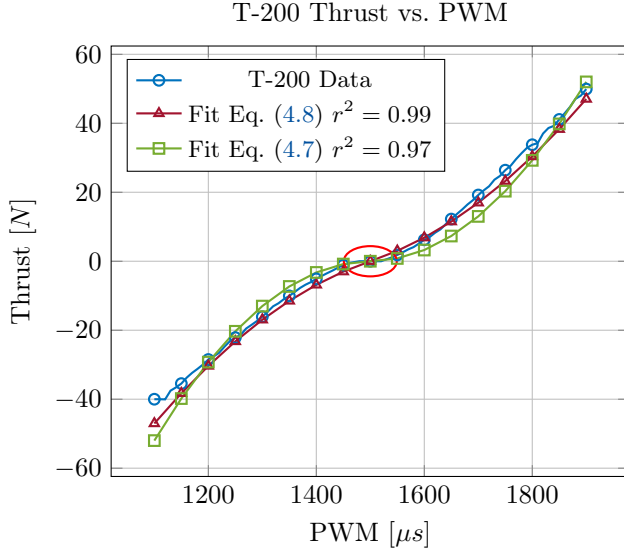
Figure 4.1: Figure shows the raw BlueRobotics T-200 Thrust vs. PWM, as well as, fittings for the models of Eq. (4.8) and Eq. (4.7). The modified model of Eq. (4.8) yields best residuals. The T-200 data exhibits a dead-zone behavior around $1500 \pm 20\mu s$ marked by a circle.

the thruster on a rod. Consequently, any thruster-hull interaction effects are not part of the provided data, and for this reason, this chapter conducts new hull-specific bollard tests.

4.2 Experimental Implementation

The experiments were conducted in the MCLAB located at the NTNU.

The chosen geometry of the subsystem hulls is spherical to avoid any complex hydrodynamic behavior. A sphere is geometrically simple as the surface is smooth and uniform. Furthermore, the sphere has three planes of symmetry and thereby assumption 4.1 is valid. This choice of hull geometry considerably reduces the required number of parameters to identify. By reducing the parameter space the uncertainty of the dynamics automatically reduces as well. The hydrostatic test does not require actuation, and for this reason, the T-200 thruster mount is designed to be easily attached and detached. The connection between the subsystems is a metal rod measuring $0.596m$ in length and weighing $500g$. MCLAB features an optical underwater motion tracking system from Qualisys. The Qualisys system measures position of multiple markers, attached to module, from multiple perspectives and triangulates the positions to produce a full pose measurement. The

experiments employs the tracking system to capture the motion of the spheres with submilimeter position error.

4.3 Hydrostatic Experiment

The purpose of the hydrostatic test is to investigate the interaction between the two bodies, with identical hydrodynamic profiles, actuated only by the gravity vector $\boldsymbol{g}$. The restoring force vector generates the actuation, which allows for the removal of the thrusters and thereby ensuring the concordance of Assumption 4.1. Fig. 4.2a
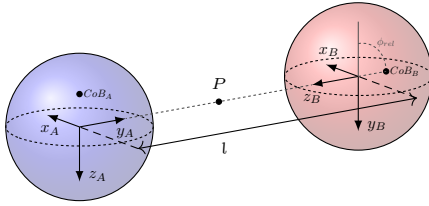
(a) Hydrostatic Experiment Configuration: Vehicle B is rotated relative to vehicle A by ϕ_{rel} such that axis y_A and z_B coincide.
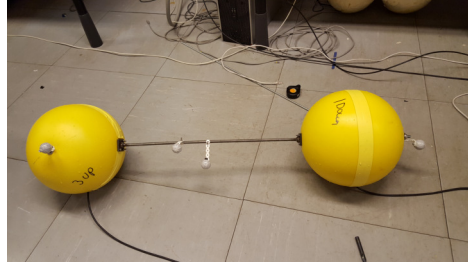
(b) The hydrostatic test setup with Qualisys markers attached. Mirroring the illustration of 4.2a, subsystem A is the left-most sphere, and subsystem B is the right-most sphere.

Figure 4.2: The illustration 4.2a shows the configuration for the hydrostatic experimentl, whereas 4.2b shows the actual implementation of the system.

shows the interconnection of the subsystems without the thrusters. The point P between the subsystems is the common point in the rigid-constraint, and ideally, it intersects with the CoM of the combined system. The right-most subsystem B was attached at an rotated roll angle of 90° relative to subsystem A around the local x_B-axis (roll). Ideally, the relative rotation results in the CoB of subsystem A and B to be placed at $CoB_A 1$ and CoB_B respectively.

The actuation of the system is then the product of the forces induced by the gravity-vector $\boldsymbol{g}(\boldsymbol{\eta})$.

The hydrostatic experiments are performed by fully submerging the connected robots into the water and positioning the connecting rod parallel to the water surface. The markers used by the tracking system are strategically attached to allow robust detection of the pose. Upon initializing the motion data capture, the system was released, and the restoring forces began acting on the bodies[1].

4.3.1 Results & Discussion

The experiments were conducted five times with data captured for approximately two minutes per experiment. The hydrodynamic parameters of the hull sans thruster are adapted from the parameters in Tab. 4.1 and shown in Tab. 4.2. The surge DOF

---

[1]Video of a hydrostatic experimental run: https://youtu.be/LIwqB7WIbFE

is the only direction, where the thruster attachment does not directly influence the flow However, the quadratic hull damping parameter is only $3.8[\frac{kg}{m}]$, which is approximately 20% of the expected drag of a sphere.

Fig. 4.3 shows the comparison between the roll angle ϕ from the simulation using the parameters of Tab. 4.2, and a dataset from the experiments. The oscil-

Hydrostatic Trajectory
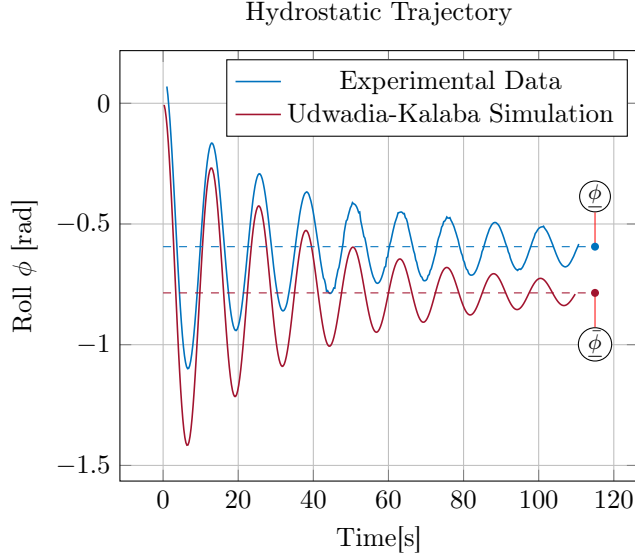
Figure 4.3: The figure shows a comparative plot between one pass of the hydrostatic experiments and a simulated counterpart. The oscillations of the actual system data and simulation are in good agreement. The angle $\underline{\phi}$ denotes the equilibrium angle of the measured data, while $\bar{\phi}$ denotes the equilibrium angle of the simulation.

lation period of the simulation matches that of the real data very well. However, the equilibrium offset is shifted. $\underline{\phi}$ (---) and $\bar{\phi}$ (---) marks the equilibrium roll angle for the measured data, and the simulation respectively. From Fig. 4.3, the equilibrium angles are read as:

$$\underline{\phi} = -0.594 \approx -34°,$$
$$\bar{\phi} = \frac{\pi}{2} = -45°.$$

The significant offset in equilibrium angle is the result of uncertainty on the gravity vectors. Neutral buoyancy is an essential part of the experiment. The necessary buoyancy material to keep the submodule neutral buoyant was calculated before the experiment and inserted into the hull. The calculation was deliberately conservative, such that, the subsystems were positively buoyant. Thus, more weight was applied to the subsystem to ensure neutral buoyancy. The applied weight was only attached to the rightmost subsystem. The space available to attach weight on the module was limited and this meant that there was a shift in the CoM of that

subsystem. The larger peak-to-peak amplitudes appear during the initial swings, where the velocity of the translational motion is largest, which suggest an underestimated quadratic damping. The reverse is true for the peak-to-peak amplitudes from 80 to 110 seconds, where the peak-to-peak of the experimental data is larger than the simulation, this suggests an overestimation of the linear drag coefficient.

Tuning the model parameters allows a better comparison between the simulation and the measured data. The two hulls are assumed to share the same damping profile, and the restoring force vector on the leftmost subsystem is assumed accurate. The assumptions reduce the parameter space enough to allow for parameter identification. The parameter vector $\boldsymbol{\theta}$ comprise of the two restoring vector parameters, $\tilde{r}_y^b$, and $\tilde{r}_z^b$, as well as, the quadratic damping coefficient $D_{|v|v}$, and the linear drag coefficient D_v:

$$\boldsymbol{\theta} = [\tilde{r}_y^b, \tilde{r}_z^b, D_{|v|v}, D_v]^T. \tag{4.9}$$

The objective function is the sum of square error between the time samples of the data ϕ, and the data $\bar{\phi}$:

$$J = \sum_{k=0}^{N-1} \left(\phi_k - \bar{\phi}_k \right)^2, \tag{4.10}$$

where k is the sample, N is the total length of the data series, ϕ_k is the data point at sample k, and $\bar{\phi}_k$ is the simulation datapoint at sample k. The fitting resulted in an optimal parameter vector $\boldsymbol{\theta}^*$ as follows,

$$\boldsymbol{\theta}^* = [-0.0016, -0.00886, 9.2889, 0.2265]^T. \tag{4.11}$$

The estimation increases the quadratic drag parameter and reduces the linear drag coefficient as was predicted based on the first simulation. Furthermore, the restoring vector components move towards the CoM of the combined system and slightly upwards:

$$\boldsymbol{r}_b^b = \frac{\boldsymbol{r}_{A/b}^b + \boldsymbol{r}_{B/b}^b}{2} = [0, 0.0044339, -0.00654]^T, \tag{4.12}$$

The resulting restoring force vector has a relative angle to the global z-axis:

$$\bar{\phi} = \arctan\left(\frac{0.0044339}{-0.00654}\right) \approx -34°, \tag{4.13}$$

which is the same equilibrium angle as the experimental data. Fig. 4.4 show the fitted model compared to the fitting data, and another dataset used as validation data. The simulation fits very well with both the fitting and the validation data. The fitted model is evaluated against the rest of the data sets by usage of the Mean Square Error (MSE).

Tab. 4.3 lists the resulting MSE between the experimental data and the simulation. The considerable distance between the modules minimizes likelihood of proximity induced interaction. Furthermore, the cross-section of the connecting rod was minimal compared to the modules themselves; this was done to minimize the influence of the rod. In a realistic scenario, however, the connecting structure would be more substantial to obtain sufficient strength, and certainly add more dynamics to the system.
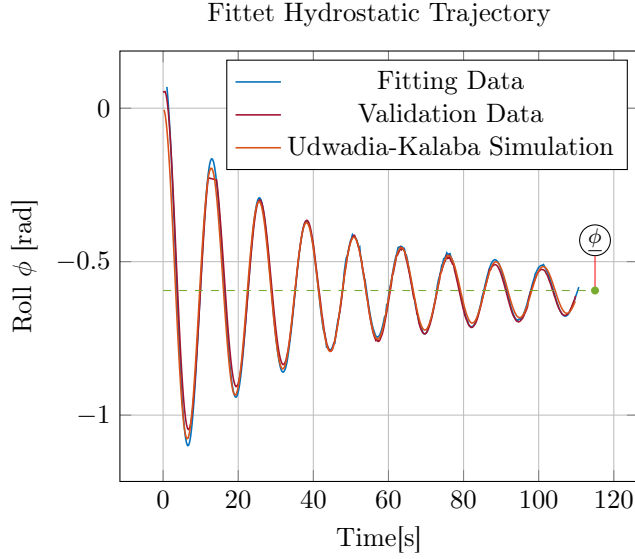
Figure 4.4: The plot shows the fittet model with the fitting data itself, and another dataset from the experiments. The oscillation period, and amplitude of the oscillations are very similar to both datasets. The ϕ angle intersects with the equilibrium of all three graphs.

Table 4.2: Estimated dimensional parameters for the spheres in the hydrostatic simulation.

$X_{\dot{u}}$ [kg]	7.06	$X_{|u|u}$ $[\frac{kg}{m}]$	3.8	X_u $[\frac{kg}{s}]$	0.67
$Y_{\dot{v}}$ [kg]	7.06	$Y_{|v|v}$ $[\frac{kg}{m}]$	3.8	Y_v $[\frac{kg}{s}]$	0.67
$Z_{\dot{w}}$ [kg]	7.06	$Z_{|w|w}$ $[\frac{kg}{m}]$	3.8	Z_w $[\frac{kg}{s}]$	0.67
$K_{\dot{p}}$ [kgm]	0.0	$K_{|p|p}$ [kgm]	0.0082	K_p $[\frac{kgm}{s}]$	0.048
$M_{\dot{q}}$ [kgm]	0.0	$M_{|q|q}$ [kgm]	0.0082	M_q $[\frac{kgm}{s}]$	0.048
$N_{\dot{r}}$ [kgm]	0.0	$N_{|r|r}$ [kgm]	0.0082	N_r $[\frac{kgm}{s}]$	0.048

Table 4.3: Mean Square Error between simulation and data.

Run	1	2	3	4	5
MSE	0.002	0.0042	0.0038	0.0154	0.0064

4.4 Open-Loop Maneuvering Experiment

The purpose of the open-loop maneuvering experiment was to test the modeling methodology under exogenous actuation.

The addition of exogenous actuation required the identification of the actuators prior to comparing the simulated open-loop trajectories with the obtained data. Open water performance charts for the T-200 Thruster are available on BlueRobotics product page[2]. However, the thrusters in the experiment are mounted in close proximity to the hull of the subsystems. The hull interferes with the flow across the propellers, and as a result the forces exerted by thruster changes.

The hull-thruster interaction of the two differently sized subsystem hulls is measured by conducting bollard pull tests with the thrusters attached to the respective hulls. The subsystem with thruster is mounted on a fitting as shown in Fig. 4.5, and lowered from the MCLAB towing carriage into the water of the tank. The thrust force is measured by three load cells, attached to the fitting and the MCLAB towing carriage. The sum of the forces measured by the load cells yields the total force:
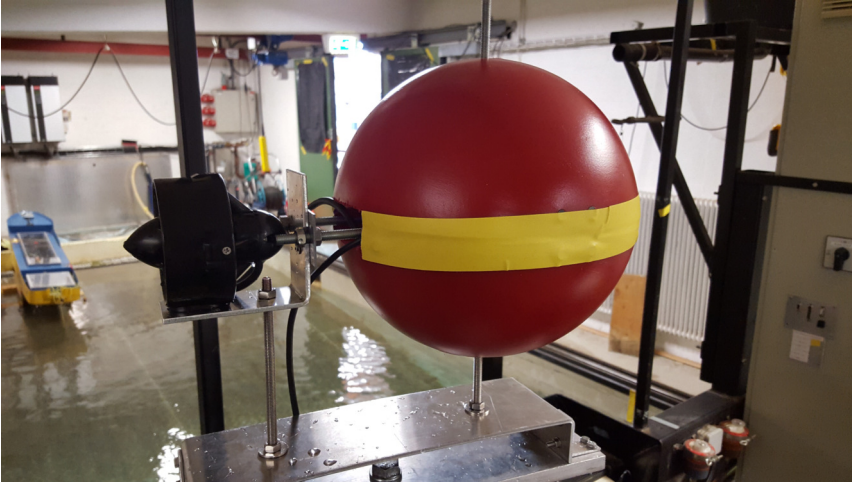
Figure 4.5: Subsystem with Ø25 shell mounted on bracket and ready for submerged thruster identification tests.

$$f_t = f_1 + f_2 + f_3. \tag{4.14}$$

The thrusters are controlled by a Raspberry Pi 3 from an air-sealed tube which also contains a battery, an ESC, and wired connectivity to the surface. The tube is fitted into the spherical hull as to not interfere with the smooth hull. The position of the umbilical cable ensures minimal interference on the hull. The Raspberry Pi 3 is controlled from the surface through the network using Robot-Operating-System (ROS) [182].

---

[2]T-200 performance chart: http://goo.gl/JXcQpy
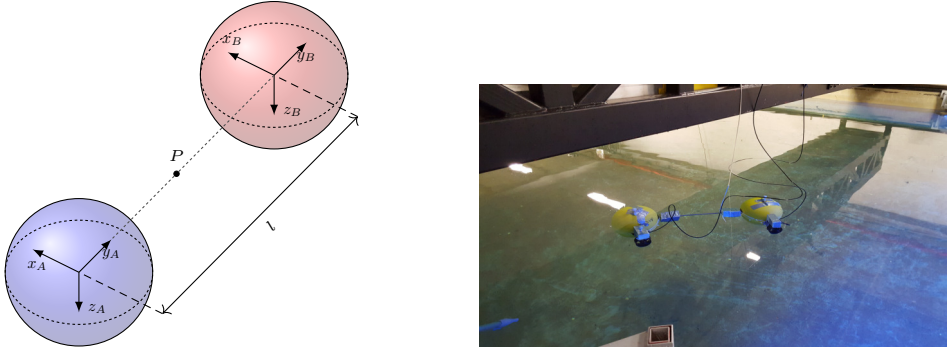
(a) Illustration of the experimental config-
uration of the open-loop maneuvering test.
The attitude of both vehicles are identical
such that axis y_A and y_B coincide.

(b) The open-loop maneuvering test imple-
mentation. The thrusters are mounted par-
allel to each other providing aft-actuation.

Figure 4.6: An overview of the experimental open-loop maneuvering configuration.
Fig. 4.6a illustrates the relative interconnection between the subsystems. Fig. 4.6b
shows the implemented system in the tank.

The experimental setup for the open-loop maneuvering experiment mirrors that
of the hydrostatic experiment, with the exception that the relative rotation between
the subsystems is zero. Fig. 4.6a shows the interconnection between the subsystems
in the open-loop maneuvering experiment. Ideally, the gravity vectors of each sub-
system are in agreement, such that, the subsystems would get passive stabilization
in pitch and roll. The Qualisys Motion capture system is utilized to track the
position of each individual subsystem.

4.4.1 Thruster Identification

The thruster parameters are identified using bollard pull tests. The bollard pull
tests are conducted by initializing the Data Acquisition (DAQ) with the thruster at
rest. The PWM signals, for the thrusters, are increased in a step-wise fashion such
that the thruster and the load cells reach a steady-state condition, before stepping
again. The thrusters exhibit a dead-zone around $1500\mu s$ of $25\mu s$. The PWM signal
sequence is started at $1525\mu s$ to overcome the dead-zone, then increased to $1540\mu s$,
and futher increased to $1700\mu s$ in $20\mu s$ increments. The experiement is conducted
for two sizes of modules producing two data sets. The signal values are kept active
for 30 seconds to ensure the steady-state conditions.

The rating of each load cell is 18 kg, and the sampling rate is 200 Hz. As the
load-cell measurement ratings are much larger than the magnitude of the force in
question the measurements have low resolution and high noise. The data is post-
processed by applying a 6th order Butterworth low-pass filter and a mean filter
with a windows size of 500 (2.5 seconds). The mean of each plateau defines a data
sample for the thruster characteristics. The result is shown in Fig. 4.7. The two
datasets share the same profile; this makes sense since the most significant inhibitor
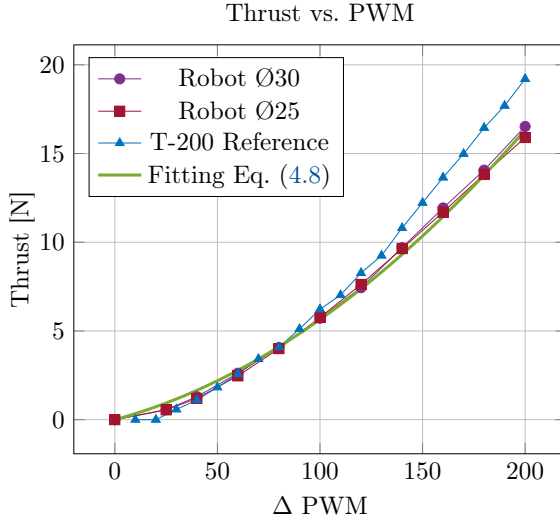
Figure 4.7: Thrust Characteristics for two sizes of robots and the PWM to thrust fitting.

of flow to the propeller is the thruster fitting, which is identical across the two subsystems. However, compared to the T-200 reference charts, there is a significant drop in force above $1600\mu s$, validating the hypothesis that the hull-interaction is significant. Tab. 4.4 shows the least-squares fitting of data from Fig. 4.7 onto the

Table 4.4: Result of least-square fitting on thrust data on Eq. (4.8).

K_L	K_Q	R^2
3.123×10^{-2}	2.52×10^{-4}	0.992

model of Eq. (4.8).

4.4.2 Results & Discussion

In the hydrodynamic experiments, a thruster is mounted on each vehicle to apply a force. The relative attitude between the subsystems is zero to isolate the motion induced by the thrusters to a single axis. Hence, the actuation is no longer zero $\boldsymbol{\tau}_i \neq \mathbf{0}$ for $i \in \{A, B\}$.

Two configurations are considered, first by using identical subsystem hulls the expected trajectory of the combined CG is a straight line. Secondly, reducing the size of subsystem B lowers the damping. The hypothesis generated from the numerical simulations of Chapter 3 proposed that the trajectory was expected to diverge towards the port side. Fig. 4.8 shows the result of a step on both thrusters. Qualitatively the trajectories are in agreement. However, the open-loop maneuvering test is subject to multiple confounding factors. First, the alignment between
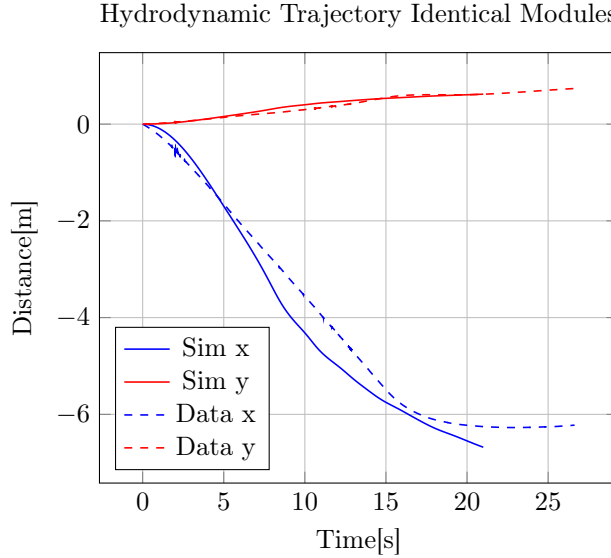
Figure 4.8: Hydrodynamic Trajectory of two identical modules.

the thruster and the respective body-fixed x-axis is imperfect. The consequence of the misalignment is that the thrusters do not exert force in the expected direction. Secondly, the thrusters are not attached at a point off of the y-axis of the CoM, hence the pitch angle is excited when the thrusters are engaged. The restoring force vector was assumed strong enough to overcome the excitation of the pitch moment. However, the experiments showed that this was not the case.

4.5 Chapter Summary

The chapter considered a preliminary model validation scheme. Two modules were identified, and subsequently combined using the simulator developed in Chapter 3. Two different experiments were conducted to investigate the model behavior; namely a hydrostatic experiment, and an open-loop maneuvering experiment. The restoring force vector actuated the modules in the hydrostatic experiment. The model parameters were derived through CFD and compared to the actual measured result. The findings showed that the hydrostatic oscillation period was very well determined by just considering decoupled module parameters, but the equilibrium angle was offset by $11°$ from the expected, and the CFD derived damping coefficient did not match those of the real system. Secondly, a dynamic parameter fitting was conducted to find both the restoring force vector and the resulting damping coefficients accordance with expectation. The identified restoring force vector component only changed a few millimeters. However, the result drastically changed the angular equilibrium of the system. Hence, the experiment was very sensitive to errors in the restoring force vector components.

The open-loop maneuvering experiment experience multiple confounding factors leading to poor quantitative outcomes. However, qualitatively the experimental trajectories were in agreement with the simulations. The open-loop maneuvering experiment concluded that that active control of pitch, roll, and heave is highly desirable to reduce confounders in future experiments.

Chapter 5

Identification of the BlueROV

The constrained multi-body dynamics method presented in Chapter 3 couples the dynamics of multiple sub-systems into an overall model that captures the main dynamics. Thereby, the sub-system models must be identified for the purpose of validating the overall modeling methodology. Given the purpose of the modeling scheme, the subsystem of choice was a BlueROV vehicle from Bluerobotics.

Contribution

The contribution of this chapter is an experimental investigation of the dynamic model parameters of the BlueROV vehicle. The experimental investigation involves towing tank tests conducted at MCLAB during January 2017. The chapter details, how the tests were prepared, executed and why certain simplification were made. Subsequent data analysis is discussed along with comparisons to the equivalent CFD results obtained in SolidWorks.

Organization of this chapter

The organization of the chapter is as follows: The models of the thruster and vehicle hull dynamics are presented and discussed in Section 5.2. Then, the experimental hardware setup within MCLAB is presented in Section 5.3. The resulting experimental data is analysed to obtain the dynamic parameters of the thruster and vehicle in Section 5.4. Finally, Section 5.5 summarises and compares the chapter main findings to the CFD results.

Publications

The material used in this chapter is based on the publication

[J1] Mikkel Cornelius Nielsen et al. "Constrained multi-body dynamics for modular underwater robots — Theory and experiments". In: *Ocean Engineering* 149.February 2018 (2018), pp. 358–372

5.1 Introduction

System identification of dynamic models is a widely studied problem in literature. The purpose of system identification is to obtain some knowledge of the system parameters based on a mapping between the input and output. However, model based system identification imposes a specific structure to the parameters. Often these parameters are results of first-principle modeling and thus have a physical meaning attached to them.

For underwater vehicles such parameters are - among others - the drag forces, the added mass and the hydrostatic lever arm. The kinetic coefficients of the underwater vehicle requires knowledge of the forces exerted on the vehicle along with the velocity at which it moves.

$$0 = \tau - c_1|u_a|u_a + c_2 u_a, \tag{5.1}$$
$$c_1, c_2 \in \mathbb{R}_{\geq 0}.$$

Eq. (5.1) shows the expression for a basic uncoupled DOF on a UUV. The problem of estimating c_1 and c_2 can be approached in two ways. Either the velocity u_a is applied and τ is measured or τ is applied and u_a is measured. In the case, where u_a is applied and τ is measured - the velocity-force approach - the τ represents the damping force of the system at the given velocity. Sampling at multiple different velocities allows for a curve-fitting of Eq. (5.1).

In cases, where τ is applied and u_a measured - the force-velocity approach - the τ is often a result of thruster actuation and thus the actuator model needs to be known prior to the experiments.

In either cases, the force τ must be measured or applied and both are approaches are difficult to implement on real systems. However, the force-velocity approach has garnered most research interest because of the potential to use on-board sensors to estimate the velocity and thus potentially allow cheaper identification procedures. Caccia, Indiveri, and Veruggio [32] considered a force-velocity approach, where the thrusters were identified by bollard pull tests and subsequently the dynamics of an Open-Frame ROV was derived based on the assumed force produced by the thrusters. Marco, Martins, and Healy [129] conducted identification on the surge part of an AUV using motion data from a sonar ranging devices to estimate the velocity and acceleration. The propeller shaft velocity was measured using a tachometer and the propeller to force model was assumed known prior from bollard pull tests. Similarly in Ridao et al. [188] the authors used a visual navigation system to obtain the velocity and accelerations based on a pose measurement. The method also used bollard pull tests to obtain a model for the thrusters.
The confounder in most force-velocity approaches is the assumption on the known relation between propeller and thrust.

A remedy to the thrust-velocity confounding is to use another force input with better known force profile. Ross, Fossen, and Johansen [190] proposed to replace the thrust input with a spring attachment with known spring coefficients in combination with a free-decay test. As opposed to thruster identification, the spring coefficients are easily identified and the proposed method showed promising results in simulation.

Inspired, in part, by Ross, Fossen, and Johansen [190], the authors Eng et al. [53] suggested to use a pendulum type free-decay and applied it to an ROV in a test tank. The position was captured by a camera system and the resulting damping and added mass coefficients were identified and compared to CFD results. The advantage of the method related to the ability to better restrict identification to single DOF, the fact that the applied force was equal to the gravity, and the high repeatability of the experiment.

The velocity-force approach to identification is often realised by towing-tank tests, where the vehicle is towed through a water tank or placed in a fixed position in a flume tank.

Towing tank testing is the industrial standard for obtaining dynamic parameters of ship models. Substantial research has been conducted to extend the towing tank principle to underwater vehicle identification. Avila and Adamowski [12] and Avila et al. [11] identified ROV damping coefficients using Morison's equation and a series of Planar-Motion-Mechanism (PMM) tests in a towing tank. As already mentioned, the velocity-force approach can also be conducted in a flume tank, where the water velocity is varied and the vehicle is fixed to a force measurement setup. Nouri, Mostafapour, and Bahadori [149] investigated such an approach, where they designed an apparatus to oscillate the vehicle in multiple directions.

5.2 Identification of Hull and Thrusters

During trials conducted in October 2016 it was observed that thruster dynamics had profound impact on the motion of the vehicles. It was hypothesised that the flow across the propeller reduced the produced force.

As a result, the dynamics of the vehicle was partitioned into two parts. The actuation system consisting of the thrusters attached to the ROV and the ROV itself. Fig. 5.1 shows the partitioning, where the body-velocity $\boldsymbol{\nu}$ is fed back to the
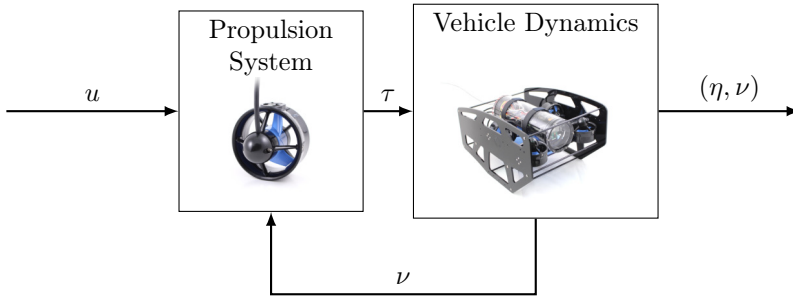
Figure 5.1: Model subsystem segregation of simulation model for single vehicle system. Signal u represents the control input PWM and τ is the produced forces.

thrusters.

5.2.1 BlueROV Hull

The hydrodynamic drag forces are a result of multiple factors. However, according to Fossen [61], the main forces are derived from: *Potential Damping*, *Skin Friction*, *Wave Drift Damping*, *Damping Due to Vortex Shedding* and *Lifting Forces*. Underwater vehicles are assumed to be moving far enough under the surface of the water, such that the waves do not affect their motion. Thus, the *Potential Damping* and *Wave Drift Damping* are not considered and the frequency dependency of the *Skin Friction* is also neglected. In short the damping forces can be assumed to comprise of linear and quadratic drag terms in the body-fixed velocity vector $\boldsymbol{\nu}$.

$$\boldsymbol{D}\left(\boldsymbol{\nu}\right) = \boldsymbol{D} + \boldsymbol{D}_n\left(\boldsymbol{\nu}\right). \tag{5.2}$$

Althought, the matrices $\boldsymbol{D}$ and $\boldsymbol{D}_n$ are not necessarily diagonal, they are assumed as such, since obtaining the off-diagonal elements in an experimental setting is very difficult and time consuming. The experiments are specifically designed for identification of uncoupled parameters. The hydrodynamic damping $\boldsymbol{D}(\boldsymbol{\nu})$ is a product of multiple components as discussed in [52] and [61]. The effects of the different components can be collected into a linear an quadratic term, such that,

$$f_D\left(u_a\right) = c_1|u_a|u_a + c_2 u_a, \tag{5.3}$$
$$c_1, c_2 \in \mathbb{R}_{\geq 0},$$

where c_1 and c_2 constitute the damping parameters. Another important effect is the Added Mass effect. During acceleration and deceleration the vehicle must push more water adding to its own mass (and thus added mass is an important factor to consider). Unfortunately, due to the nature of the effect, obtaining added mass coefficients requires tight control of the acceleration of the vehicle. Instead of experimentally identifying the added mass parameters, the effects were obtained through CFD simulation.

5.2.2 Thruster & Propeller

The actuation input for the vehicle $\boldsymbol{\tau}$ is a result of the combination of thrusters mounted on the vehicle. Thrusters are located on the vehicle relative to the centre of origin (CO). Each thruster contains a local frame aligned with the direction of thrust produced. The thrust exerted in the body-frame of the vehicle is then calculated by transforming the thrust from the thruster-frame to the body-frame. Since the local x-axis is parallel with the produced thrust direction any rotation around said x-axis will not change the thrust generated in the vehicles body-frame. Instead the transformation from the local thruster to the body frame can be written as follows,

$$\begin{aligned}\boldsymbol{\tau}_{j/b}^b &= \boldsymbol{t}_j^b \tau_j, \\ &= \begin{bmatrix} \cos(\alpha_j)\cos(\beta_j) \\ -\cos(\alpha_j)\sin(\beta_j) \\ \sin(\alpha_j) \end{bmatrix} \tau_j, \end{aligned} \tag{5.4}$$

where subscript j denotes the jth thruster such that α_j and β_j are angles relating the direction of thruster j with respect to the body-fixed frame of the vehicle. The actuation $\boldsymbol{\tau}$ is the result of the combined thrust from each thruster, such that,

$$\boldsymbol{\tau} = \sum_{j \in \mathcal{J}} \boldsymbol{h}\left(\boldsymbol{\tau}^b_{j/b}, \boldsymbol{p}^b_{j/b}\right) = \sum_{j \in \mathcal{J}} \begin{bmatrix} \boldsymbol{\tau}^b_{j/b} \\ \boldsymbol{p}^b_{j/b} \times \boldsymbol{\tau}^b_{j/b} \end{bmatrix}, \tag{5.5}$$

where $\mathcal{J}$ is the set of thrusters mounted on the robot and $\boldsymbol{p}^b_{j/b}$ is the body-fixed position of thruster j. The force generated by the thruster τ_j depends on the motor driving the propeller and the propeller itself. Commonly, propellers are modeled in

Table 5.1: Nomenclature for thruster dynamics

Symbol	Name	Unit
u_a	Advance Speed	$\left(\frac{m}{s}\right)$
ω	Propeller shaft speed	$\left(\frac{rad}{s}\right)$
J	Advance Ratio	$(-)$
K_T	Thrust Coefficient	$(-)$
ρ	Water Density	$\left(\frac{kg}{m^3}\right)$
D	Propeller Diameter	(m)
$T_{|\omega|\omega}$	Thrust Coefficient	(kgm)
$T_{|\omega|u}$	Thrust Coefficient	(kg)
τ_p	Propeller Thrust	(N)

non-dimensional form and, as such, they can be described by the non-dimensional coefficient K_T defined as follows,

$$K_T = \tau_p \frac{4\pi^2}{\rho|\omega|\,\omega D^4}, \tag{5.6}$$

where τ_p is the thrust output of the propeller, ρ is the density of the water, ω is the propeller shaft angular velocity and D is the propeller diameter. Since the inflow velocity of the propeller affects the thrust output, K_T is a function of the advance ratio J defined as,

$$J = \frac{2\pi u_a}{\omega D}, \tag{5.7}$$

where u_a is the inflow velocity of the propeller. From Eq. (5.6) it is clear that the advance ratio does not enter the definition directly. Blanke, Lindegaard, and Fossen [23] showed that linear lift theory for propeller blades lead to the thrust expression,

$$\tau_p = T_{|\omega|\omega}|\omega|\omega + T_{|\omega|u}|\omega|u_a, \tag{5.8}$$
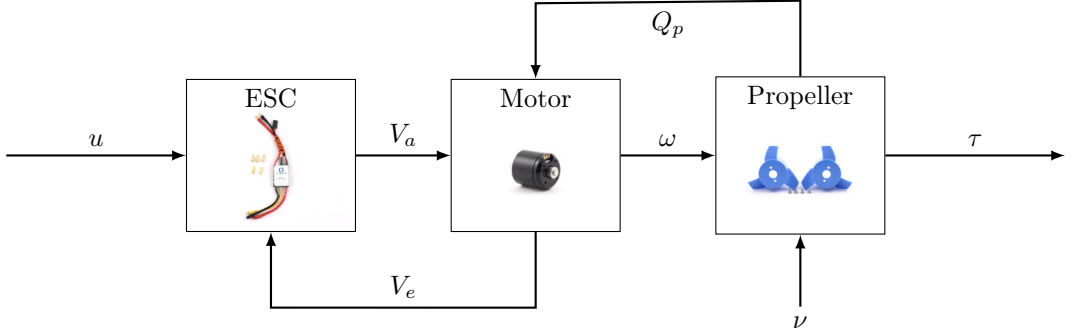
Figure 5.2: Diagram of thruster from input u to output τ. Signal u is the set-point for the ESC, which produces the control sequence V_a for the motor. The motor is affected by the load from the propeller Q_p and produces back-EMF, which affects itself and is measured by the ESC. The propeller is actuated by the shaft at velocity ω and disturbed by the resistance of the water, which depends on the velocity of the vehicle.

which in turn is equivalent to the approximation,

$$K_T = \alpha_0 + \alpha_1 J. \tag{5.9}$$

Access to the rotational velocity of the propeller is not always available, and hence a function to predict the rotational velocity based on an input u, e.g., PWM is necessary, such that,

$$\omega = f\left(u\right), \tag{5.10}$$

where $f\left(u\right)$ is a function of the input u to be defined later. Combining Eq. (5.6), (5.7) and (5.9) and solving for the propeller thruster yields an expression for the propeller induced torque,

$$Q_p = Q_{|\omega|\omega}|\omega|\omega - Q_{\omega u}\omega u_p. \tag{5.11}$$

Recalling that the motor constants k_i and k_t are related by,

$$k_i k_t = 1, \tag{5.12}$$

a simplified DC motor model from Fig. 5.2 is used to model the dynamics of the thruster:

$$J_m\dot{\omega} = \left(\frac{V - \omega k_t}{R}\right) k_q - k_{f_1}\omega - Q_{|\omega|\omega}|\omega|\omega. \tag{5.13}$$

The model is not accurate in the sense that the Brushless DC motor is controlled by a 3-phase signal from the ESC, thus V_a is not a DC voltage. However, for the purpose of this thesis the model is accurate enough.

5.3   Experimental Verification

Model testing based on towing tank experiments is a standardized approach to carry out hydrodynamic tests. The NTNU facilitates towing tank tests at the MCLAB. Thereby all experiments conducted to obtain the hydrodynamic parameters and thruster coefficients for the BlueROV are based on Towing Tank data. The International Towing Tank Conference (ITTC) association provides a variety of procedures to test different aspects of ship models in Towing Tank tests. Among these procedures are the resistance drag tests on ship models [85]. However, the procedure of measuring resistance drag of an underwater vehicle and the thruster coefficients is not standardized. Therefore, modifications were made to allow for underwater vehicles to be identified as well [52].

The experiment was partitioned into three stages

Step 1. Identify Mounting Bracket Drag

Step 2. Identify Unactuated BlueROV Hull Drag

Step 3. Identify BlueROV actuators forces

Since the thrusters are mounted inside the vehicle chassis and the chassis itself is mounted on the bracket the effect of each of these must be identified. The sensors can only measure the total force applied to the bracket and, therefore, the identification of thruster parameters is separated from that of the hull coefficients. The hull resistance is evaluated by first dragging the vehicle through water at different velocities to measure the force and then by conducting a polynomial fitting to measurements. The thruster performance is evaluated by dragging the vehicle through water at different velocities and for different commanded thruster inputs. The mounting bracket itself produces drag forces that need compensation in the data, thus the first step of the experimental verification was to identify the bracket drag profile. Once the bracket drag forces were known, the hull of the BlueROV itself could be estimated by towing it through the tank at different velocities. Finally, to identify the effects of flow across the propellers, the BlueROV was towed at different velocities, while the thrusters were engaged with different PWM commands.

5.3.1   Mounting Bracket

The towing carriage in MCLAB features a velocity controller for the bridge itself. Thereby mounting the vehicle on the bridge allows for tight control of the velocity at which the vehicle is dragged through the water. The bracket was designed by Ole A. Eidsvik for experiments conducted on the Neptunus ROV and presented in Eidsvik and Schjølberg [52]. The bracket consists of two 1-DOF force blocks installed between the bridge and the bracket itself.
 Fig. 5.3 shows the force block configuration between the bracket and bridge.
It was observed, during the experiments on the Neptunus ROV, that the bracket had a tendency to bend, which would add uncertainty in the measurements. To compensate for this the bracket was modified to have a strain gauge attached on a cord between the front of the BlueROV and the forward part of bridge.
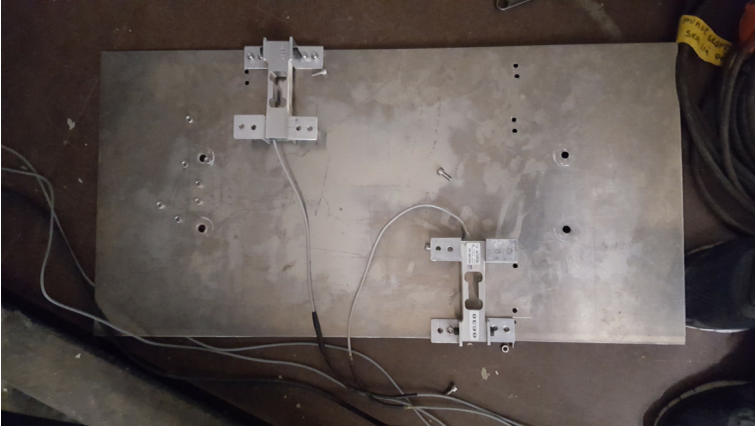
Figure 5.3: Force blocks m_1 and m_2 between the PMM and bracket.
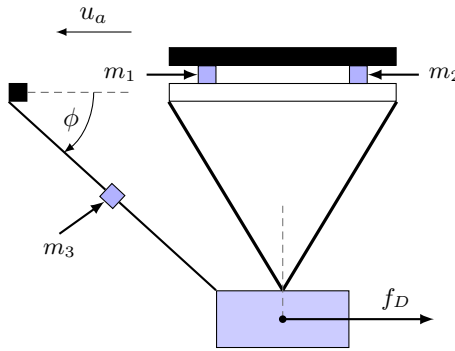
Figure 5.4: Diagram of the towing tank test setup with two load cells m_1 and m_2 attached between the towing carriage and bracket and a strain gauge m_3 attached though wire at an angle ϕ. The forward velocity u_a of the towing carriage and the induced drag force f_D are also shown.

Fig. 5.4 shows a diagram of the bracket mounted to the carriage bridge. The force blocks m_1 and m_2 are attached between the bracket and the carriage bridge. The strain gauge m_3 was attached at an angle ϕ, which was measured during the experiments. The velocity enforced by the carriage bridge actuation system u_a induces a drag force f_D on the vehicle. Fig. 5.5a shows the BlueROV mounted on the bracket, and Fig. 5.5b shows the submerged bracket mounted with the BlueROV under the towing carriage. The mounting bracket with the ROV was fastened to the PMM on the carriage in MCLAB. Load cell m_3 is mounted at an angle ϕ hence the measured force includes a component not related to the motion of the vehicle. The total force acting on the bracket and vehicle is a function of all
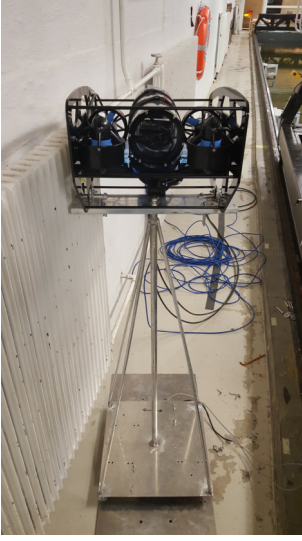
(a) BlueROV vehicle attached to the measurement bracket. The bracket is standing up side down on the side of the tank.
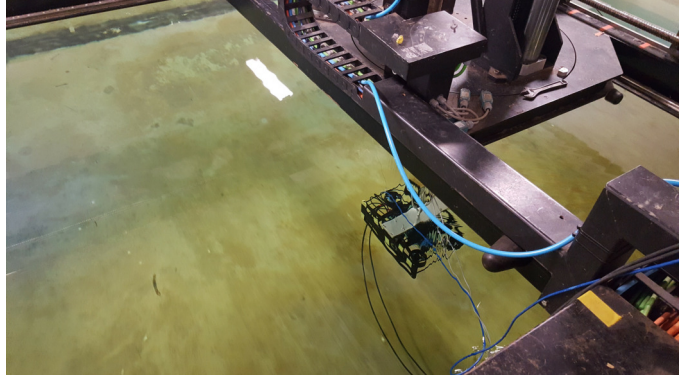
(b) Vehicle attached to bracket and mounted submerged underneath the towing carriage

Figure 5.5: The bracket with the vehicle attached mounted on the PMM in MCLAB

three measurements given in Eq. (5.14).

$$f_D = f_{m_1} + f_{m_2} - f_{m_3} \cos(\phi).$$ (5.14)

The masses m_1 and m_2 correspond to two 18 kg load cells of the type PW2GC3 from Hottinger Baldwin Messtechnik GmbH (HBM)[1], while m_3 was a 5 kg strain gauge.

5.3.2 Thrust Control and Power

The measurements of the propeller RPMs are usually conducted using a tachometer attached to the shaft of the motor. However, due to the design of the T-200 thrusters, there is no support for such a sensor attachment and as a result the shaft speed ω must be estimated based on the back-EMF voltage of the motor itself. The ESCs employed to drive the motors are 3-phase drives. At each time only two of the coils in the motor are energized leaving the last coil to measure the back emf,

$$RPS_{ESC} = \frac{RPS_{raw}}{0.5 N_{poles} \Delta t},$$ (5.15)

[1][1]

where RPS_{raw} is the cumulative zero-crossings of the motor poles across the non-energized coil, Δt is the time between pooling of the ESC and N_{poles} are the number of poles in the motor. The M-200 motor contains 14 poles.

The ESC used in the BlueROV is connected to the PixHawk through PWM signaling, however, in order to query the ESC for the RPS_{raw} signal the firmware of the ESC had to be changed. The changed firmware effectively changed the interface from PWM to Inter-Integrated Circuit (I^{2}C). Unfortunately, the interface change meant that the PWM interface was blocked, thus leaving the PixHawk interface unusable. The solution was to implement an Arduino Mega 2550 into the BlueROV to bypass the PixHawk and interface directly with the I^{2}C interfaces of the ESCs.

Finally, the ROV had to fastened from below the carriage. Since the BlueROV is battery powered, it was necessary to establish an external power supply system to power the BlueROV from the towing carriage.

5.3.3   System Implementation

The BlueROV is interfaced by ROS, whereas the Towing Carriage control system is implemented on a stationary desktop on the bridge itself.

The mounting bracket is fitted to the carriage wagon and the setup was dragged from one end of the pool to the other multiple times a different velocities. The important factor is that the carriage reaches steady state speed and that the speed and force measurements are accurately timed and logged. Fig. 5.6 shows the signal communication setup in MCLAB. The ROS computer was connected over the network to the BlueROV sending PWM signals and receiving the RPM measurements. The carriage computer was connected to the DAQ device, which interfaced the three force measurement sensors attached to the bracket and to the towing carriage control system for set-point regulation of u_a.

The static drag tests only required data from the carriage bridge computer. Thereby the identification of the bracket and BlueROV hull drag could be conducted without consideration to the synchronization between thruster data on the ROS computer and force and velocity measurements on the carriage bridge computer. The thruster tests, however, required data from both computers. For technical reasons it was not possible to setup network synchronization between the computers. Fortunately, the tests were conducted under steady state motion of the towing carriage and the dynamics of the thrusters are many times higher than the dynamics of the carriage wagon. Thereby, the steady state segment of the data was easily identified for subsequent analysis.

5.4   Analysis of Data

The bracket was identified during the tests in [52] yielding an expression for the bracket drag parameterized in the velocity:

$$f_B\left(u_a\right) = 25.06|u_a|u_a + 4u_a, \tag{5.16}$$

Each run produced a time-series measurement data-set X, from which a subset $\bar{X} \subset X$ contains a stationary part. The load cells and strain gauge are low cost
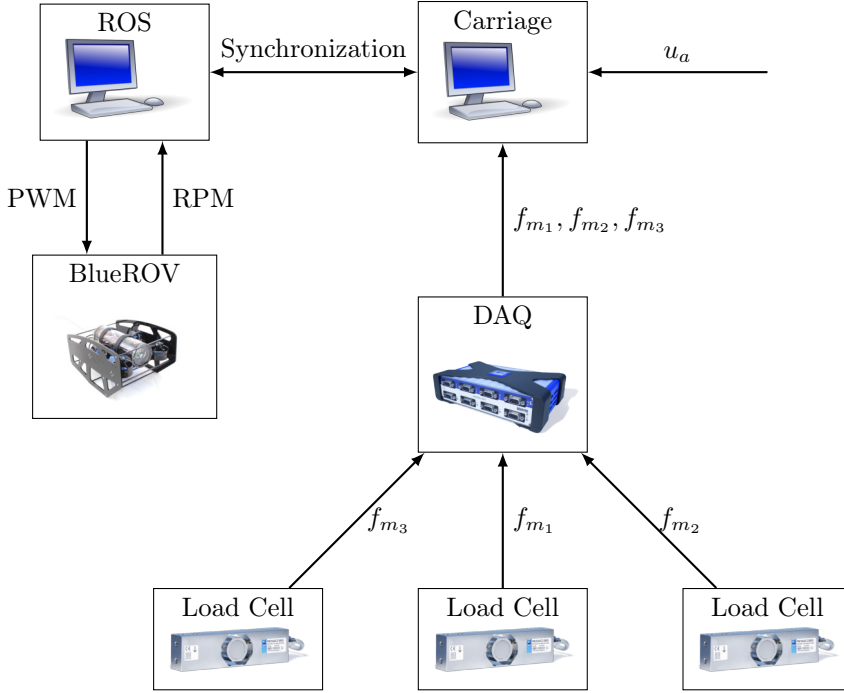
Figure 5.6: Diagram of connections between carriage computer, ROS computer and the load cells in MCLAB

devices and the signals are affected by significant amount of noise. To mitigate the effect of the noise, each stationary subset was reduced to a statistic pair composed of the expected value μ_x and the variance $P_x = \sigma_x^2$.

Fig. 5.7 shows an example of a time-series obtained from the surge drag estimation runs at $0.5\frac{m}{s}$ forward velocity. The left graph shows the whole data-set X with the stationary subset $\bar{X}$, and the right graph shows only the stationary part. The histogram shows the distribution of the signal segment with a fitted normal distribution $\mathcal{N}(\mu_x, \sigma_x^2)$ for comparison. Multiple runs were conducted at each velocity to increase the statistical certainty.

The statistics of the runs were then fused using a Weighted-Least-Squares (WLS) type algorithm to produce one point $\hat{x}$ for each velocity and an associated uncertainty P_x as shown below

$$P_x = \left(P_1^{-1} + \cdots + P_n^{-1} \right)^{-1}, \tag{5.17}$$

$$\hat{x} = P_x \left(P_1^{-1}\mu_1 + \cdots + P_n^{-1}\mu_n \right). \tag{5.18}$$
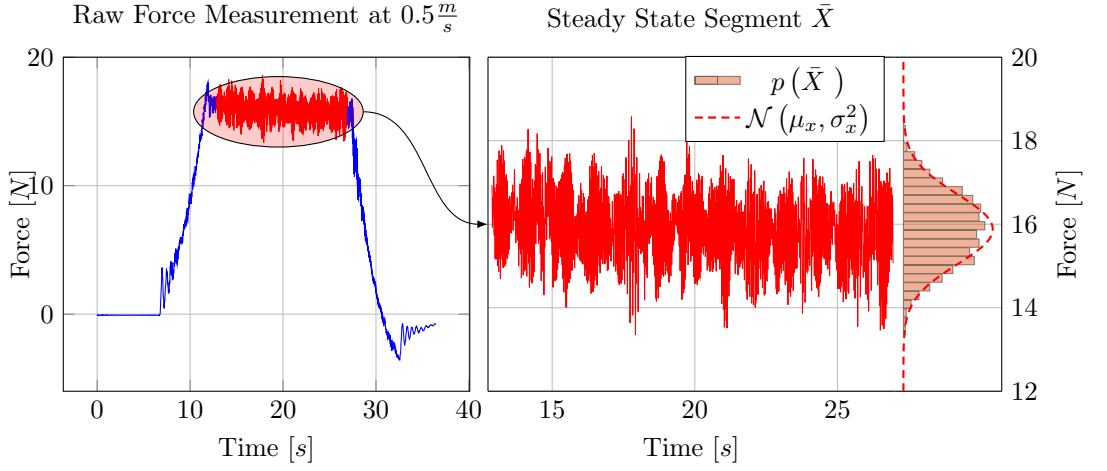
Figure 5.7: The steady state segment of each time series is extracted and reduced to a mean μ_x and a variance σ_x^2. The distribution of the signal around the steady state mean μ_x approximately follows a normal distribution.
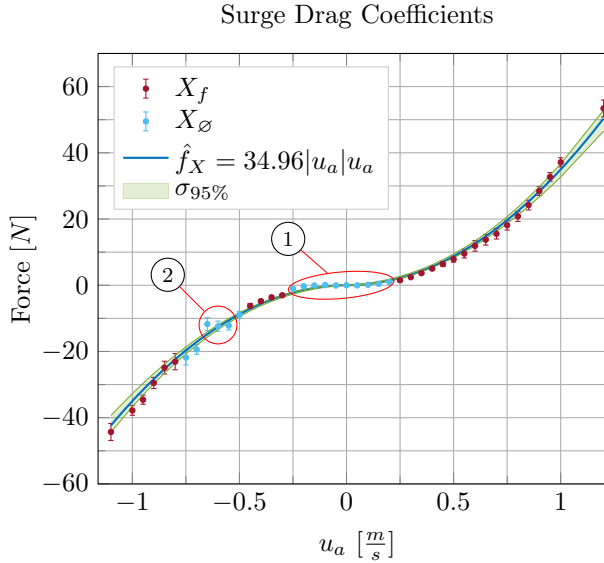
Figure 5.8: Surge drag coefficient estimates for the single vehicle case with the fitting data X_f and excluded data $X_\varnothing$ along with the fitted curve and the associated 95% confidence interval.
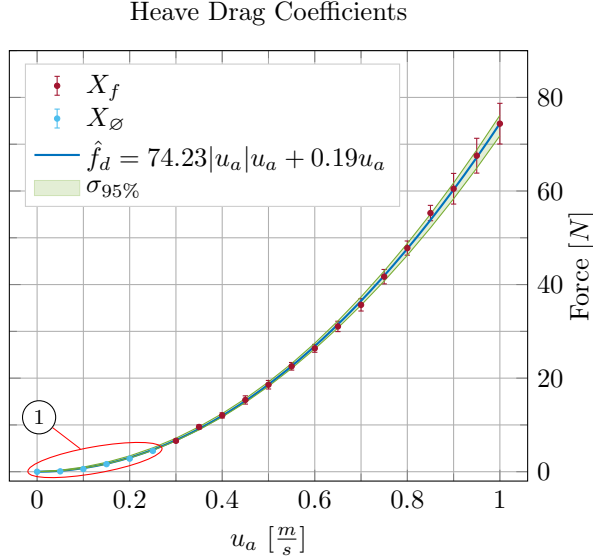
Figure 5.9: Heave drag coefficient estimates for the single vehicle case with the processed data X_f, the fitted curve $\hat{f}_X$ and the 95% confidence interval. It is noted, however, that the disregarded points fit well with the polynomial estimate.

5.4.1 Translational Drag

The surge drag experiments consisted of 128 datasets with divided across 42 different velocities (21 forward and 21 backwards). Using Eq. (5.17) and (5.18) the 128 datasets were reduced to 41 data points. The 42 data points were partitioned into fitting data X_f and non-fitting data $X_\varnothing$. The data partitioning was motivated by observed anomalies in the data (marked with ② on Fig. 5.8). Moreover, due to the low sensitivity of the load cells at small amplitudes, a significant amount of the data was excluded from the fitting marked by ①. The resulting data points of the fitting set X_f were used to fit Eq. (5.3) using bounded non-linear least squares.

Fig. 5.8 shows the resulting fitting along with confidence bounds.

The heave drag experiments were only performed in upwards direction and consisted of 61 datasets across 20 different velocities. As was the case with the surge drag, the points were reduced using the fusion formulas and divided into fitting data X_f and excluded data $X_\varnothing$. The resulting fitting is shown on Fig. 5.9.

5.4.2 Rotational Drag

The rotational drag consisted of 25 datasets captured across 7 different velocities. The distribution of the noise was subjected to additional dynamics, which violated the assumption of normal distributed noise. As a result, the fusion formulas could not be used and instead, the fitting points were picked by hand. Fig. 5.10 shows
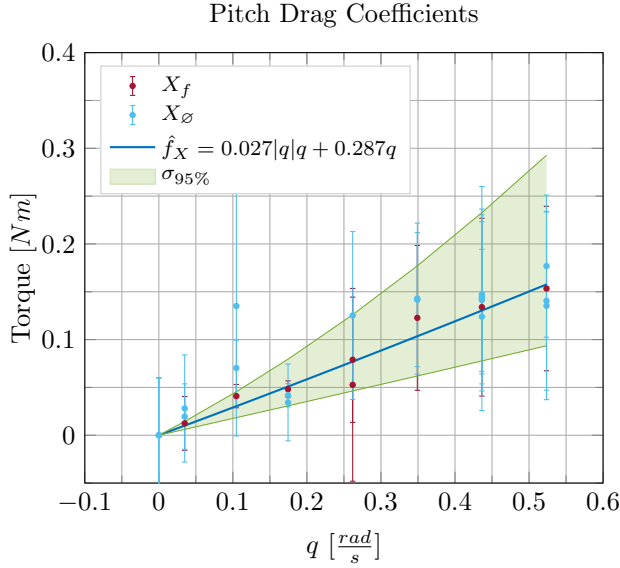
Figure 5.10: Pitch drag coefficient estimates for the BlueROV with the fitting data X_f and excluded data $X_\varnothing$ along with the fitted curve $\hat{f}_X$ and the associated 95% confidence interval. The fitting is dominated by the linear term, which is expected [32].

that for small velocities the quadratic term in the drag torque vanishes. This is in accordance to the results presented in [32].

5.4.3 Thruster Reduction

The thruster experiments were conducted by dragging the vehicle through the tank with the thrusters engaged at different PWM levels. The towing tests were conducted at $0.1ms^{-1}$, $0.2ms^{-1}$, $0.3ms^{-1}$, $0.5ms^{-1}$, $0.7ms^{-1}$, $0.8ms^{-1}$ and $0.9ms^{-1}$.

The flow conditions on the thrusters changes as a function of the velocity through the water. Thereby, the thrust generated by the thrusters reduces as a function of the velocity of the water across the propellers.
The water flow across the propeller is a function of both the body-fixed velocities and the water currents. In MCLAB there are no water currents, and therefore only the body-fixed velocities were considered.

Fig. 5.11 shows two RPM time-series data sequences of ten seconds each at different towing velocities. Although there is some variation in the RPMs at each PWM instance, it is not correlated with the velocity through the water, which suggests that the propeller load change was properly suppressed by the ESC. Instead, the PWM to RPM relationship is assumed static. The rotational rate was related to the PWM input through a fractional exponent relationship and the fitting is

Steady State RPM under different flow conditions
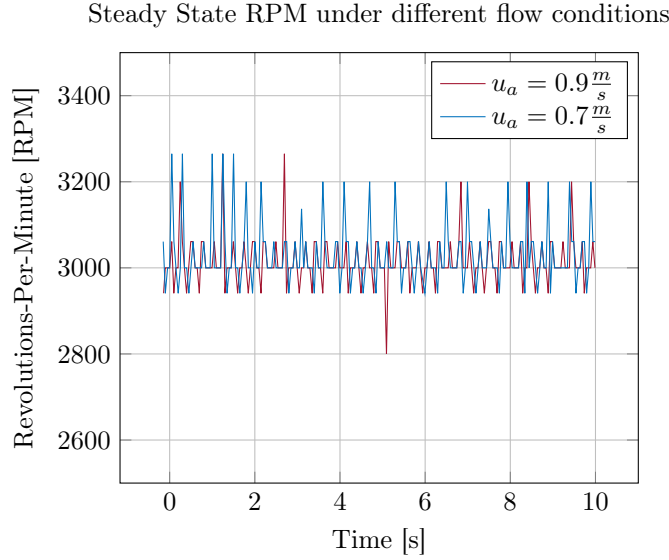
Figure 5.11: Two cropped data series of propeller RPM at forward velocity $0.9\frac{m}{s}$ and $0.7\frac{m}{s}$ respectively. There is no significant change between the RPMs suggesting that the ESC manages to maintain the shaft velocity at different flow velocities.

shown in Fig. 5.12.

$$f(x) = ax^{-b} + c \qquad (5.19)$$

The forces, measured under the experiments, were compensated by the bracket and vehicle drag and, in turn, the the thrust coefficient K_T from Eq. (5.6) was calculated. Fig. 5.13 shows the calculated thrust coefficients K_T from Eq. (5.6) and the linear estimate $\hat{K}_T$ from Eq. (5.9). Based on the thrust coefficient fitting shown in Fig. 5.13 the produced thrust of the propeller is reduced as velocity of the water across the propeller increases. This behavior is consistent with the literature [23].

Evaluating the thrust loss of each PWM and at each velocity profile yields a map of thrust loss as shown in Fig. 5.14. Three inconsistencies are marked in the thrust loss map. The mark ① shows at $1740\mu s/0.7\frac{m}{s}$ shows an increased propulsion relative to the surrounding points. The same holds true for mark ② at $1820\mu s/0.8\frac{m}{s}$ and subsequently all PWMs at $0.9\frac{m}{s}$ is either equal or increasing compared to at $0.8\frac{m}{s}$. It should be noted that the confidence intervals increase with the velocity. For velocities under $0.5\frac{m}{s}$ the thrust is consistently reduced across the operating range of the thruster. The overall result of the thruster mapping, however, is that the model of Eq. (5.8) is necessary to avoid overestimation of the produced thrust under motion.
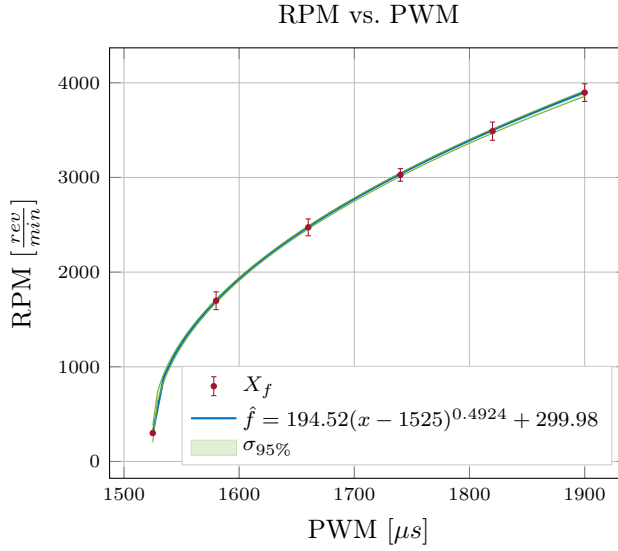
Figure 5.12: The RPM measurements are shown in X_f with 95% confidence bounds, the PWM to RPM fitting $\hat{f}$ is shown along with the 95% confidence interval. The estimated fitting intersects all the measurement points and the confidence of the parameters allows for a tight confidence interval.
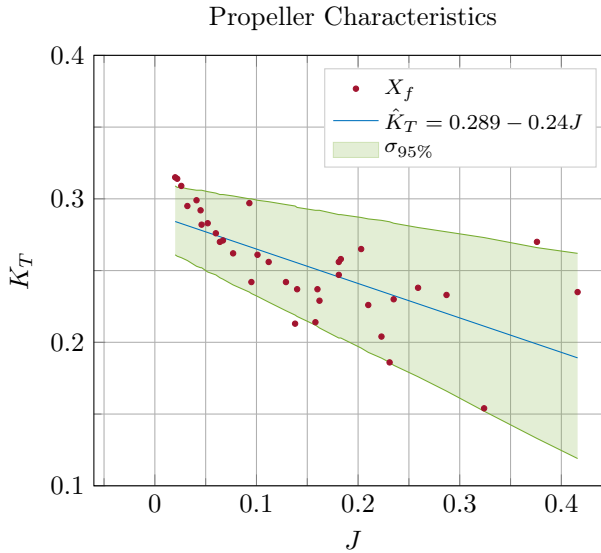
Figure 5.13: Dimensionless propeller characteristics data X_f and the linear estimate $\hat{K}_T$ versus the advance speed J
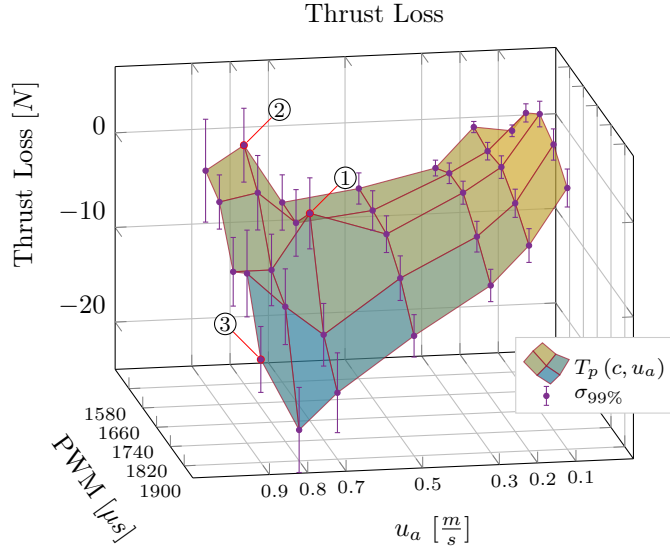
Figure 5.14: Thrust loss as function of PWM and forward velocity u_a with 99% confidence intervals at each point.

5.4.4 Result Summary

Three DOFs, surge, heave and pitch, were identified using towing tanks tests. The remaining three DOFs, sway, roll and yaw, were not identified experimentally, but were extrapolated using ratios between the added mass coefficients as follows

$$K_{|p|p} = \left(\frac{K_{\dot{p}}}{M_{\dot{q}}}\right) M_{|q|q} \ , \ K_p = \left(\frac{K_{\dot{p}}}{M_{\dot{q}}}\right) M_q,$$

$$N_{|r|r} = \left(\frac{N_{\dot{r}}}{M_{\dot{q}}}\right) M_{|q|q} \ , \ N_r = \left(\frac{N_{\dot{r}}}{M_{\dot{q}}}\right) M_q,$$

$$Y_{|v|v} = \left(\frac{Y_{\dot{v}}}{Z_{\dot{w}}}\right) Z_{|w|w} \ , \ Y_v = \left(\frac{Y_{\dot{v}}}{Z_{\dot{w}}}\right) Z_w.$$

Applying the equations to the experimentally acquired parameters yields estimates of the missing parameters. Table 5.2 shows an overview of the final values used in the subsequent simulations. Comparing Table 5.2 with the coefficients generated from a CFD study in SolidWorks, shown in Table 5.3, reveals significant discrepancies between the obtained values. The discrepancies in the rotational drag coefficients are not surprising since CFD estimation for rotational degrees of freedoms is difficult.

5.4.5 Extended Simulator

This chapter increased the model fidelity of the subsystem models used in the modeling methodology of Chapter 3. The simulator from Section 3.5 assumed that

Table 5.2: Estimated dimensional hydrodynamic parameters for the BlueROV vehicle

$X_{\dot{u}}$ $[kg]$	2.6	$X_{\|u\|u}$ $[\frac{kg}{m}]$	34.96	X_u $[\frac{kg}{s}]$	0
$Y_{\dot{v}}$ $[kg]$	18.5	$Y_{\|v\|v}$ $[\frac{kg}{m}]$	103.25	Y_v $[\frac{kg}{s}]$	0.26
$Z_{\dot{w}}$ $[kg]$	13.3	$Z_{\|w\|w}$ $[\frac{kg}{m}]$	74.23	Z_w $[\frac{kg}{s}]$	0.19
$K_{\dot{p}}$ $[kgm]$	0.054	$K_{\|p\|p}$ $[kgm]$	0.084	K_p $[\frac{kgm}{s}]$	0.895
$M_{\dot{q}}$ $[kgm]$	0.0173	$M_{\|q\|q}$ $[kgm]$	0.028	M_q $[\frac{kgm}{s}]$	0.287
$N_{\dot{r}}$ $[kgm]$	0.28	$N_{\|r\|r}$ $[kgm]$	0.43	N_r $[\frac{kgm}{s}]$	4.64

Table 5.3: Estimated hydrodynamic parameters based on CFD in SolidWorks.

$X_{\|u\|u}$ $[\frac{kg}{m}]$	16.41	X_u $[\frac{kg}{s}]$	2.63
$Y_{\|v\|v}$ $[\frac{kg}{m}]$	46.49	Y_v $[\frac{kg}{s}]$	7.43
$Z_{\|w\|w}$ $[\frac{kg}{m}]$	37.63	Z_w $[\frac{kg}{s}]$	6.02
$K_{\|p\|p}$ $[kgm]$	0.164	K_p $[\frac{kgm}{s}]$	0.014
$M_{\|q\|q}$ $[kgm]$	0.087	M_q $[\frac{kgm}{s}]$	0.012
$N_{\|r\|r}$ $[kgm]$	0.97	N_r $[\frac{kgm}{s}]$	0.08

the thruster mapping between input $\boldsymbol{u}$ and thrust output $\boldsymbol{\tau}$ was static. In this chapter, the model $\mathcal{H}_i$ of Eq. (3.70) is extended with the new thruster dynamics.

A simulator is needed to evaluate and compare the behavior of the multi-body system. The vectors containing all the states of the system is defined as follows

$$\dot{\boldsymbol{\nu}}_u = [\dot{\boldsymbol{\nu}}_u^{(1)}, \ldots, \dot{\boldsymbol{\nu}}_u^{(i)}], \quad \dot{\boldsymbol{\nu}}_c = [\dot{\boldsymbol{\nu}}_c^{(1)}, \ldots, \dot{\boldsymbol{\nu}}_c^{(i)}],$$
$$\boldsymbol{\nu}_c = [\boldsymbol{\nu}_c^{(1)}, \ldots, \boldsymbol{\nu}_c^{(i)}], \quad \dot{\boldsymbol{\eta}}_c = [\dot{\boldsymbol{\eta}}_c^{(1)}, \ldots, \dot{\boldsymbol{\eta}}_c^{(i)}],$$
$$\boldsymbol{u} = [\boldsymbol{u}^{(1)}, \ldots, \boldsymbol{u}^{(i)}],$$

where $\boldsymbol{u}^{(i)}$ is the input vector containing the PWM signals for vehicle i. The vehicle subsystems are build from the dynamic model of Eq. (2.20), along with the propeller thrust model in Eq. (5.5), (5.4), (5.8) and (5.10). The new subsystems $\mathcal{H}_i$ are then defined as follows

$$\mathcal{H}_i \ : \begin{cases} \omega_j^{(i)} = f_j^{(i)}(u_j^{(i)}) & \text{Eq. (5.10)} \\ \tau_j^{(i)} = T_{\|\omega\|\omega}|\omega_j^{(i)}|\omega_j^{(i)} + T_{\|\omega\|u}|\omega_j^{(i)}|u_a^{(i)} & \text{Eq. (5.8)} \\ \boldsymbol{\tau}_{j/i}^i = \boldsymbol{t}_j^i \tau_j^{(i)} & \text{Eq. (5.4)} \\ \boldsymbol{\tau}^{(i)} = \sum_{j \in \mathcal{J}_i} \boldsymbol{h}\left(\boldsymbol{\tau}_{j/i}^i, \boldsymbol{p}_{j/i}^i\right) & \text{Eq. (5.5)} \\ \boldsymbol{M}^{(i)}\dot{\boldsymbol{\nu}}_u^{(i)} + \boldsymbol{D}^{(i)}(\boldsymbol{\nu}_c^{(i)})\boldsymbol{\nu}_c^{(i)} + \boldsymbol{C}^{(i)}(\boldsymbol{\nu}_c^{(i)})\boldsymbol{\nu}_c^{(i)} + \boldsymbol{g}^{(i)}(\boldsymbol{\eta}_c^{(i)}) = \boldsymbol{\tau}^{(i)} & \text{Eq. (2.20)} \end{cases}$$
$$(5.20)$$

5.5   Chapter Summary

Experimental identification was performed on both the BlueROV vehicle and the thruster system to obtain a complete dynamic model of the system. The hull parameters were identified via towing tank tests. Thruster tests were carried out in the form of towing tank tests so as to identify the loss of thrust as a function of the flow of the water across the propeller. The resulting model parameters were compared to those obtained through CFD analysis.

Chapter 6

Modeling for modular underwater robots

The constrained multi-body dynamics method presented in Chapter 3 couples the dynamics of multiple sub-systems into an overall model, that captures the main dynamics. The purpose of the constrained model is to give insight into the behavior of a system of small interconnected ROVs or AUVs. The vision for the modular underwater robotic system is, to utilize multiple small interconnected ROVs or AUVs for IMR task. The envisioned size of the vehicles is comparable with that of the BlueROV from BlueRobotics.

Contribution

The contribution of this chapter is the experimental validation of the modeling method presented in Chapter 3 and extended in Chapter 5.

The experimental validation is a free-motion experiment based on data from tests conducted at MCLAB in October 2016. Motion trajectory data is obtained through position measurements of the system while applying and logging different open-loop excitation signals to the thrusters of the vehicles. The simulator, developed in Chapter 3 and extended in Chapter 5, use the logged PWM signals to simulate trajectories of the system. The similarity between the time-series data from the simulator and the measured data from MCLAB is compared using Dynamic Time Warping (DTW) as a similarity measure.

Organization of this chapter

The organization of the chapter is as follows: Section 6.1 introduces the problem and explains the similarity measure. Section 6.2 presents the experimental setup in MCLAB and explains the necessary corrections used to compare the data with the simulations. Section 6.3 displays the straight path experiments conducted, as well as, the results. Section 6.4 describes the rotational type experiments, and presents the analysis of the results. Finally, Section 6.5 presents the chapter summary.

Publications

The material used in this chapter is based on the following publications

[J1] Mikkel Cornelius Nielsen et al. "Constrained multi-body dynamics for modular underwater robots — Theory and experiments". In: *Ocean Engineering* 149.February 2018 (2018), pp. 358–372

6.1   Introduction

Model-based control is highly dependent on the quality of the model for the derivation of the controller. Therefore, the model developed in Chapter 3, and extended in Chapter 5 has to be tested against a realistic system to verify that the model captures the behavior of the real system.

   The purpose of the interconnected multi-body dynamic simulator is to gain insights into the behavior of a modular underwater robotic system. The developed model is an approximation, as it does not consider potential hull to hull effects.

   The chosen course of action for validation of the model is free motion trajectory tests. Model validation through free motion trajectory tests is similar to the ideas in Chapter 4, where the systems were subjected to actuation, and the trajectories were measured and compared to the simulations. The results from the experiments in Chapter 4 showed, that tight control of the each DOF was necessary to ensure meaningful results. Any deviations in the model parameters will affect the trajectories, and for this reason, it is advantageous to consider a lower dimensional problem. The vehicles chosen for testing in this chapter are the BlueROV. The BlueROV has attitude and depth stabilization functionality. The attitude, and depth stabilization helps reducing the problem from full 6-DOF space to a horizontal 3-DOF problem. The dynamic parameters for the BlueROV were identified in Chapter 5.

   The resulting analysis employs the DTW similarity measure to mitigate error accumulation due to uncertainty in dynamic parameters.

6.1.1   Time-Series Similarity

The proposed type of experiments results in time-series data from the position measurement system. The analysis of the proposed experiments requires the comparison between time-series data. Any comparison requires a measure to evaluate the similarity between the time-series. There exist multiple different similarity measures for time-series data.

   A popular similarity measure for time-series data is the DTW algorithm [20]. The DTW similarity approach is an established approach in areas, such as speech-recognition [183, 191, 140, 80, 139, 138], and time-series data classification [187, 35, 62, 171, 88, 172].

   As spoken words are equal in shape, but not necessarily in timing, the DTW helps to overcome the temporal distortion in speech patterns by transforming the data, in a non-linear fashion. The concern regarding the computational demands of the algorithm is natural considering the applications such as databases containing a large number of words, and real-time demands for specific applications such as

speech recognition. Multiple publications have considered the computational load and ways to speed up the calculation of DTW algorithm [101, 192, 143].

DTW is not the only algorithm used to compare data. Procrustes distance compares data by estimating a centroid of the data, then shifting, rotating, and uniformly scaling the data to get the best overall fit between two shapes [73, 170]. Hausdorff [136, 244, 16], and Fréchet distance [37, 221, 60, 47] are other measures used to conduct data shape analysis.

In this chapter, the DTW analysis is used to compare the shapes of the trajectories between the measured data, and the simulated data. The distance measure is the Euclidean distance of the warped path.

$$\delta\left(i,\ j\right) = \left(x_i - y_j\right)^2 \tag{6.1}$$

Two fundamental properties of the DTW algorithm is outline below:

Monotonicity Points can only stay or increase at the current value.

Continuity The steps taken must be in the neighborhood of the current point.

The monotonicity ensures the ordering of the points with respect to time, while the continuity ensures the choices of points stay coherent with the time-series data. Additional conditions can be imposed to increase the computational speed of the algorithm [20].

Warping Window Allowable points can be constrained to lie within a warping window, $|i_k - j_k| \leq \epsilon$, where ϵ is a constant.

Slope Constraint Allowable paths can be constraints by a slope condition to avoid large movements in a single direction

Boundary Condition Naturally, the lengths of the signals imposes natural boundaries for the algorithm.

However, Ratanamahatana and Keogh [186] note that for most practical problems, the CPU workload is not enough to commit significant resources in speeding up the algorithm.

The algorithm calculates the accumulated cost $\gamma\left(i,\ j\right)$ by:

$$\gamma\left(i,\ j\right) = \delta\left(i,\ j\right) + \min[\gamma\left(i-1,\ y\right),\ \gamma\left(i-1,j-i\right),\gamma\left(i,\ j-1\right)]. \tag{6.2}$$

To exemplify the problem, we revert to the pendulum problem in Chapter 3. The model from Eq. (3.78) is restated here:

$$\ddot{\theta} = -\frac{g}{l^2}\left(\tilde{r}_y^b\cos(\theta) - \tilde{r}_z^b\sin(\theta)\right) - \frac{D_Q l|\dot{\theta}|\dot{\theta} + D_L\dot{\theta}}{m}$$

The inertia of the system depends on the length l. Small differences in the length l have a significant impact on the period of the oscillation. Running two simulations with $l = 0.25m$, and $l = 0.3m$ produces two time-series of θ. Fig. 6.1 shows a 2D histogram with the distance between points on the signals (——), and (——) in each cell. Simulating the pendulum twice with 50 samples yields a grid with 2500 grid points. Starting in lower right corner with $i = j = 0$, the algorithm must reach
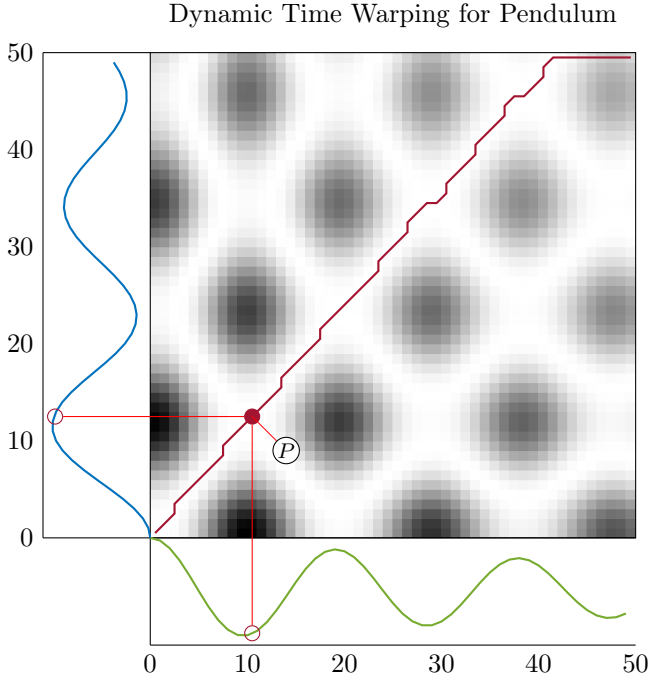
Figure 6.1: DTW diagram between two pendulums with different rod length l. The θ signal for each pendulum simulation shown as (——), and (——) are evaluated at each point with respect to the other signal forming a 2D historgram. The DTW algorithm finds the lowest cost route between sample 0 and sample 50. The cost at point P is low because the points on the curves are close to each other at the specific sample.

$i = j = 50$. (——) marks the DTW path solution.

Applying the DTW path solution to the time-series data changes the mapping between points. Fig. 6.2 shows the mapping between trajectories using unmodified temporal data in Fig. 6.2a, and the DTW temporal shift in Fig. 6.2b. The y-components of the in Fig. 6.2 are the distances between the graphs evaluating the $\|\cdot\|_2$ of the signals:

$$\|d\|_2 = 3.38 \tag{6.3}$$

$$\|d_{DTW}\|_2 = 0.32 \tag{6.4}$$

6.2 Experimental Implementation

The experimental validation requires two rigidly connected BlueROV vehicles with Qualisys tracking. The following sections describe the implementation of the vehicle connection, and the Qualisys setup.
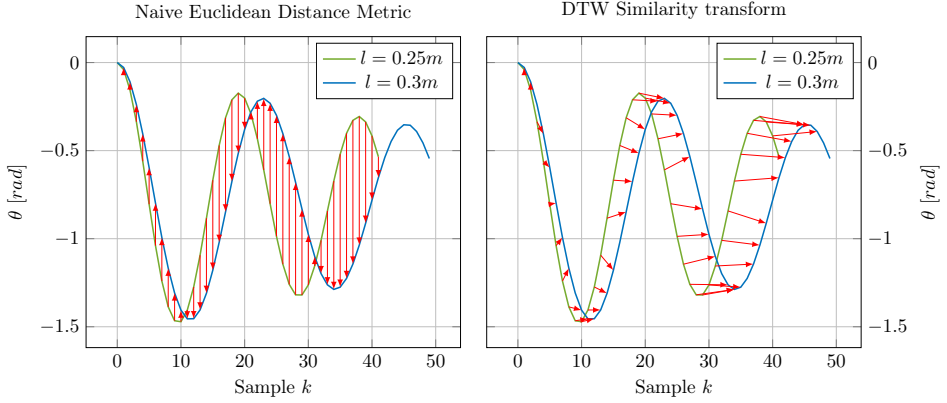
(a) Euclidean Distance metric without temporal shift results in large errors.

(b) DTW shifts points temporally to better match the shapes of the different curves.

Figure 6.2: The matches between a standard Euclidean distance measure without temporal shifts in Fig. 6.2a, and the DTW temporal matching in Fig. 6.2b

6.2.1 Vehicle Connector

A rigid coupling between the hulls implements the physical connector between the vehicles. Fig. 6.3a shows the interconnection between the vehicles. The geometric center is assumed to intersect with the CoM. It is essential to know the vector between the CoM, and the connection point $\boldsymbol{r}^A_{c_A/A}$ and $\boldsymbol{r}^B_{c_B/B}$. $\boldsymbol{r}^A_{c_A/A}$ denote the position vector of connector point c_A with respect to frame A evaluated in frame A. The simulator requires knowledge of the distance between the CoMs of the vehicles as part of the constraint formulation. The link connection has to withstand substantial force and moment. Fig. 6.3b shows the final bracket design. The frame is constructed using four aluminum rods connected between the hulls and stabilized by additional support rods.

The design was chosen to avoid unwanted deformation of the structure during motion. However, the hydrodynamics of the design added significant dynamics to the overall behavior of the system. The added dynamics was added to the overall system as a vehicle node between the two BlueROVs. The connector drag coefficients were obtained through CFD analysis using Ansys Fluent 17.2, while the added mass parameters were obtained using Boundary Element Method (BEM) analysis using WADAM.

Table 6.1: Dynamic Parameters of the connector bracket

$X_{\dot{u}}$ $[kg]$	1.52	$X_{\lvert u\rvert u}$ $[\frac{kg}{m}]$	17.96	X_u $[\frac{kg}{s}]$	0
$Y_{\dot{v}}$ $[kg]$	0.517	$Y_{\lvert v\rvert v}$ $[\frac{kg}{m}]$	14.09	Y_v $[\frac{kg}{s}]$	0.26
$N_{\dot{r}}$ $[kgm]$	0.025	$N_{\lvert r\rvert r}$ $[kgm]$	0.11	N_r $[\frac{kgm}{s}]$	4.64
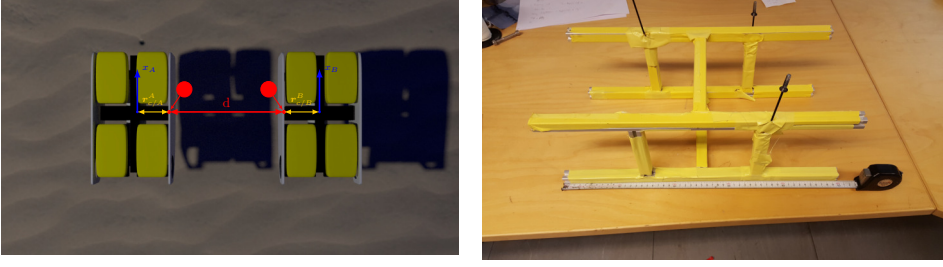
(a) Diagram of the interconnection between the vehicles.

(b) The interconnection bracket with tape to avoid reflections in the Qualisys detection system.

Figure 6.3: Diagram of the interconnection, and the actual interconnection bracket

6.2.2 MCLAB Interface

The Qualisys measurement system is composed of six underwater cameras and uses two frames as reference frames to track vehicles. The global Qualisys frame is a tangential reference frame with an origin defined during calibration of the camera system. For this thesis, the global Qualisys frame will be a NED-like frame with origin $\mathcal{O}_n$. The tracking system estimates the pose of a body-fixed reference frame located on the vehicle based on reflective markers attached to the vehicle.

Origin $\mathcal{O}_Q$, located at one of the reflective markers on the leftmost vehicle, defines the Qualisys body-fixed frame. Fig. 6.4b shows the location of the frame fixed on the interconnected vehicle system. The Qualisys body-fixed axes, denoted $\{Q\}$ as seen on Fig. 6.4b, and the axes of the body-fixed frame of the vehicle itself are aligned. The offset between the body-fixed frame attached to the CoM and the Qualisys body-fixed origin $\mathcal{O}_Q$ measured in the body-fixed frame is denoted $\boldsymbol{p}_{Q/b}^b$ and shown in Fig. 6.4a. The position of the marker in the global frame is found by rotating the body-fixed distance $\boldsymbol{p}_{Q/b}^b$ into the global frame, and adding the position of the origin of the body-fixed frame $\boldsymbol{p}_{b/n}^n$:

$$\boldsymbol{p}_{Q/n}^n = \boldsymbol{p}_{b/n}^n + \boldsymbol{R}_b^n \boldsymbol{p}_{Q/b}^b \tag{6.5}$$

Differentiation of Eq. (6.5) yields the velocity of the marker position:

$$\boldsymbol{v}_{Q/n}^n = \boldsymbol{v}_{b/n}^n + \boldsymbol{\omega}_{b/n}^n \times \boldsymbol{R}_b^n \boldsymbol{p}_{Q/b}^b \tag{6.6}$$

The actual displacement between the origin of the Qualisys body-fixed frame $\mathcal{O}_Q$, and the body-fixed frame of the vehicle itself $\mathcal{O}_b$ is found through SolidWorks CAD model to be:

$$\boldsymbol{p}_{Q/b}^b = [0.2415, \quad -0.165, \ 0]^T. \tag{6.7}$$

The kinematics of Eq. (6.5), and Eq. (6.6) is added to the simulation output to allow for comparisons between the real data and the simulated data. The Qualisys data is published on the internal laboratory network, and interfaced with ROS through the qualisys ROS-package[1].

---

[1] https://github.com/KumarRobotics/qualisys
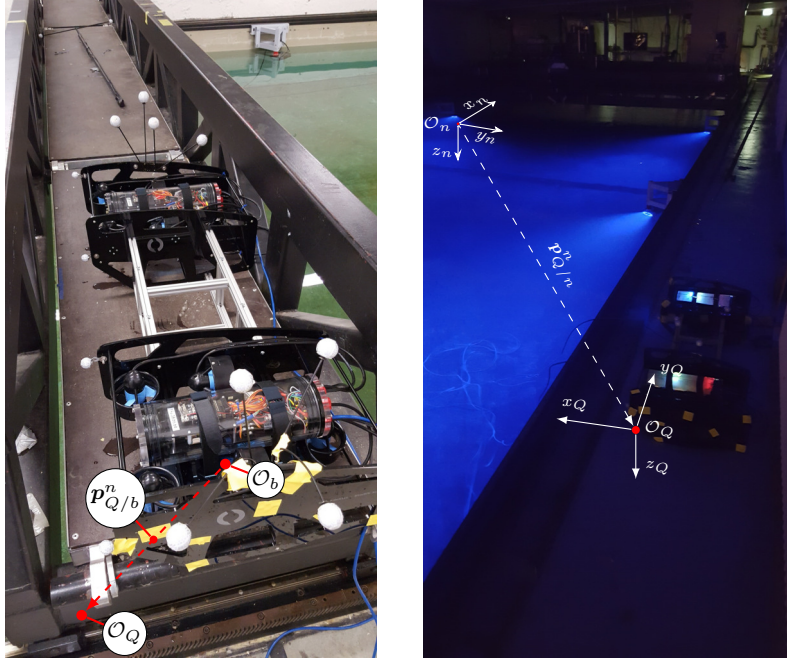
(a) Two BlueROV vehicles joined together by a connection piece made from aluminium profiles. The origin of the body-fixed Qualisys frame $\mathcal{O}_Q$ and the origin of the vehicles body-fixed frame $\mathcal{O}_b$ are marked in red with the lever-arm vector $\boldsymbol{p}^n_{Q/b}$ shown.

(b) The experimental setup with the active QUALISYS motion capture system in the background. The fixed and moving Qualisys frames denoted $\mathcal{O}_n$ and $\mathcal{O}_Q$ respectively can be seen.

Figure 6.4: The interconnected ROV system used in the validation procedure for the multi-body modelling method.

The master computer controls the thruster with PWM using a ROS-interface, which connects to both the vehicles computers, and the Qualisys data network. The vehicles publish their current thruster PWM settings at a fixed rate on the network. The messages contain a timestamp with the local time of the computer generating the message. The timestamps require synchronization between the master computer and the vehicles. Network Time Protocol (NTP) was used to ensure time synchronization. The PWM and Qualisys signals of the vehicles were logged at 50 Hz and 200 Hz, respectively. All the signals on the network were logged by the master computer.

6.2.3   Kinematic Kalman Filter

The Qualisys positioning system only measures the pose of the attached coordinate frame. However, the actuation of the vehicles occurs on acceleration level. The difference in the type of measurement and input leaves a relative degree of 2 between the applied input and measured output. The relative degree means any error in the single-vehicle parametric identification will aggravate twice through integrators.

The single-vehicle model is an approximation based on polynomials, and any comparison results between the pose of the measurements and the simulations will not fit accurately. To augment the analysis, a kinematic Kalman Filter (KF) is employed to estimate the velocities based on the position data,

$$\hat{\boldsymbol{x}}_{k|k-1} = \boldsymbol{F}_k \hat{\boldsymbol{x}}_{k-1|k-1}, \tag{6.8}$$
$$\boldsymbol{P}_{k|k-1} = \boldsymbol{F}_k \boldsymbol{P}_{k-1|k-1} \boldsymbol{F}_k^T + \boldsymbol{Q}_k,$$

where $\boldsymbol{F}_k$ is the discretized state-space model, $\boldsymbol{P}_{k|k-1}$ is the predicted covariance matrix, and $\boldsymbol{Q}_k$ is the state uncertainty matrix. $\hat{\boldsymbol{x}}_{k-1|k-1}$ and $\hat{\boldsymbol{x}}_{k\ |k-1}$ is the corrected state vector of the previous sample, and the predicted state vector based on previous sample state estimation. The correction phase uses the discrepancies between model, and measurement to obtain a residual, which then drives the update of the KF gains and subsequent correction of the state estimate. The residual and correction matrices are found as follows:

$$\tilde{\boldsymbol{y}}_k = \boldsymbol{y} - \boldsymbol{H}_k \hat{\boldsymbol{x}}_{k|k-1}, \tag{6.9}$$
$$\boldsymbol{S}_k = \boldsymbol{H}_k \boldsymbol{P}_{k|k-1} \boldsymbol{H}_k + \boldsymbol{R}_k, \tag{6.10}$$
$$\boldsymbol{K}_k = \boldsymbol{H}_k^T \boldsymbol{P}_{k|k-1} \boldsymbol{S}_k^{-1}, \tag{6.11}$$

where $\tilde{\boldsymbol{y}}_k$ is the measurement residual, $\boldsymbol{H}_k$ is the measurement model, $\boldsymbol{K}_k$ is the KF gain matrix, and $\boldsymbol{R}_k$ is the measurement uncertainty matrix. The correction is then applied to the estimates and driven by the residual $\tilde{\boldsymbol{y}}_k$, and the estimated covariance is updated by the KF gain $\boldsymbol{K}_k$ as follows:

$$\hat{\boldsymbol{x}}_{k|k} = \hat{\boldsymbol{x}}_{k|k-1} + \boldsymbol{K}_k \tilde{\boldsymbol{y}}_k, \tag{6.12}$$
$$\boldsymbol{P}_{k|k} = [\boldsymbol{I} - \boldsymbol{K}_k \boldsymbol{H}_k] \boldsymbol{P}_{k|k-1} [\boldsymbol{I} - \boldsymbol{K}_k \boldsymbol{H}_k]^T + \boldsymbol{K}_k \boldsymbol{R}_k \boldsymbol{K}_k^T. \tag{6.13}$$

The model employed to estimate the velocity from the pose is the simple kinematic model as follows:

$$\boldsymbol{F}_k = \begin{bmatrix} 1 & \Delta t \\ 0 & 1 \end{bmatrix} \otimes \boldsymbol{I}_2, \tag{6.14}$$

$$\boldsymbol{H}_k = [\boldsymbol{I}_2, \ \boldsymbol{0}_{2\times 2}],$$

where Δt is the sampling time of the measurement system, and $\otimes$ is the Kronecker product. The Qualisys system is recording the position data at $200Hz$, making the sampling time $\Delta t = 0.005s$. Fig. 6.5 shows an overview of the comparison. The
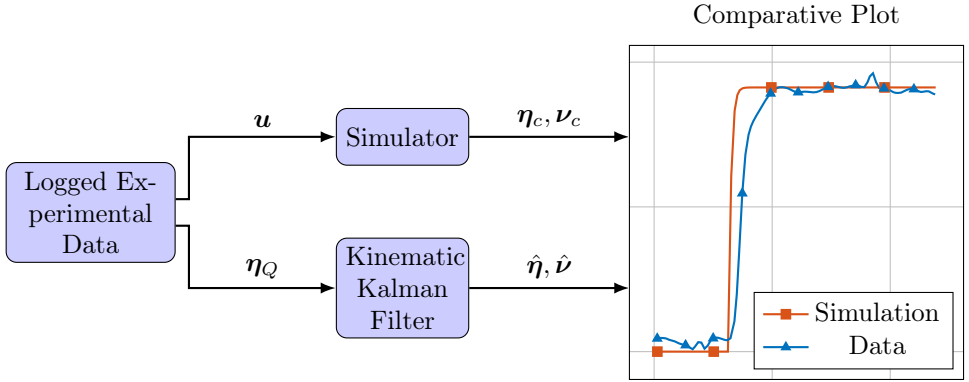
Figure 6.5: The figure shows the method of comparative study. First, the PWM signals logged in the experimental trails and the Qualisys pose vectors are fed to the simulator and Kinematic KF respectively. Thereafter, the resulting pose and velocity vectors of the experimental data and simulation is compared.

simulator, described in Section 3.5 and 5.4.5, take the logged PWM as inputs. The poses, logged by the Qualisys position system, are used in the correction step of the kinematic KF to estimate the velocities. The resulting trajectories and velocities are compared using the DTW similarity measure, and Pearsons R-Correlation.

6.3 Straight Path Experiments

The first proposed experimental validation procedure is the straight path motion. The straight path motion is the most uncomplicated conceivable motion possible, as this isolates the surge DOF dynamics and thereby reduces potential uncertainty introduced by interaction with other DOFs.

As was mentioned in Section 6.1, the depth of the tank restricts the motion of the system to the horizontal plane. The built-in depth controller in the BlueROV maintains the horizontal plane restriction.

Additionally, horizontal plane restriction serves to reduce the number of DOFs in the system, and thereby reduce the accumulated errors resulting from uncertainty in the model parameters. A total number of 14 datasets were collected

Comparison of x-position for dataset

Comparison of y-position for dataset

(a) Comparison between the simulated forward position $\hat{x}$ and the measured forward position x.

(b) Comparison between the simulated sideways position $\hat{y}$ and the measured sideways position y
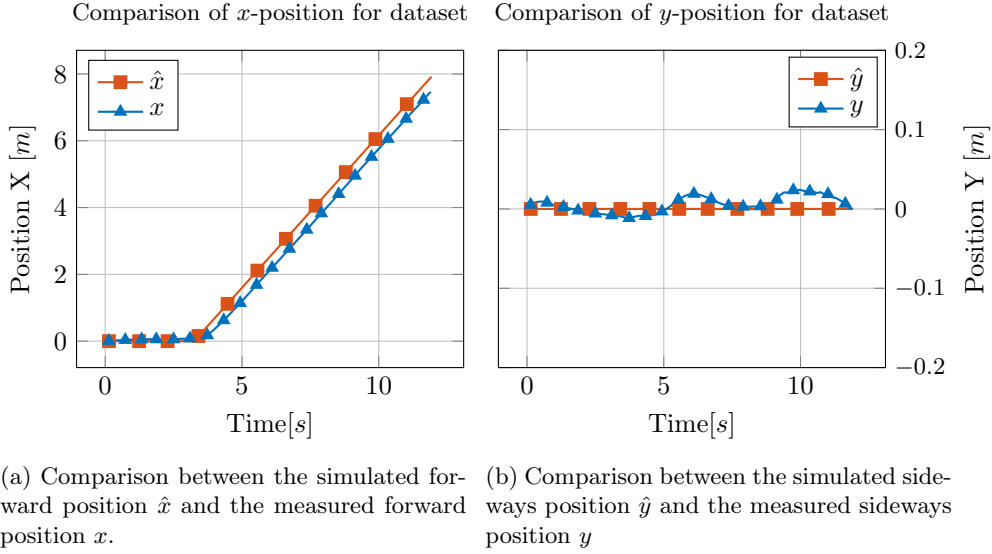
Figure 6.6: Time-series comparison of a straight run dataset in the horizontal plane. The dataset is the last captured set with $1800[\mu s]$ PWM on all surge thrusters.

during the experiments. The length of each dataset spans 12 seconds, where the first 3 seconds are zero-input steady state conditions until the surge thrusters are engaged. Fig. 6.6 shows the X and Y trajectories of both the simulations and the real data.

Fig. 6.6a shows the position of the simulated and measured data along the x-axis. The profiles are in agreement especially for the gradient of the curve. However, there is a time delay between the measurements and simulation after the thrusters are engaged.

Fig. 6.6b shows the position of the simulated and measured data along the y-axis. The simulation $\hat{y}$ is, as expected, zero. However, the real data y shows some fluctuations around zero, but the magnitude are only a few centimeters.

The reason for the offset in Fig. 6.6a is multi-factorial. First, the thrusters are assumed static as the propeller spin-up constant is very small. Secondly, the dynamics of individual thrusters vary slightly. It was noted, in Chapter 5, that the individual RPS of thrusters would vary for the same PWM, and at the same forward velocity. However, from the Figs. 6.6, the trajectory is a straight line and, thus, there is no significant variation in the RPS between the thrusters on each local vehicle or even between them since they follow the same trajectory without deviation of the simulations.

Finally, the tether cables extruding from each of the vehicles are not part of the model. The tether cables introduce additional rigid-body mass, hydrodynamic added mass, and drag, which in turn decreases the acceleration and steady-state velocity of the combined system. Fig. 6.7 support the hypothesis. The comparison between the euclidean norm of the horizontal velocity components from the sim-

Straight Path $\|\boldsymbol{\nu}\|_2$, and $\|\hat{\boldsymbol{\nu}}\|_2$
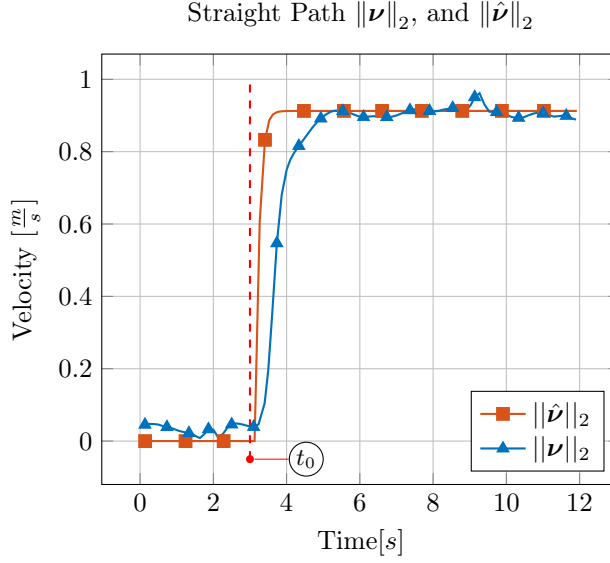
Figure 6.7: Comparison of the simulated and measured velocity profiles denoted $\|\hat{\boldsymbol{\nu}}\|_2$ and $\|\boldsymbol{\nu}\|_2$ respectively. The time of thruster engagement is marked by the line - - - . The horizontal steady-state velocity is identical between the simulation, and the real data. However, the rise-time of the real system is slightly slower than that of the simulation.

ulation and measurements, shows that rise-time of the simulation is smaller than that of the measurements, while the difference in steady-state conditions is negligible. The result suggests, that the cable drag is a non-significant factor, which makes sense, since the cables were dragged after the vehicles and, thus, remained streamlined to the direction of flow. Using the drag coefficient of a flat plate in turbulent conditions, the drag force of the cable is estimated as:

$$F_d = \frac{1}{2}\rho d\phi C_t |u_a|u_a L \;=\; 0.12|u_a|u_a L, \tag{6.15}$$

where L is the length of the cable, u_a is the water flow velocity, C_t is the drag coefficient, and d is the diameter of the cable. For the case in Fig. 6.7, the velocity is $0.9\ \frac{m}{s}$, and the vehicles manage to reach $8\ m$ from the initial point. The added drag increases as a function of the length of the cable. From Eq. (6.15), the cable drag at the end of the motion becomes:

$$F_d = 0.12|0.9|0.9 \cdot 8 \;=\; 0.77N,$$

which is negligible compared to the vehicles and connector itself by a factor of 32 and 16, respectively.

There is a notable discrepancy between the initial conditions in Fig. 6.7. The discrepancy is a result of the depth and attitude hold controller of the vehicle. The attitude controllers of the vehicles were initially Proportional-Integral-Derivative
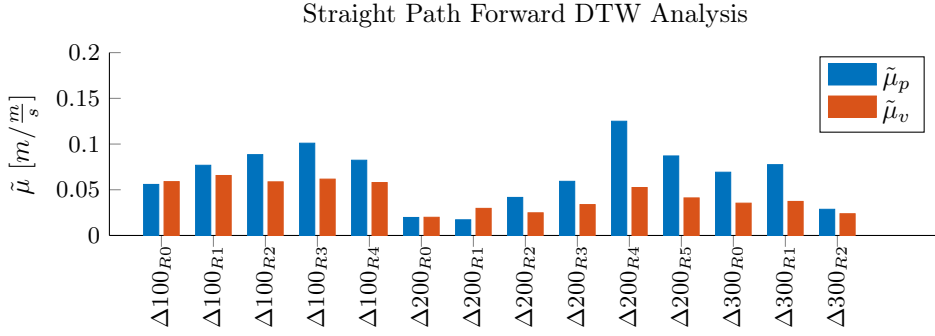
Figure 6.8: Average $||\cdot||_2$ error distance $\tilde{\mu}$ between the simulation and the positional data and velocity data respectively for the straight path trials. The x-axis shows the datasets named by their difference from the baseline $1500[\mu s]$. The average error distance is low compared to the total distance travelled.

(PID) type controllers, However, small differences in the estimated attitude in each vehicle induced integrator wind-up in the controllers. Therefore, the integral term of the controllers was removed at the cost of small steady-state errors in the attitudes.

As mentioned, the x-position on Fig. 6.6a was identical between the simulation and measurement except for a time delay. The same is true for the velocity on Fig. 6.7.

This time-delay has a profound impact on trajectory outcome of the simulation versus the data. Using DTW from Section 6.1 allows warping the time for the curves to match each other better. Fig. 6.8 shows the results of the calculated averages for each data-set, where the x-axis signifies the increased PWM from baseline $1500[\mu s]$ denoted ΔPWM.

Fig. 6.6, and 6.7 shows the data from $\Delta300_{R2}$, which has an error of $0.027m$ and $0.025\frac{m}{s}$ respectively. Overall the average errors between the simulations and the measurements are upper bounded by $0.15m$ and $0.1\frac{m}{s}$ respectively.

The Pearson R Coefficient is added to complement the DTW analysis. The Pearson Coefficient measures correlation between variation in time-series data. Fig. 6.9 shows the correlations between the x-position of the simulation and measurements and the normed velocity of the simulation and measurements. The y-position of the simulation on Fig. 6.6b was not excited, while the data measurements showed a few centimeters of fluctuations around the zero axis. The zero excitation leaves no variation in the time-series, whereas the data has variation.

6.4   Rotational Experiments

The first experimental validation procedure restricted the motion to the surge DOF and avoided rotational dynamics. This section expands the analysis from non-rotational to rotational excitation in combination with translational motion.
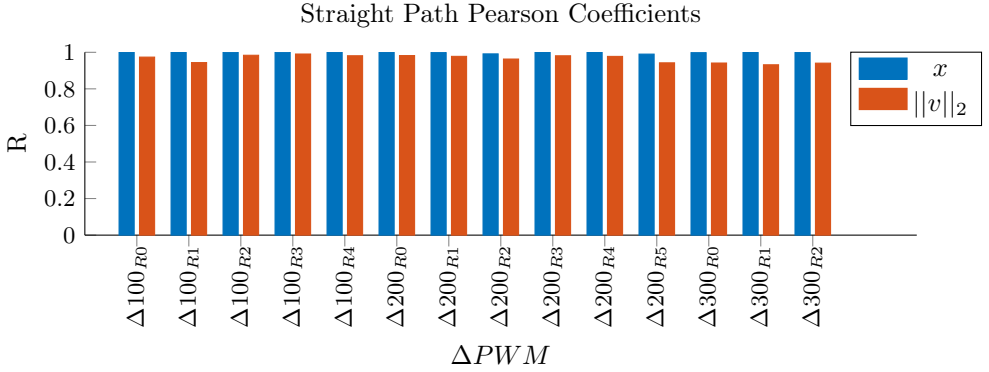
Figure 6.9: Pearson R coefficients for the forward position x and the euclidean norm of the velocity vector $||v||_2$ for the straight path trails. The x-axis shows the dataset as the difference from the baseline $1500[\mu s]$.

The experiment is implemented by only engaging the surge thruster on one ROV, and leaving the other ROV as dead-weight. The motion resulting from this differential thruster scheme was an initiation of a forward motion for the port side ROV, which in turn triggered a starboard turn from the drag of the right ROV. Fig. 6.10 shows the positional data of a single run. The trajectory of the system forms a circle, which is evident as the x and y components each forms a sinusoidal curve. Fig. 6.10a shows the x position for the simulation, and real data respectively. Qualitatively, the curves follow the same motion. However, an offset occurs after a few seconds of thruster actuation. l_x and $\hat{l}_x$ in Fig. 6.10a visualise the peak-to-peak distance for the data and simulation respectively. Measuring the two peak-to-peak distances yields:

$$l_x = 2.45 \ m, \quad \hat{l}_x = 2.42 \ m. \tag{6.16}$$

The deviation between the peak-to-peak distances, is less than 1%. The y positions for the simulation and real data is shown in Fig. 6.10b. The curves overlap for the first 7 seconds of the simulation until an offset develops. As was the case for the x position, the y position offset is very similar to the x position offset.

$$l_y = 2.34 \ m, \quad \hat{l}_y = 2.41 \ m, \tag{6.17}$$

meaning the y offset is around 3% deviation between the peak-to-peak distances of the signals.

Fig. 6.11 shows the yaw angle ψ and the estimated yaw rate r with the respective simulation equivalents. The yaw rotation in Fig. 6.11a follows the actual data very well both temporally, and spatially. The yaw angle ψ exceeds π around 8.5 seconds into the experiment causing a change of the sign. The heading rate is positive as expected as only the port-side vehicle actuates the system causing a starboard turn. Apart from a time delay in the measurements, the resulting curves are similar. Fig. 6.11b compare the estimated yaw rate of the real data r with the simulated
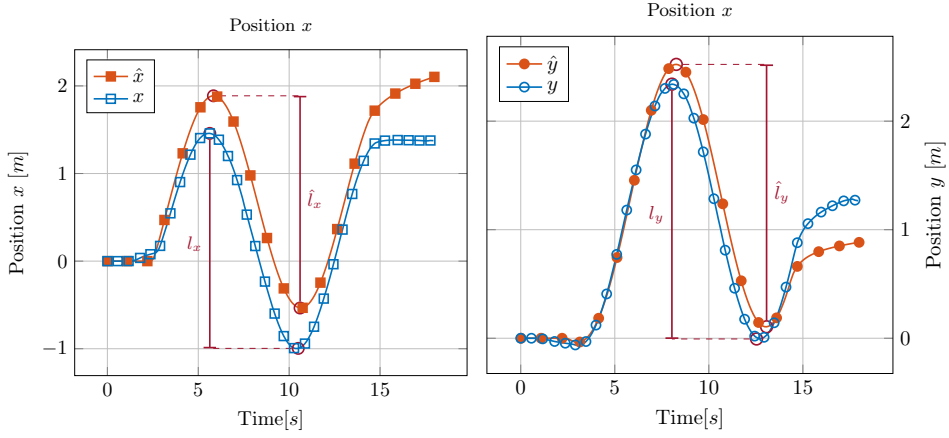
(a) Comparison of simulated x-position of simulated case $\hat{x}$, and measured data $\hat{x}$. Qualitatively the curves are in good agreement. The offset between the curves are equal, and thereby the peak-to-peak length l_x and $\hat{l}_x$ are approximately the same size.

(b) Comparison of simulated y-position of simulated case $\hat{y}$, and measured data $\hat{y}$. The simulation and measured data follow identically for the first 7 seconds. From 7 seconds to the end the qualitative curve is the same with a slight offset. The magnitude of the peak to peak of the two curves are the same.

Figure 6.10: Analysis of single dataset from the rotational trials, where the left-most ROV is engaging surge thrusters at $\Delta 200 \mu s$ forward direction.
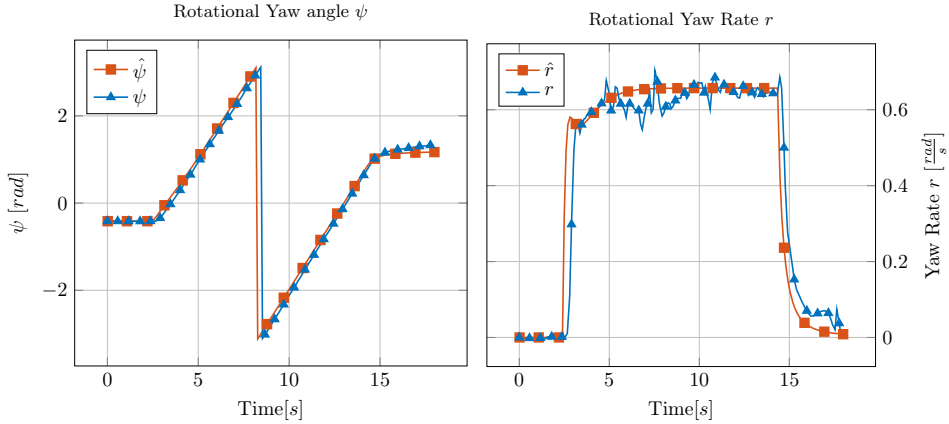
(a) Comparison of the heading angle ψ from the simulated case $\hat{\psi}$ versus the measurements ψ

(b) Comparison of the rotation yaw rate $\hat{r}$ from the simulated case and the experimentally obtained yaw rate r.

Figure 6.11: Analysis of single dataset from the rotational trials, where the portside ROV is engaging surge thrusters at $\Delta 200 \mu s$ forward direction.

yaw rate $\hat{r}$. The yaw rate curves are very well aligned. The estimated yaw rate experience considerable fluctuations around 6 to 10 seconds into the experiment. The fluctuations are due to the Qualisys system loosing track of the pose in a few samples. However, the steady-state yaw rate from 10 seconds and forward matches the simulation very well. Fig. 6.12 shows the euclidean norm of the horizontal
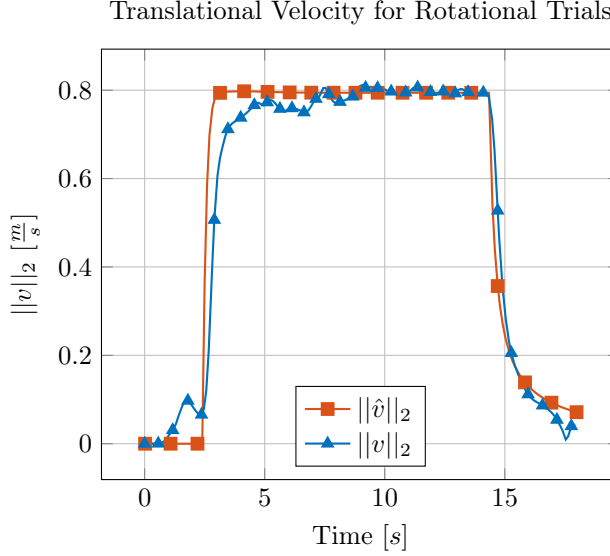
Figure 6.12: Comparison of the euclidean $||\cdot||_2$ of the horizontal velocity components of the simulation $||\hat{v}||_2$ and the measurements $||v||_2$.

velocity vector. However, the difference in rise-time suggests an underestimation of the inertia parameters. The cause of the underestimation is most likely due to the extra mass of the tether wires. The results strengthen the assumption, that any inconsistencies in the translational velocity were from added wire mass as the effect on the rotational inertia should be minimal. The results of the rotational experiments are analyzed using DTW. DTW is neither scale nor rotational invariant, and therefore no analysis of the position data is conducted. Instead, the analysis considers the average heading angle $\tilde{\mu}_\psi$, the euclidean norm of the velocity vector $\tilde{\mu}_{||v||_2}$ and the body angular velocity $\tilde{\mu}_r$. The results are shown on Fig. 6.13. The errors between the simulations and measurements are small. Finally, Fig. 6.14 shows the Pearson R coefficient for the pose, angular rate and the normed horizontal velocities. Generally the correlation between the curves are high except for $\Delta100_{R0}$, this suggests that the trajectories of the experimental data matches the equivalent simulated cases.

6.5 Chapter Summary

In summary, the chapter presented the model validation for the modular underwater robotic systems model developed in Chapter 3 and 5. The model validation
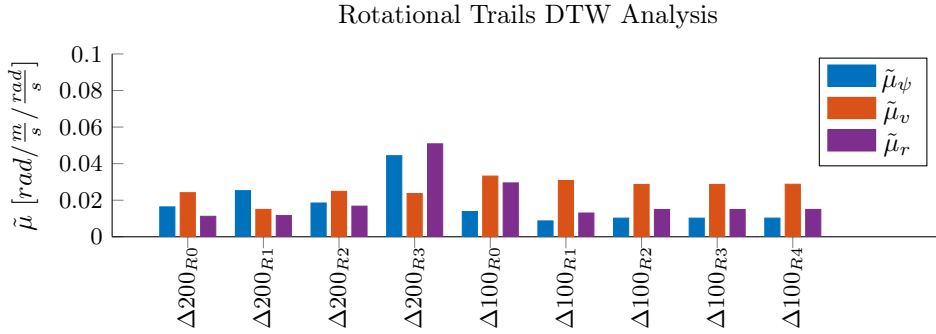
Figure 6.13: The average euclidean error between the simulated and measured heading angle ψ, velocity v and body angular velocity r with the x-axis showing the datasets as differences between the baseline $1500[\mu s]$. The average error is very small suggesting a good agreement in the behavior of the simulations versus the experimental data.
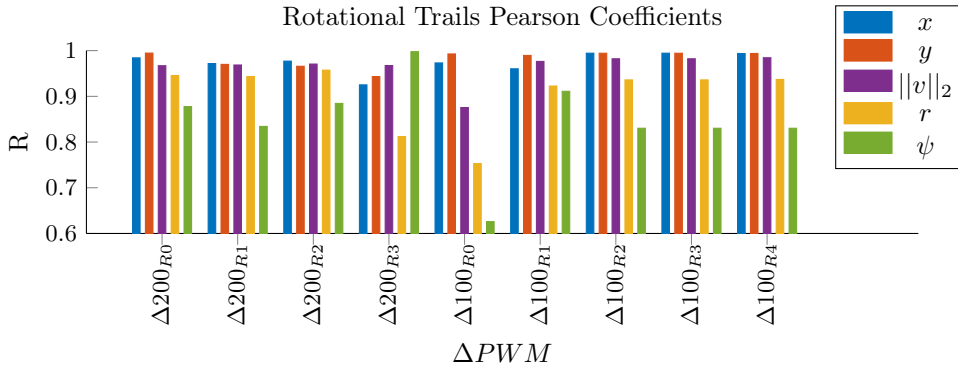
Figure 6.14: The Pearson R coefficients for x, y, $||v||_2$, r and ψ respectively for each of the datasets at different ΔPWM. The correlation between the simulation and experimental data is high.

was based on free motion data obtained in MCLAB at NTNU. A straight-ahead type experiment was conducted to isolate a single DOF, as well as, a rotational type experiment where only one vehicle actuated the whole system. The subsequent data analysis utilized the DTW transform to evaluate the similarity between the measured and simulated trajectories. The model successfully captures the primary behavior of the actual system.

Part II

Control

Chapter 7

Predictive Control for Rendezvous and Docking

The automatic modeling approach of Part I describes the dynamics of a MUR system with settled morphology. Forming a morphology between MURs require physical connection between the robots. Establishing a physical connection between the robots require the robots to rendezvous and dock with each other.

Organization of this Chapter

The organization of the chapter is as follows, Section 7.1 introduces the concept of rendezvous and docking. Section 7.2 introduces the discretization used to convert the continuous model to an equivalent discrete model. Then, the standard MPC is presented in Section 7.3, where the advantage and disadvantage of using such a control approach is considered. Section 7.4 describes the Distributed Model Predictive Control (DMPC), which distributes the optimization problem across multiple nodes. Finally, Section 7.5 completes the chapter with a summary.

7.1 Introduction

The term *Rendezvous* refers to the action of meeting at a specific time and place [151], while the term *docking* refers the action of physically connecting between two bodies. In literature, *docking* and *berthing* often occur interchangeably, but this thesis only uses docking.

The envisioned system introduced in Chapter 1 posits that the MURs are small-sized vehicles that operates in cluttered environments. The size and operational space constraints limits the array of navigation sensors available to the vehicles. Utilization of camera based navigation solves the close-quarter navigation problem by providing a small sized sensor with potential for high accuracy. Camera based navigation has received much attention in the last decades. However, besides the issues related to robustness of computer vision, the camera based navigation suffers a limited field-of-view of the sensor.

Naturally, feedback based on camera navigation require that the camera points in the appropriate direction, such that, the target of interest is within the field-of-view. Therefore, the field-of-view provides a hard-constraint to the control problem. Several authors, in different fields of literature, investigates control methods that take into account the limitations of camera based navigation. In the aeronautical literature, Weiss et al. [233] proposed a MPC for rendezvous and docking for spacecrafts with Line-of-Sight (LOS) constraints. Li and Zhu [121] proposed a non-linear MPC approach to rendezvous spacecrafts with LOS constraint in elliptical orbits. Park, Cairano, and Kolmanovsky [163] investigated rendezvous and docking for a spacecraft and a tumbling/rotating platform with LOS constraints.

In context to underwater vehicles, multiple authors consider the control problem for the camera-based navigation with LOS constraints. Panagou, Maniatopoulos, and Kyriakopoulos [158] proposed a docking algorithm for docking of underactuated underwater vehicles in 3-D space based on potential-fields. Maniatopoulos, Panagou, and Kyriakopoulos [128] applied a MPC to the docking problem of an underactuated underwater vehicle with LOS constraints. Panagou and Kyriakopoulos [157] considered camera-based docking of an underacted vehicle with respect to a stationary target using a switched control law and potential fields for guidance.

In summary, camera based rendezvous and docking is composed of a two part problem with a LOS constraint. In the first stage, the vehicles must approach each other in a rendezvous-fashion, such that, they converge to the same point at the same time. In the second stage, the vehicles connect physically to each other in the docking maneuver. Both stages are subjected to the LOS constraint.

The MPC is an advanced controller that considers both the system behavior through mathematical modeling and the possible restrictions on the control input, as well as, the states themselves. Since the MPC handles constraints directly in the formulation, the controller strategy readily solves the LOS problem. Furthermore, the This chapter presents the basics of the MPC, the necessary notation, and the DMPC.

7.2 Discrete-Time Dynamics

Part I considered continuous-time dynamics, which entailed descriptions of motion followed an ODE.

$$\dot{\boldsymbol{x}}\left(t\right) = \boldsymbol{f}\left(\boldsymbol{x}\left(t\right), \boldsymbol{u}\left(t\right)\right). \tag{7.1}$$

This thesis considers control of discrete form. Hence, the continuous dynamics in Eq. (7.1) require discretization to produce a description of the following form,

$$\boldsymbol{x}_{k+1} = \bar{\boldsymbol{f}}\left(\boldsymbol{x}_{k}, \boldsymbol{u}_{t}\right), \tag{7.2}$$

where $\boldsymbol{x}_{k}$ is the state-vector at time sample k, $\boldsymbol{x}_{k+1}$ is the state at time sample $k+1$ based on the state $\boldsymbol{x}$, and input $\boldsymbol{u}$ at time sample k. Integration of Eq. (7.1) produces the state-transition function $\bar{\boldsymbol{f}}$:

$$\bar{\boldsymbol{f}}\left(\boldsymbol{x}_{k}, \boldsymbol{u}_{k}\right) = \boldsymbol{x}_{k} + \int_{t_{k}}^{t_{k+1}} \boldsymbol{f}\left(\boldsymbol{x}\left(\tau\right), \boldsymbol{u}\left(t_{k}\right)\right) \mathrm{d}\tau, \tag{7.3}$$

where t is the time, t_k is the time at sample k, and h is the sampling time, such that,

$$t_{k+1} - t_k = h. \tag{7.4}$$

Notice, the input $\boldsymbol{u}(t)$ of Eq. (7.3) stays constant over the integration. The complexity of Eq. (7.1) often requires approximation of the integration in Eq. (7.3) by numerical integration. There exist multiple numerical integration procedures. Two simple approaches are the Euler integration and the Runge-Kutta methods. The Euler integration evaluates the dynamic function Eq. (7.1), and scales it with the sampling time to produce an approximation of the next state:

$$\boldsymbol{x}_{k+1} = \boldsymbol{x}_k + h\boldsymbol{f}(\boldsymbol{x}_k, \boldsymbol{u}_k). \tag{7.5}$$

The Euler integration is simple to implement. The cost of simplicity is lack of stability and accuracy. Small sampling times partially mitigate the low accuracy and stability, but this approach increases the computationally cost. The Runge-Kutta method is a popular alternative to Euler integration. This thesis utilizes the explicit Runge-Kutta of fourth order for integration of the continuous dynamics in Eq. (7.1) to produce the discrete state-transition mapping of Eq. (7.2). The following summation of terms describe the explicit Runge-Kutta method:

$$\boldsymbol{x}_{k+1} = \boldsymbol{x}_k + h \sum_{i=1}^{s} b_i k_i, \tag{7.6}$$

where k_i is the ith intermittent function evaluation, h is the sampling time, s is the order of the method, and b represents a scaling factor. The evaluation points $\boldsymbol{k}_i$ calculated as a series based on previous values of $\boldsymbol{k}$. The sequence initializes with,

$$\boldsymbol{k}_1 = \boldsymbol{f}(\boldsymbol{x}_k, \boldsymbol{u}_k). \tag{7.7}$$

The subsequent series of intermittent points $\boldsymbol{k}_i$ are calculated as follows,

$$\boldsymbol{k}_i = \boldsymbol{f}\left(\boldsymbol{x}_k + h \sum_{j=1}^{i-1} a_{i,j}\boldsymbol{k}_j, \boldsymbol{u}_k\right) \text{ for } i = 2, \ldots, s, \tag{7.8}$$

where $a_{i,j}$ are scaling factors. The input $\boldsymbol{u}_k$ stays constant during the evaluation of Eq. (7.7) and (7.8). The scaling factors b_i and $a_{i,j}$ results from the Butcher's tableau depending on the order of the method employed [30]. Tab. 7.1 shows a Butcher's tableau for a generic order explicit Runge-Kutta method. The c_i coefficients denote the time-point at which the state evolution takes place,

$$t_{k,i} = t_k + hc_i. \tag{7.9}$$

Tab. 7.2 shows the Butcher's tableau for Runge-Kutta of fourth order. The trial

c_1				
c_2	$a_{2,1}$			
c_3	$a_{3,1}$	$a_{3,2}$		
$\vdots$	$\vdots$	$\ddots$		
c_s	$a_{s,1}$	$\ldots$	$a_{s,s-1}$	
	b_1	b_2	$\ldots$	b_s

Table 7.1: Butcher tableau for generic order Runge-Kutta method.

0				
$\frac{1}{2}$	$\frac{1}{2}$			
$\frac{1}{2}$	0	$\frac{1}{2}$		
1	0	0	1	
	$\frac{1}{6}$	$\frac{1}{3}$	$\frac{1}{3}$	$\frac{1}{6}$

Table 7.2: Butcher tableau for Runge-Kutta of fourth order.

midpoints $\boldsymbol{k}_i$ from Eq. (7.7) and (7.8) becomes:

$$\boldsymbol{k}_1 = \boldsymbol{f}\left(\boldsymbol{x}_k, \boldsymbol{u}_k\right),$$
$$\boldsymbol{k}_2 = \boldsymbol{f}\left(\boldsymbol{x}_k + \frac{h}{2}\boldsymbol{k}_1, \boldsymbol{u}_k\right),$$
$$\boldsymbol{k}_3 = \boldsymbol{f}\left(\boldsymbol{x}_k + \frac{h}{2}\boldsymbol{k}_2, \boldsymbol{u}_k\right),$$
$$\boldsymbol{k}_4 = \boldsymbol{f}\left(\boldsymbol{x}_k + h\boldsymbol{k}_3, \boldsymbol{u}_k\right).$$

Finally, the integration completes with the evaluation of Eq. (7.6) to yield the subsequent state $\boldsymbol{x}_{k+1}$:

$$\boldsymbol{x}_{k+1} = \boldsymbol{x}_k + \frac{h}{6}\left(\boldsymbol{k}_1 + 2\boldsymbol{k}_2 + 2\boldsymbol{k}_3 + \boldsymbol{k}_4\right). \tag{7.10}$$

The c_i coefficients of Tab. 7.2 shows that the Runge-Kutta of fourth order evaluates the dynamics twice at the time midpoints, and once at the full sampling time.

7.3 Standard Model Predictive Control

MPC is an optimization-based control approach, where the controller determines the control inputs $\boldsymbol{u}$ based on the current state information, and predicts the future states based on a model. The MPC utilizes the state information obtained at each sample instance to simulate the system model over a horizon of N steps using a control sequence. The control sequence results from the optimization problem,
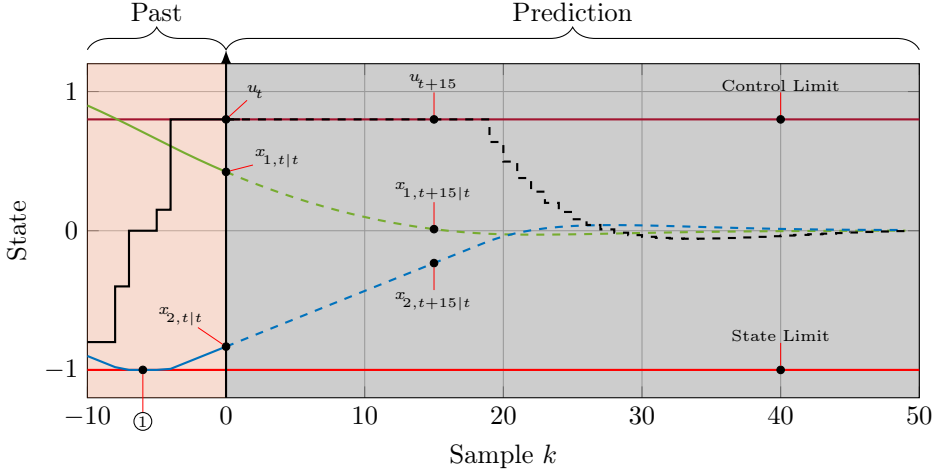
Figure 7.1: The MPC solves an open-loop optimization problem at sample $k = 0$ over a horizon N to obtain a control sequence of length N which is optimal with respect to the cost function J. The controller applies the first element of the control sequence to the plant, and repeats the process. The MPC incorporates control and state restrictions directly in the formulation. The controller enforces the restrictions $u_{max} = 0.8$, and $x_{2,min} = -1$.

which seeks to minimize a cost function. The MPC applies the first element in the obtained control sequence. The system simulates the model from sample $k = 0$ to sample $k = N$. Fig. 7.1 illustrates the principle of the MPC on a two-state system with a prediction horizon of 50 samples.

$\boldsymbol{x}_{1,t|t}$ denotes the first state at time t, $\boldsymbol{x}_{1,t+15|t}$ denotes the future prediction of state one at sample $k = 15$ based on the state information at time t.

The MPC considers restrictions on the control input and the states. The control constraint and the state constraint are shown by (——) and (——) respectively.

At time $k = 0$, the MPC calculates the optimal input to minimize a cost function J over the horizon $k = 50$. The predicted states denoted by (- - -) and (- - -) respectively are calculated based on the mathematical model. The cost function J comprises of two terms, namely the stage-cost and the terminal cost,

$$J\left(\boldsymbol{X}, \boldsymbol{U}\right) = l_N\left(\boldsymbol{x}_{t+N|t}, \boldsymbol{u}_{t+N}\right) + \sum_{k=0}^{N-1} l\left(\boldsymbol{x}_{t+k|t}, \boldsymbol{u}_{t+k}\right), \qquad (7.11)$$

where $l\left(\boldsymbol{x}_{t+k|t}, \boldsymbol{u}_{t+k}\right)$ is the stage-cost function, $l_N\left(\boldsymbol{x}_{t+N|t}, \boldsymbol{u}_{t+N}\right)$, $\boldsymbol{X} \in \mathbb{R}^{n_x \times N}$ consist of all the state-vectors for all times on the horizon N, and $\boldsymbol{U} \in \mathbb{R}^{n_u \times N}$ consist of all the control inputs over the horizon N, such that,

$$\begin{aligned} \boldsymbol{X} &= [\boldsymbol{x}_{t|t}, \boldsymbol{x}_{t+1|t}, \ldots, \boldsymbol{x}_{t+N-1|t}], \\ \boldsymbol{U} &= [\boldsymbol{u}_t, \boldsymbol{u}_{t+1}, \ldots, \boldsymbol{u}_{t+N-1}]. \end{aligned} \qquad (7.12)$$

113

The formulation of an open-loop control problem is then to minimize the cost function $\boldsymbol{J}$ for all the inputs $\boldsymbol{U}$, such that,

$$\underset{\boldsymbol{U}}{\text{minimize}}\, J\left(\boldsymbol{X}, \boldsymbol{U}\right) \tag{7.13}$$

$$
\begin{aligned}
&\text{subject to} \\
&\boldsymbol{u}_{t+k} \in \mathcal{U} \text{ for } k = 1, \ldots, N - 1, \\
&\boldsymbol{x}_{t+k|t} \in \mathcal{X} \text{ for } k = 1, \ldots, N - 1, \\
&\boldsymbol{x}_{t+N|t} \in \mathcal{X}_N, \\
&\boldsymbol{x}_{t+k+1|t} = \bar{\boldsymbol{f}}\left(\boldsymbol{x}_{t+k|t}, \boldsymbol{u}_{t+k}\right) \text{ for } k = 0, 1, \ldots, N - 2,
\end{aligned}
\tag{7.14}
$$

where $\mathcal{X}_N$ is the required terminal state region, $\mathcal{X}$ and $\mathcal{U}$ is the state and input constraint region respectively. The constraint regions usually form convex polyhedrons implemented as linear inequalities. The constraints in Eq. (7.14) are hard-constraints. Thus the solution to problem Eq. (7.13) requires that there exist a feasible solution. In essence, the feasibility condition is a controllability condition. The MPC handles constraints and Multiple-Input-Multiple-Output (MIMO) systems directly in the formulation. The ability to handle constraints constitute a significant advantage as constraints occur naturally in many systems. Conversely, the required computational power necessary to solve the optimization problem poses the primary challenge in employing the MPC.

7.4 Distributed Model Predictive Control

Section 7.3 presented the standard MPC. The computational demands of the MPC require a conscious choice of the formulation, as well as, the number of states in the system. The process industry has successfully employed standard MPCs for large-scale systems [180, 181, 68]. The success partly rests on the slow dynamics of the processes, which allows for more computational time between samples, and partly due to a neglectable interaction between processes, which allows for a decentralized design of controllers.

Scattolini [199] reviews the contemporary methods in decentralized, distributed, and hierarchical MPC methods. Fig. 7.2 shows a decentralized control architecture, where the two subsystems v_1 and v_2 respectively operate with a neglectable state interaction. Since the state interaction is neglectable, the control design handles the interference of the other plants as disturbances.

A MUR comprises of fast dynamics, which require higher control sampling rate. Thus, the sampling time imposes limitations on the computational time of the optimization algorithm. Systems comprised of MURs represents another control problem with a high number of states. Moreover, the physical reconfiguration of the robots is not neglectable. The non-neglectable interaction between the robots violates the assumptions of the decentralized approach to control. Thus, the MUR system requires distributed control to account for the interaction. Fig. 7.3 shows the distributed control architecture. The solid lines ⇆ denote the non-neglectable state interaction between plant v_1 and v_2.
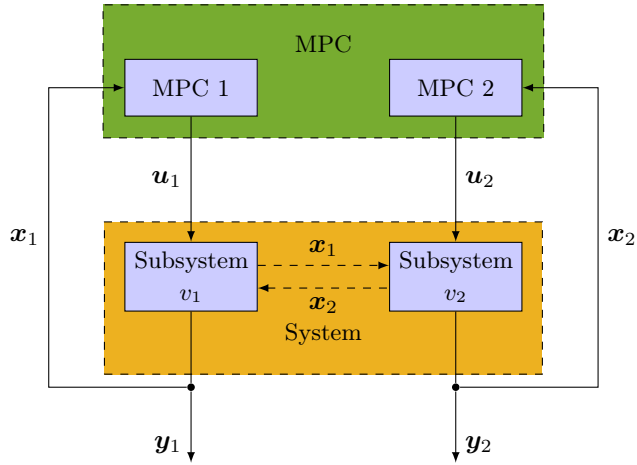
Figure 7.2: The decentralized architecture considers the state interaction as neglectable disturbances, and the decentralized MPCs acts as standard MPCs [199].
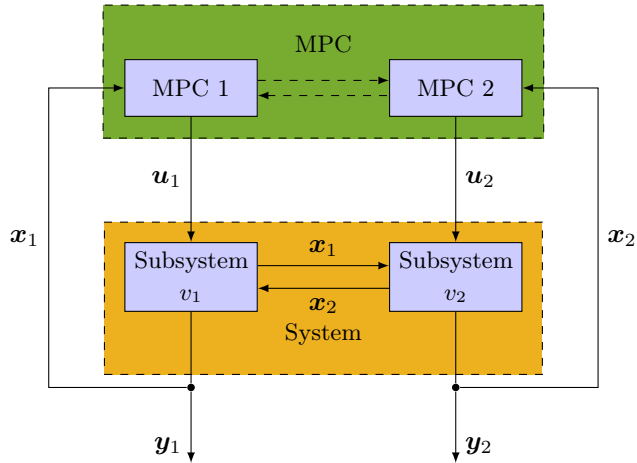
Figure 7.3: The distributed control architecture considers the non-neglectable state interaction between the plants by synchronizing the controllers [199].

7.4.1 Graph Notation

Graphs are standard mathematical tools for dealing with complex interconnected systems, and in this thesis, the graphs provide a foundation for the cooperative control.

Consider a multi-vehicle system comprised of n MURs. The MURs interact through a network defined by a graph-topology $\mathcal{G}$. Fig. 7.4 shows an example interconnection of a graph-topology, where each node v_i correspond to a MUR, and the edge e_{ij} comprise of the set of connecting nodes, such that,

$$e_{ij} = \{v_i, v_j\}, \; e_{ji} = \{v_j, v_i\}. \tag{7.15}$$

In undirected graphs, the edge does not contain directional information, and therefore $e_{ij} = e_{ji}$ for undirected graphs. For directed graphs, digraphs, the edge impose a direction. Thus, $e_{ij} \neq e_{ji}$ for digraphs. This thesis does not consider multi-graphs, that is graphs with multiple edges between two nodes. In turn, only one instance of the edge exists for digraphs, either e_{ij} or e_{ji}.

Together the set of vertices $\mathcal{V}$ and the set of edges $\mathcal{E}$ constitute a graph $\mathcal{G}$.

$$\mathcal{G} = \{\mathcal{V}, \mathcal{E}\}. \tag{7.16}$$

The MUR in the graph has a set of neighbors $\mathcal{N}_i$ consisting of all vertices in the graph connected to the MUR,

$$\mathcal{N}_i(\mathcal{G}) = \{v_j \in \mathcal{V} \mid \{v_i, v_j\} \cap \mathcal{E} \neq \emptyset \vee \{v_j, v_i\} \cap \mathcal{E} \neq \emptyset\}. \tag{7.17}$$

The edge set $\mathcal{E}_i$ contains all the edges connected to node i, such that,

$$\mathcal{E}_i(\mathcal{G}) = \{e \in \mathcal{E} \mid \{v_i\} \cap e \neq \emptyset, \; \forall e \in \mathcal{E}\}. \tag{7.18}$$

Example 7.1: Edge Set, and Neighbors

Considering the network in Fig. 7.4b, the neighborhood $\mathcal{N}_2$ comprise of all other nodes than v_2, such that,

$$\mathcal{N}_2 = \{v_1, v_3, v_4\}. \tag{7.19}$$

Since node v_2 connects to all other nodes, the edge set $\mathcal{E}_2$ equals the full set,

$$\mathcal{E}_2 = \mathcal{E}. \tag{7.20}$$

Node v_1 only connects to node v_2, thus the neighborhood set $\mathcal{N}_1$ only contains node v_2,

$$\mathcal{N}_1 = \{v_2\}. \tag{7.21}$$

The edge set of node v_1 contains only one connection: $\{v_1, v_2\}$. Thus,

$$\mathcal{E}_1 = \{\{v_1, v_2\}\}. \tag{7.22}$$

Example 7.1 provides an example of the edge set of the digraph from Fig. 7.4b. Eq. (7.17) produces identical neighborhood sets for the undirected graph of Fig. 7.4a and the digraph of Fig. 7.4b. However, the edge set may differ between the graphs since the digraph contains ordered edges. The cardinality of the edge sets is identical due to neither graphs being multi-graphs. This thesis applies arbitrary direction
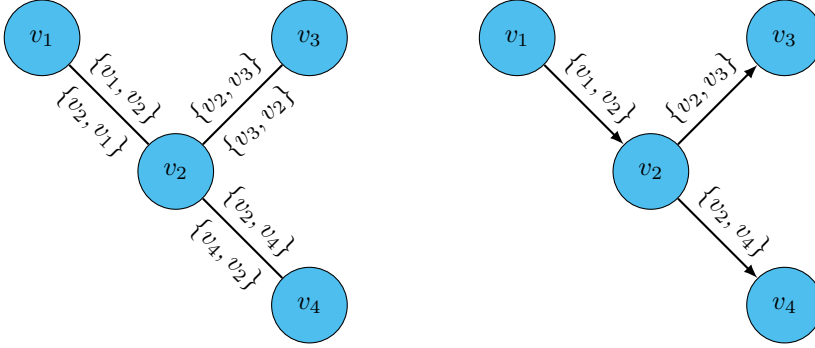
(a) The un-directed graph contains no directional meaning on the edges. Thus, edge $\{v_i, v_j\}$ and the reverse $\{v_j, v_i\}$ are equal.

(b) The directed graph removes the edge ambiguity by imposing direction on the edge.

Figure 7.4: Interconnection between the vehicles represented as nodes.

to undirected graphs to avoid ambiguity in the edge sets.

7.4.2 Dual Decomposition

Consider a graph with three interconnected systems, such that $n = 3$. The cost function J comprises of the cost function contributions associated with each vehicle,

$$J\left(x_1, x_2, x_3, y, z\right) = J_1\left(x_1, y\right) + J_2\left(x_2, y, z\right) + J_3\left(x_3, z\right). \tag{7.23}$$

The desire to minimize Eq. (7.23) yield an unconstrained optimization problem on centralized form,

$$\mathcal{P}_{uc} \; : \; \underset{\boldsymbol{x}}{\text{minimize}} \, J_1\left(x_1, y\right) + J_2\left(x_2, y, z\right) + J_3\left(x_3, z\right), \tag{7.24}$$

where $\boldsymbol{x} = [x_1, x_2, x_3, y, z]$. $\mathcal{P}_c$ contains five decision variables and thereby represents a small-scale problem. Separating the cost function of Eq. (7.24) allows for parallelism of the optimization problem. However, the cost functions J_1 and J_2 both depend on the variable y, while the cost function J_2 and J_3 depends on z. Evidently, the variables y and z couples J_1 and J_2, and J_2 and J_3 respectively. Fig. 7.5 shows the system graph with an arbitrary direction applied. The couplings complicate the decomposition of the cost function. Fortunately, dual decomposition solves the problem from Eq. (7.24) by introducing a local version of y and z at the respective systems, and then impose a coupling constraint between the independent variables. The minimization problem then changes from a purely unconstrained problem to
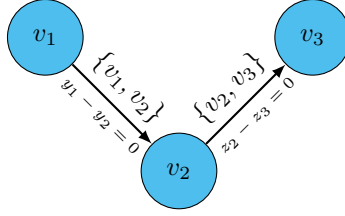
Figure 7.5: Example of graph interconnection between three nodes. The arbitrary direction on the edges result in specific signs on the variable constraints, which is shown under the edges.

a equality constrained problem as follows,

$$
\mathcal{P}_c \; : \; \begin{cases} \underset{\bar{x}}{\text{minimize}} \; J_1\left(x_1, y_1\right) + J_2\left(x_2, y_2, z_2\right) + J_3\left(x_3, z_3\right), \\ \qquad \text{subject to,} \\ \qquad \bm{h}\left(\bar{\bm{x}}\right) = \bm{0}, \end{cases} \tag{7.25}
$$

where $\bar{\bm{x}} = [x_1, x_2, x_3, y_1, y_2, z_2, z_3]^T$, and $\bm{h}\left(\bar{\bm{x}}\right)$ contains the equality constraints, such that,

$$
\bm{h}\left(\bar{\bm{x}}\right) = \begin{bmatrix} h_{12}\left(\bar{\bm{x}}\right) \\ h_{23}\left(\bar{\bm{x}}\right) \end{bmatrix} = \begin{bmatrix} y_1 - y_2 \\ z_2 - z_3 \end{bmatrix}. \tag{7.26}
$$

Every constraints of Eq. (7.26) associates with an edge in the connection graph, such that, $\bm{h}_{12}$ belongs to e_{12} and $\bm{h}_{23}$ belongs to e_{23}. The equality constraints are linear, and for notation the constraint are put on matrix form.

$$
\bm{A}_{i,c}\bm{x}_i = \bm{0}, \tag{7.27}
$$

where $\bm{A}_{i,c}$ is the constraint matrix of edge c wrt. vehicle i, i. e.,

$$
\bm{A}_{1,12} = \frac{\partial h_{12}}{\partial \bm{x}_1} = [0, \; 1], \tag{7.28}
$$

$$
\bm{A}_{2,12} = \frac{\partial h_{12}}{\partial \bm{x}_2} = [0, \; -1, \; 0], \tag{7.29}
$$

$$
\bm{A}_{2,23} = \frac{\partial h_{23}}{\partial \bm{x}_2} = [0, \; 0, \; 1], \tag{7.30}
$$

$$
\bm{A}_{3,23} = \frac{\partial h_{23}}{\partial \bm{x}_3} = [0, \; -1], \tag{7.31}
$$

where $\bm{x}_1$, $\bm{x}_2$, and $\bm{x}_3$ are the local decision vectors, such that,

$$
\bm{x}_1 = [x_1, y_1]^T, \; \bm{x}_2 = [x_2, y_2, z_2]^T, \; \bm{x}_3 = [x_3, z_3]^T. \tag{7.32}
$$

The constrained problem of Eq. (7.25) is equivalent to the unconstrained problem of Eq. (7.24). The number of decision variables increased from five to seven, with an additional two additional constraints imposed. However, the new formulation

separates the cost functions J_1, J_2, and J_3 to allow parallelism in the minimization procedure. The imposed constraints does complicate the new formulation, but dual decomposition deals with the constraints through Lagrangian Relaxation. The Lagrangian L of each sub-problem becomes,

$$L_i = J_i\left(\boldsymbol{x}_i\right) + \sum_{e \in \mathcal{E}_i} \mu_e \boldsymbol{A}_{i,e}\boldsymbol{x}_i \tag{7.33}$$

The resulting Lagrangians for the sub-problems of the graph in Fig. 7.5 becomes,

$$\begin{aligned}
L_1 &= J_1\left(x_1, y_1\right) + \mu_{12}y_1, \\
L_2 &= J_2\left(x_2, y_2, z_2\right) - \mu_{12}y_2 + \mu_{23}z_2, \\
L_3 &= J_3\left(x_3, z_3\right) - \mu_{23}z_3.
\end{aligned} \tag{7.34}$$

The dual functions of Eq. (7.34) are then:

$$g_1\left(\mu_{12}\right) = \inf_{\boldsymbol{x}_1}\left(J_1\left(x_1, y_1\right) + \mu_{12}y_1\right), \tag{7.35}$$

$$g_2\left(\mu_{12}, \mu_{23}\right) = \inf_{\boldsymbol{x}_2}\left(J_2\left(x_2, y_2, z_2\right) - \mu_{12}y_2 + \mu_{23}z_2\right), \tag{7.36}$$

$$g_3\left(\mu_{23}\right) = \inf_{\boldsymbol{x}_3}\left(J_3\left(x_3, z_3\right) - \mu_{23}z_3\right). \tag{7.37}$$

The dual problem of the dual functions in Eq. (7.35) are then,

$$\underset{\mu_{12}, \mu_{23}}{\text{maximize}}\ g_1\left(\mu_{12}\right) + g_2\left(\mu_{12}, \mu_{23}\right) + g_3\left(\mu_{23}\right) \tag{7.38}$$

The solution to Eq. (7.38) is solved using sub-gradients [21, 26], such that,

$$\mu_e^{k+1} = \mu_e^k + \gamma_e g_e\left(\bar{\boldsymbol{x}}^*\right) \tag{7.39}$$

where γ_e is the step-size of the given edge update, g_e is the constraint related to the edge e, and $\bar{\boldsymbol{x}}^*$ is the optimal state vector used to minimize Eq. (7.35).

7.5 Chapter Summary

The chapter presented the general problem of rendezvous and docking for underwater vehicles. Specifically, the problem of rendezvous and docking for underwater applications with camera constraints was considered. First, an overview of the literature relevant for camera-based rendezvous and docking was presented. The camera-based navigation imposed LOS constraints on the problem. The LOS constraint requires attention on a control level and, therefore, the chapter proposes to apply predictive control to solve the problem. The predictive controllers simulates the model behavior ahead of time to find a sequence of control inputs that optimally minimizes a user-defined cost-function. The applied controllers utilize discrete time dynamics, which requires transformation of the continuous time dynamics. The chapter presented two methods, Euler integration and explicit Runge-Kutta, for transforming continuous plant dynamics from discrete time equivalents. Then, the concept of a standard MPC was briefly introduced. Finally, the chapter introduced the DMPC by dual decomposition to distribute the control problem among the MURs.

Chapter 8

Rendezvous and Docking using Distributed Model Predictive Control

Reconfiguration of a MUR system require physical attachment, and detachment between the robots. Furthermore, the act of attaching to each other encompass the same difficulties as those of the rendezvous and docking problem.

Contribution

The contribution of this chapter is a cooperative docking algorithm which allows the MURs to rendezvous and dock with each other.

Organization of this chapter

The organization of this chapter is as follows:
Section 8.2 describes the model dynamics employed in the Chapter. Section 8.3 presents the control problem in a centralized fashion. In Section 8.4 the distributed controller is derived from the centralized problem using dual decomposition. Section 8.5 presents and discusses the results of the simulation. Finally, in Section 8.6, the conclusion is given along with considerations of future work.

Publications

The material used in this chapter is based on the following publication,

[C3] Mikkel Cornelius Nielsen, Tor Arne Johansen, and Mogens Blanke. "Cooperative Rendezvous and Docking for Underwater Robots using Model Predictive Control and Dual Decomposition". In: *2018 European Control Conference (ECC)*. Limassol, Cyprus: IEEE, 2018, p. 6

8.1   Introduction

The issue of multi-vehicle rendezvous and docking with multiple objectives, input constraints, and visual constraints pose a challenging problem. MPC is an advanced control strategy often employed to solve problems where constraints pose a central issue in the objectives. Several authors, [36, 59, 102], have investigated DMPC. Dual decomposition is a frequently applied method, which decomposes a large central optimization problem into smaller sub-problems that can be solved locally.

The decomposition transforms the coupled objective function into decoupled objective functions with coupling constraints. Afterwards, the constraints are relaxed using Lagrangian relaxation and the individual vehicles enforce the coupling constraints by manipulation of the dual variables. Multiple authors, [72, 185, 108, 74], have exploited the dual decomposition technique in various contexts. However, none have considered multi-vehicle docking.

The strategy utilizes a DMPC by dual decomposition to achieve rendezvous while the vehicles maintain visual contact with each other. The rendezvous problem is solved as a consensus problem solved by introducing a consensus point with a coupled equality constraint between the vehicles. Inspired by, [164] and [163], the visual constraint of the cameras are constructed as inequalities. The constraints are decomposed using dual decomposition and subsequently relaxed by Lagrangian relaxation. The dual variables are then updated by negotiation between neighboring vehicles to thereby enforce the relaxed constraints.

8.2   Modeling

For brevity, the docking algorithm proposed in this chapter only considers the planar case. This dimensional reduction imposes an assumption on the free degrees of motion,

> **Assumption 8.1** (3-DOF). *The dive-plane is stabilized by an active attitude-heave control system.*

Thereby, the assumption removes the roll, pitch, and heave from the problem and only leaves the surge, sway, and yaw degrees for control. The vehicles employes the $\{n\}$, and $\{b\}$ frames introduced in Chapter 2. However, the coordinates of the pose vector $\boldsymbol{\eta}$ and the velocity vector $\boldsymbol{\nu}$ reduces to the control degrees, The pose of a vehicle in the global frame is denoted $\boldsymbol{\eta}$ is defined as follows,

$$\boldsymbol{\eta} = [N,\ E,\ \psi]^{T}, \tag{8.1}$$

where N and E are the position coordinates in the North-East frame and ψ is the yaw-angle relative to north. The body-fixed velocity vector is denoted $\boldsymbol{\nu}$ and defined as,

$$\boldsymbol{\nu} = [u,\ v,\ r]^{T}, \tag{8.2}$$

The transformation matrix $\boldsymbol{J}_\psi$ only requires a rotation matrix of the plane,

$$\dot{\boldsymbol{\eta}} = \overbrace{\begin{bmatrix} \cos(\psi) & -\sin(\psi) & 0 \\ \sin(\psi) & \cos(\psi) & 0 \\ 0 & 0 & 1 \end{bmatrix}}^{\boldsymbol{J}_\psi} \boldsymbol{\nu}. \tag{8.3}$$

Figure 8.1 shows the global coordinate frame with the origin denoted $\mathcal{O}_n$ along with the two coordinate frames attached to two vehicles.

8.2.1 Kinetics

Underwater vehicles are affected by hydrodynamic effects. As a consequence a vehicle experiences the effect of hydrodynamic damping and added mass.

$$\boldsymbol{M}\dot{\boldsymbol{\nu}} + \boldsymbol{D}(\boldsymbol{\nu})\,\boldsymbol{\nu} = \boldsymbol{u}, \tag{8.4}$$

where $\boldsymbol{M}$ and $\boldsymbol{D}$ is the inertia, including added mass, and damping matrix respectively defined as follows:

$$\boldsymbol{M} \triangleq \mathrm{diag}\,(m_{11}, m_{22}, m_{33})\,, \ \ \boldsymbol{D} \triangleq \mathrm{diag}\,(d_{11}, d_{22}, d_{33})\,, \tag{8.5}$$

and $\boldsymbol{u}$ being the force input in each DOF. The model Eq. (8.3) and (8.4) is represented on standard ODE form by aggregating the pose and body-velocity vector as follows:

$$\boldsymbol{x} = [\boldsymbol{\eta}^T, \ \boldsymbol{\nu}^T]^T. \tag{8.6}$$

The combined state evolution can then be written as follows:

$$\dot{\boldsymbol{x}} = \boldsymbol{f}(\boldsymbol{x}, \boldsymbol{u})\,. \tag{8.7}$$

When considering multiple vehicles in Section 8.3, the vehicles associated with the i-th vehicle is assigned an index i.

8.3 Multi-Vehicle Model Predictive Control for Docking

This section defines the consensus and visual constraint, as well as, the centralized MPC controller. In this section the two objectives, consensus and visual constraints, are defined and combined into a centralized controller.

8.3.1 Notation

Consider a multi-vehicle system comprised of n agents. The agents interact through a network defined by a graph-topology $\mathcal{G}$. Agent i in the network correspond to a vertex v_i in the graph, the connection between individual agents are defined by the edge $e_{ij} = v_i v_j$. Together the set of vertices $\mathcal{V}$ and the set of edges $\mathcal{E}$ constitute a graph $\mathcal{G}$.

$$\mathcal{G} = \{\mathcal{V}, \mathcal{E}\}. \tag{8.8}$$

Each agent in the graph has a set of neighbors $\mathcal{N}_i$ consisting of all vertices in the graph connected to the agent

$$\mathcal{N}_i(\mathcal{G}) = \{v_j \in \mathcal{V} \mid \{v_i, v_j\} \cap \mathcal{E} \neq \emptyset \vee \{v_j, v_i\} \cap \mathcal{E} \neq \emptyset\}. \qquad \text{(7.17 restated)}$$

Recalling from Chapter 7 that the edge set of the local node is,

$$\mathcal{E}_i(\mathcal{G}) = \{e \in \mathcal{E} \mid \{v_i\} \cap e \neq \emptyset, \ \forall e \in \mathcal{E}\}. \qquad \text{(7.18 restated)}$$

8.3.2 Line-of-Sight Constraints

The navigation of the MURs utilize optical navigation for both the rendezvous and docking phase. THe optical navigation is camera based. The camera based navigation requires constant line-of-sight to the target. Inspired by work in [163], [164]
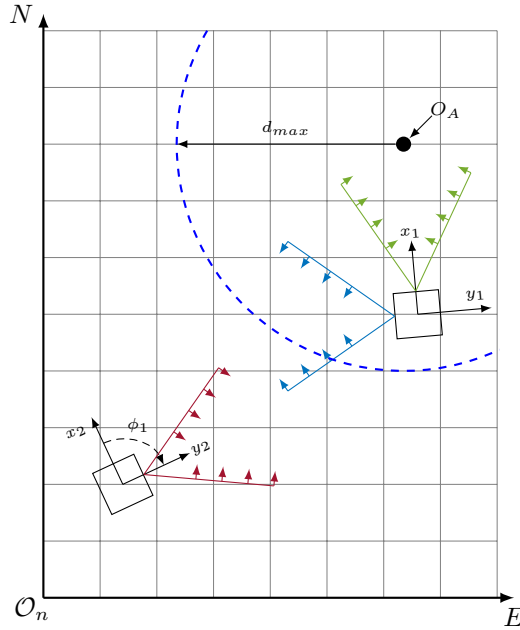
Figure 8.1: Figure shows a multi-vehicle system consisting of two vehicles v_1 and v_2 as well as an object O_A. The camera cones are shown in brown, blue and green respectively along with the constraint direction. ϕ_1 on v_2 shows the relative rotation between the onboard camera and the vehicle.

and [165] the *line-of-sight* (LOS) constraints can be formulated as follows,

$$\begin{aligned}
\boldsymbol{n}^+_{i,j} \boldsymbol{e}_{j,i} \leq 0, \ \text{for} \ \forall v_i \in \mathcal{V} \ \wedge \ v_j \in \mathcal{N}_i, \\
\boldsymbol{n}^-_{i,j} \boldsymbol{e}_{j,i} \leq 0, \ \text{for} \ \forall v_i \in \mathcal{V} \ \wedge \ v_j \in \mathcal{N}_i,
\end{aligned} \qquad (8.9)$$

where the normal vectors $\boldsymbol{n}^+_{i,j}$ and $\boldsymbol{n}^-_{i,j}$ are parameterized in the ith vehicles respective camera rotation. Notice, that the $\boldsymbol{n}$ vectors are parameterized in the states,

and thus are time-varying. The $\boldsymbol{e}_{j,i}$ is the relative position between the vehicle in the global frame and is assumed measured by the local camera.

$$\boldsymbol{e}_{j,i} = [N_j - N_i, E_j - E_i]^T.$$

The parameterizations of the normal vectors $\boldsymbol{n}_{i,j}^+$ and $\boldsymbol{n}_{i,j}^-$ are,

$$\begin{aligned}
\boldsymbol{n}_{i,j}^+ &: \begin{bmatrix} -\sin\left(\xi_{i,k} + \alpha_k\right) & \cos(\xi_{i,k} + \alpha_k) \end{bmatrix}, \\
\boldsymbol{n}_{i,j}^- &: \begin{bmatrix} \sin\left(\xi_{i,k} - \alpha_k\right) & -\cos(\xi_{i,k} - \alpha_k) \end{bmatrix},
\end{aligned} \tag{8.10}$$

where α_k is the camera half-angle of the visual cone for camera k, $\xi_{i,k}$ is the direction of the cone relative to the global frame $\xi_{i,k} = \psi_i + \phi_k$ with ϕ_k being the relative rotation between the vehicle i's local x-axis and the visual cone of camera k. Fig. 8.1 shows the camera cone of two vehicles with respect to each other and a target.

8.3.3 Consensus Problem

The control objective is to solve the rendezvous problem, meaning for the vehicles to converge to and remain at a common point:

$$\lim_{t \to \infty} ||\boldsymbol{\eta}_i - \boldsymbol{\eta}_j|| = 0 \; \forall v_i \in \mathcal{V} \; \wedge \; v_j \in \mathcal{N}_i, \tag{8.11}$$

$$\lim_{t \to \infty} ||\boldsymbol{\nu}_i|| = 0 \; \forall v_i \in \mathcal{V}. \tag{8.12}$$

The rendezvous objective of Eq. (8.11) is not feasible in practice since the vehicles cannot occupy the same space, however, in combination with the visual constraint the system will converge from a direction defined by the camera cones. Thus the vehicles will collide, but this is the desire as docking requires physical contact. Introducing the vectors $\boldsymbol{x}$, $\boldsymbol{\eta}$, $\boldsymbol{\nu}$ and $\boldsymbol{u}$ as follows,

$$\begin{aligned}
\boldsymbol{\eta} &= [\boldsymbol{\eta}_1^T, \ldots, \boldsymbol{\eta}_n^T]^T, \; \boldsymbol{u} = [\boldsymbol{u}_1^T, \ldots, \boldsymbol{u}_n^T]^T, \\
\boldsymbol{\nu} &= [\boldsymbol{\nu}_1^T, \ldots, \boldsymbol{\nu}_n^T]^T, \boldsymbol{x} = [\boldsymbol{x}_1^T, \ldots, \boldsymbol{x}_n^T]^T,
\end{aligned}$$

where the subscript $\boldsymbol{\eta}_i$ denotes the pose of vehicle v_i. The objective function of the centralized problem is formulated as:

$$J\left(\boldsymbol{X}, \boldsymbol{U}\right) = \sum_{k=0}^{N} l(\boldsymbol{x}_{t+k|t}, \boldsymbol{u}_{t+k}), \tag{8.13}$$

where $\boldsymbol{U}$ is all control inputs for all vehicles across the time horizon $\boldsymbol{U} = [\boldsymbol{u}_t, \boldsymbol{u}_{t+1}, \ldots, \boldsymbol{u}_{t+N}]$, N is the control horizon, $\boldsymbol{X}$ is all the state-vectors over the horizon, and the function $l(\boldsymbol{x}, \boldsymbol{u})$ is defined as:

$$l(\boldsymbol{x}, \boldsymbol{u}) = \boldsymbol{\eta}^T(\boldsymbol{L} \otimes \boldsymbol{P})\boldsymbol{\eta} + \boldsymbol{\nu}^T \boldsymbol{W} \boldsymbol{\nu} + \boldsymbol{u}^T \boldsymbol{R} \boldsymbol{u}, \tag{8.14}$$

where matrix $\boldsymbol{L}$ is the Laplacian matrix of the graph, $\otimes$ is the Kronecker product, $\boldsymbol{P}$, $\boldsymbol{W}$ and $\boldsymbol{R}$ are tuning matrices and

8.3.4 Centralized Problem

The centralized control problem is composed of the consensus problem and the LOS constraints. Thus the overall controller can be formulated as follows:

$$\underset{\boldsymbol{U}}{\text{minimize}}\, J\left(\boldsymbol{X},\boldsymbol{U}\right) \tag{8.15}$$

s.t.
$$\begin{aligned}
&\boldsymbol{u}_{i,t+k} \in \mathcal{U}_i,\; \forall v_i \in \mathcal{V},\\
&\boldsymbol{x}_{i,t+k+1|t} = \boldsymbol{f}_i(\boldsymbol{x}_{i,t+k|t},\boldsymbol{u}_{i,t+k}),\; \forall v_i \in \mathcal{V},\\
&\boldsymbol{n}_{i,j}^{\pm}\boldsymbol{e}_{j,i} \leq 0,\; \forall v_i \in \mathcal{V} \;\wedge\; v_j \in \mathcal{N}_i,\\
&\boldsymbol{x}_{t+k|t} = [\boldsymbol{x}_{1,t+k|t},\boldsymbol{x}_{2,t+k|t},\ldots,\boldsymbol{x}_{n,t+k|t}],\\
&\boldsymbol{u}_{t+k} = [\boldsymbol{u}_{1,t+k},\boldsymbol{u}_{2,t+k},\ldots,\boldsymbol{u}_{n,t+k}],
\end{aligned} \tag{8.16}$$

where $\mathcal{U}_i$ is the input constraints for vehicle v_i.

8.4 Cooperative Model Predictive Control

The controller must be converted into a distributed formulation to employ it in a multi-vehicle system efficiently. This section describes the utility of dual decomposition to distribute the control among the agents.

8.4.1 Rendezvous Problem

The rendezvous problem from Sec. 8.3.3 is solved through the objective function in Eq. (8.15). However, the function itself relies on the difference in the pose of the vehicles due to $\boldsymbol{L}$. Hence the objective function is not separable. Introducing a new consensus parameter vector $\boldsymbol{\theta} \in \mathbb{R}^3$, which acts as a universal rendezvous point for the system, allows for the reformulation of the objective function. The global rendezvous point $\boldsymbol{\theta}$ is then distributed by introducing a local version $\boldsymbol{\theta}_i$ on each vehicle and adding the equality constraints as follows:

$$\boldsymbol{\theta}_i = \boldsymbol{\theta}_j\; \forall v_i \in \mathcal{V} \wedge\; v_j \in \mathcal{N}_i. \tag{8.17}$$

The stage cost function of Eq. 8.14 is reformulated into the following expression:

$$l_i(\boldsymbol{x}_i,\boldsymbol{u}_i,\boldsymbol{\theta}_i) = (\boldsymbol{\eta}_i - \boldsymbol{\theta}_i)^T\boldsymbol{P}(\boldsymbol{\eta}_i - \boldsymbol{\theta}_i) + \boldsymbol{\nu}_i^T\boldsymbol{W}\boldsymbol{\nu}_i + \boldsymbol{u}_i^T\boldsymbol{R}\boldsymbol{u}_i. \tag{8.18}$$

The Hessian of l_i is only positive-semidefinite, and thus the problem is underconstrained. There is no guarantee that the consensus point reaches a steady point unless additional pose constraints are applied, such as a stationary target or target area. The equality constraint of Eq. (8.17) is subsequently softened using Lagrangian relaxation and added to the objective function in the following section.

8.4.2 LOS-Constraint

The LOS constraints of Eq. (8.9) depends on the position error $\boldsymbol{e}_{j,i}$ and the normal vectors are parameterized in the attitude of the local vehicle,

$$\begin{aligned}
\boldsymbol{n}_{i,j}^{+}\boldsymbol{p}_j - \boldsymbol{n}_{i,j}^{+}\boldsymbol{p}_i &\leq 0,\\
\boldsymbol{n}_{i,j}^{-}\boldsymbol{p}_j - \boldsymbol{n}_{i,j}^{-}\boldsymbol{p}_i &\leq 0.
\end{aligned} \tag{8.19}$$

Together, the constraints can be reformulated on matrix form as follows:

$$\boldsymbol{A}_{i,j}\boldsymbol{x}_j - \boldsymbol{A}_{i,j}\boldsymbol{x}_i \leq 0, \tag{8.20}$$

such that the matrix $\boldsymbol{A}_{i,j}$ is parameterized in the attitude of vehicle i on the constraint related to vehicle j. Finally, since the constraint is now linear in the state, a local optimization problem can be formulated,

$$
\begin{aligned}
J_i\left(\boldsymbol{X}_i, \boldsymbol{U}_i, \boldsymbol{\Theta}_i\right) = \sum_{k=0}^{N} &\bigg[l(\boldsymbol{x}_{i,t+k|t}, \boldsymbol{u}_{i,t+k}) \\
&+ \sum_{j\in\mathcal{N}_i}[\boldsymbol{\lambda}_{j,it+k}^T \boldsymbol{A}_{j,i} - \boldsymbol{\lambda}_{i,j,t+k}^T \boldsymbol{A}_{i,j}]\boldsymbol{x}_{i,t+k|t} + \sum_{e\in\mathcal{E}_i} \boldsymbol{\mu}_{e,t+k}^T \boldsymbol{A}_e \boldsymbol{\theta}_{i,t+k}\bigg],
\end{aligned}
\tag{8.21}
$$

where $\boldsymbol{\lambda}_{j,i}$, and $\boldsymbol{\mu}_e$ are the Lagrangian multipliers associated with the LOS constraint from vehicle j to vehicle i and the consensus equality constraint associated with the edge e_{ij} respectively. $\boldsymbol{X}_i$ is the states of vehicle i over the time horizon, $\boldsymbol{X}_i = [\boldsymbol{x}_{i,t|t}, \boldsymbol{x}_{i,t+1|t}, \ldots, \boldsymbol{x}_{i,t+N-1|t}]$, $\boldsymbol{U}_i$ is the inputs over the time horizon $\boldsymbol{U}_i = [\boldsymbol{u}_{i,t}, \boldsymbol{u}_{i,t+1}, \ldots, \boldsymbol{u}_{i,t+N-1}]$ and $\boldsymbol{\Theta}_i$ is the locally computed consensus point across the time horizon, $\boldsymbol{\Theta}_i = [\boldsymbol{\theta}_{i,t}, \boldsymbol{\theta}_{i,t+1}, \ldots, \boldsymbol{\theta}_{i,t+N-1}]$. The control problem can now be reformulated as a local optimization problem as follows,

$$\underset{\boldsymbol{X}_i, \boldsymbol{U}_i, \boldsymbol{\Theta}_i}{\text{minimize}}\, J_i\left(\boldsymbol{X}_i, \boldsymbol{U}_i, \boldsymbol{\Theta}_i\right) \tag{8.22}$$

$$
\begin{aligned}
&\text{subject to,} \\
&\boldsymbol{u}_{i,t+k} \in \mathcal{U}_i, \\
&\boldsymbol{x}_{i,t+k+1|t} = \boldsymbol{f}_i(\boldsymbol{x}_{i,t+k|t}, \boldsymbol{u}_{i,t+k}).
\end{aligned}
\tag{8.23}
$$

The dual variables $\boldsymbol{\lambda}$ for the visual inequalities are updated using the projected sub-gradient method [21] as follows,

$$\boldsymbol{\lambda}_{i,j,t+k}^{r+1} = \boldsymbol{\lambda}_{i,j,t+k}^{r} + \kappa_{i,j}^r (\boldsymbol{A}_{i,j,t+k}[\boldsymbol{x}_{j,t+k|t}^{*r} - \boldsymbol{x}_{i,t+k|t}^{*r}])_+, \tag{8.24}$$

where $(\cdot)^*$ are the resulting optimal values from the solution to Eq. (8.22-8.23), $(\cdot)^r$ denotes the rth iteration, $(\cdot)_+$ is the projected gradient and $\boldsymbol{A}_{i,j,t+k}$ is the visual constraint matrix updated over the time horizon.

The dual variables $\boldsymbol{\mu}$ for the consensus equality constraints are likewise updated using the sub-gradient method [21].

$$\boldsymbol{\mu}_{e,t+k}^{r+1} = \boldsymbol{\mu}_{e,t+k}^{r} + \gamma_e^r (\boldsymbol{\theta}_{i,t+k}^{*r} - \boldsymbol{\theta}_{j,t+k}^{*r}), \tag{8.25}$$

where i and j are the nodes of the edge, such that,

$$i, j \in e. \tag{8.26}$$

The overall control algorithm is shown in Algorithm 1.

Algorithm 1 Distributed Controller

Input: $\boldsymbol{\lambda}^0$, $\boldsymbol{\mu}^0$

1: **for** $r = 0, \dots, L - 1$ **do**
2:     Solve local optimization problem Eq. (8.22) to obtain $\boldsymbol{X}_i^{*r}$, $\boldsymbol{U}_i^{*r}$ and $\boldsymbol{\Theta}_i^{*r}$
3:     Communicate the local state trajectories $\boldsymbol{X}_i^{*r}$ and consensus point sequence $\boldsymbol{\Theta}_i^{*r}$, to neighbors in $\mathcal{N}_i$.
4:     Compute the new price sequences $\boldsymbol{\lambda}^{r+1}$ and $\boldsymbol{\mu}^{r+1}$ locally by applying Eq. (8.24) and (8.25)
5: **end for**
6: Set $\boldsymbol{\lambda}^0 = \boldsymbol{\lambda}^L$ and $\boldsymbol{\mu}^0 = \boldsymbol{\mu}^L$
7: Apply first element of the control sequence $\boldsymbol{U}_i^{*L-1}$ to the local plant.

8.5 Simulations

In this section a simulation is conducted to show the application of the controller. The simulation is implemented in Python using CasADI [5]. The model of Eq. (8.7) is discretized using Runge-Kutta4. The applied optimization solver is the interior-point implementation IPOPT [231].

Parameter	Value	Unit
$\kappa_{i,j}$	30	$[-]$
γ_{ij}	2	$[-]$
$\boldsymbol{D}_i$	$diag(30, 30, 1)$	$[-]$
$\boldsymbol{M}_i$	$diag(10, 10, 1)$	$[-]$
$\|\boldsymbol{u}\|_\infty$	$[5, 5, 1.5]$	$[-]$
L	15	$[-]$
$\boldsymbol{x}_{1,0}$	$[4, 3, -0.2, 0, 0, 0]$	$[-]$
$\boldsymbol{x}_{2,0}$	$[1, -2, -0.58, 0, 0, 0]$	$[-]$
O_A	$[6.1, 3]$	$[m]$
d_{max}	3	$[m]$
$\boldsymbol{P}_i$	$diag(15, 15, 15)$	$[-]$
$\boldsymbol{W}_i$	$diag(10, 10, 10)$	$[-]$
$\boldsymbol{R}_i$	$diag(10, 10, 10)$	$[-]$
N	30	$[-]$
α_k	25	$[deg^\circ]$
δt	0.05	$[s]$

Table 8.1: Parameters and initial conditions used in the simulation scenario.

8.5.1 Monitoring and Rendezvous

The simulation scenario consists of two vehicles v_1, and v_2 and a stationary target O_A. Vehicle v_1 is inspecting target O_A, while at the same time rendezvous and docking with vehicle v_2. The inspecting vehicle is required to stay within a certain

distance of the target and maintain visual contact. Fig. 8.1 shows the scenario, where d_{max} is the maximum distance allowed between v_1 and O_A. The distance constraint is implemented as a quadratic constraint as follows:

$$(\boldsymbol{p}_{O_A} - \boldsymbol{p}_1)^T (\boldsymbol{p}_{O_A} - \boldsymbol{p}_1) \le d_{max}^2. \tag{8.27}$$

The location of the object $\boldsymbol{p}_{O_A}$ is stationary, and known. Thereby, the constraint (8.27) is simply an inequality constraint on vehicle one. Moreover, the visual constraint (8.10) is only from the vehicle to the object and requires no dual decomposition and communication between them.

Table 8.1 contains the dynamics parameters, initial conditions, and tuning parameters. Fig. 8.2 shows the bearing angles measured in the cameras. The bearings move towards the visual constraint limits and overshoots slightly. The overshoot is natural since the visual constraints are implemented using Lagrangian relaxation, and the number of iterations for updating the dual variables are limited. The overshoot is easily dealt with if one defines the limits lower than the actual camera field of view. Fig. 8.3 shows the trajectories of the vehicles. Vehicle v_1 shown in blue
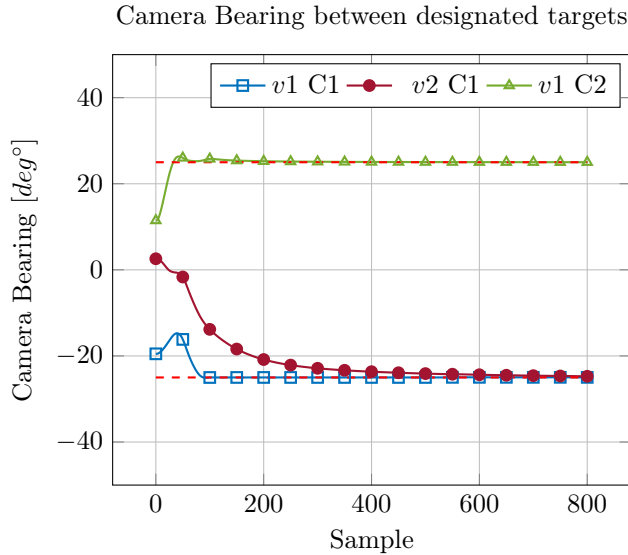
Figure 8.2: The figure shows bearing degrees in each of the cameras. The bearings of the cameras overshoots the limits slightly and thereby violates the constraint, however, in practice this could be avoided by defining a safety limit a couple of degrees inside the actual field-of-view

starts inside the designated target area looking at object O_A, while vehicle v_2 starts outside the area with v_1 inside the field-of-view. Note that the constraint of (8.27) imposes an implicit restriction on the pose of vehicle one. Hence the consensus point of (8.18) is attracted to the position of vehicle one. The constraint violation is a trade-off between both the tuning of the consensus and the number of iterations for the update of the dual variables and as such more iterations would allow a better
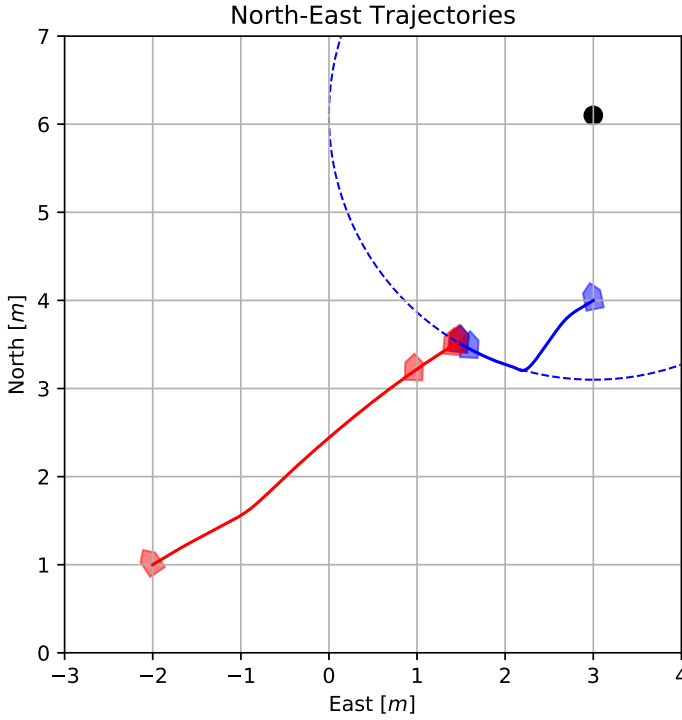
Figure 8.3: The trajectories show that each vehicle move towards each other while trying to maintain visual contact. Vehicle v_1 stays within the prescribed distance of the target while keeping both v_1 and O_A inside the respective camera field-of-view.

estimate of the actual dual variables. The subgradient method is converging at a sub-linear rate and thus to obtain accurate dual variables a large number of iterations are required [105, 109]. The communication requirement quickly increases as a result of the sharing of state trajectories and optimal consensus point sequences. One possible solution would be to allow second-order information to the update of the dual variables at the expense of slightly more data communication for each iteration. The second-order information would allow up to quadratic convergence of the dual variables and as such reduce the necessary iterations significantly [105, 109]. The bandwidth of underwater optical communication would allow for the increased communication requirement within a few tens of meters [243, 232]. The communication requirement for the specific simulation was approximately 1.7 Mbit/s. The bandwidth of acoustic communication range up to 0.5 Mbit/s at 60m [206], but the bandwidth can by manipulation of the sampling time δt, the max iteration L and the length of the control horizon N be significantly lowered.

8.6 Chapter Summary

In this chapter, we presented a distributed model predictive controller for the solution to a cooperative rendezvous and docking problem under visual camera constraints. The problem consisted of two subparts, namely a consensus problem and a visual field-of-view restriction. The DMPC was derived using dual decomposition. A simulation study was conducted to show the application of the controller, where two vehicles conduct are rendezvous and docking maneuver while one of the vehicles stay within a maximum prescribed distance of a designated target and maintain visual contact.

Chapter 9

Conclusions and Future Work

This chapter provides the overall conclusions of the work presented in previous chapters of this monograph. Further, the research conducted has revealed additional avenues of research interest, which will be summaries at the end of the chapter.

9.1   Conclusions

This thesis considered the modeling and control of modular underwater robots. The thesis was divided into two parts with each part treating a research question.

9.1.1   Conclusions of Part I: Modeling

The research question of Part I considered the change of behavior as a result of changing morphology. Specifically, the research question posed in Chapter 1 was:

Research Question 1: Is it feasible to automatically construct a descriptive model of a given morphology for a system composed of Modular Underwater Robots?

Part I of this thesis developed a modeling approach to mapping the behavior of a system comprised of arbitrarily rigidly interconnected underwater robots. Part I employed the Udwadia-Kalaba Formulation for constrained dynamics as a framework to model the modular underwater robotic system. The robotic models are based on Fossens robot-like formulation for marine vehicles and utilizes quaternions for attitude representation. The modular robots rigidly attach themselves to each other to form an aggregated systems with higher capabilities. The Udwadia-Kalaba formulation handles constraints on acceleration level. However, regular derivation of systems dynamics using generalized coordinates produces a singular mass matrix, due to the properties of the quaternion attitude representation. Employing quasi-coordinates for the dynamics of the system, and the derivation of the constraint formulation was shown to circumvent the problem of the singular mass matrix.

The multi-body dynamics model does not take into account advanced effects, such as, hydrodynamic hull to hull interaction effects. Therefore, the model requires rigorous testing before employing it for control design purposes. The thesis

has conducted two separate experimental test campaigns to evaluate the applicability of the multi-body approach to modeling the modular underwater robotics system. The first experimental campaign consisted of two tests and employed hulls with spherical geometry. The spherical geometry of the hulls ensured symmetry conditions which in turn allowed for uncoupled damping coefficients. The first experiment was a free-decay test actuated by the combined restoring forces of the interconnected system.

The resulting analysis compared the actual trajectory of the submerged system with the simulated paths. The comparison showed that the measured and simulated system aligned very well. Furthermore, the measured data were used to estimate the damping and restoring force vector of the vehicles. The estimated parameters were within expected range, which further validated the model approach. The second experiment of the first experimental campaign employed thrusters to actuate the system.

The resulting trajectories were qualitatively similar to the simulated results. However, due to a violation of assumptions the experiment could not validate the model.

The second experimental campaign increased the complexity of the subsystems from simple geometric hulls to a BlueROV vehicle. The dynamic parameters of the BlueROV were identified in elaborate towing tank tests.

The validation experiments consisted of two maneuvering trails. The first trial actuated both vehicles in the forward axis, thereby creating a straight trajectory. The comparison of the trajectories showed very similar results with the similar simulated paths.

The second trial actuated only one vehicle causing a rotational motion. The trajectories and the heading of the vehicles were very similar to the simulated counterparts.

The result of the rigorous testing was that the proposed automatic model approach to multi-body dynamics successfully captures the behavior of a modular underwater robotic system. In short, it was possible to construct a method to automatically model a system of MURs for a given morphology.

9.1.2   Conclusions of Part II: Docking Control

The topic of Part I treated the automatic modeling of morphologies. However, formation of the morphologies require individual MURs to physically connect. The generation of a morphology provided the foundation for research question two:

Research Question 2: Is it possible to conduct rendezvous and docking between multiple vehicles to form a morphology?

Part II of this thesis treated research question two by further introducing two additional problems related to morphology generation between the MURs. First, Chapter 7 assumed that camera-based navigation was employed. Secondly, the control problem naturally conformed to a distributed control problem, since the MUR system consisted of individual MURs working towards a common goal. Camera navigation imposes LOS constraints of the vehicle which must be deal with on a control level. Chapter 7 introduced the problem of rendezvous and docking for underwater vehicles, and presented literature relevant to the problem of docking for

vehicles with LOS constraints. Part II further employed Distributed Model Predictive Control by dual decomposition to solve the rendezvous and docking problem with LOS constraints.

Chapter 7 gave an overview of the MPC strategy, and the distributed form of the controller using dual decomposition. The control tools introduced in Chapter 7 was applied in Chapter 8 to solve research question two. The proposed solution utilize a DMPC strategy to ensure the LOS constraints between the cameras on each MUR. The DMPC treats the rendezvous and docking problem by introducing a consensus variable for the pose of the vehicles, and decomposes it with dual decomposition. The LOS constraints were applied as inequality constraints, directly in the MPC formulation, and subsequently decomposed using dual decomposition. Finally, the algorithm was shown to work in simulation between two MURs.

The novelty, and the contribution, of the proposed rendezvous and docking approach is the cooperative nature of the controller, which has not been investigated in prior literature.

In short, it was possible to conduct rendezvous and docking between multiple vehicles to form a morphology by utilizing a DMPC strategy combined with camera based navigation.

9.2   Future Work

Time is a limited resource, and many possible directions within the context of modular underwater robotics could not be pursued within the time frame of this project. The following is an overview of possible research directions required for a modular underwater robotic system.

Distributed Control: Once a morphology forms, the control of the combined system becomes the main concern. Every change in the morphology cause a change in the dynamics. Any controller depends on the understanding of the underlying dynamics, and the problem of controlling a system with changing behavior is central. However, the vision of seamless cooperative control for the system requires more research. Is it feasible to automate the design of control algorithms for any given morphology based on the automatic generated model of the system?

Latency Robust Control: Underwater communication is subject to high latency. High latency deteriorates control performance and possibly destabilize the system. Control under latency is a field of research that is highly relevant to cooperative underwater control.

Fault-Detection: The modular underwater robotics system contains a significant number of redundancies in sensors and actuators. The inherent redundancies of the modular underwater robotic system enables fault-tolerant reconfiguration such that the system can maintain performance under fault occurrences. The fault-detection and identification is, therefore, a highly appropriate topic to explore.

Morphological Change: Morphological changes to the system not only changes the dynamics, but also the measurement capabilities. Studying the consequence of morphological changes in the system could be interesting in the

context of situational awareness, where the location of sensors is a critical factor for successful perception.

References

[1]   Hottinger Baldwin Messtechnik GmbH (HBM). *Hottinger Baldwin Messtechnik GmbH (HBM)*. 2017.

[2]   Pedro Caldeira Abreu and Antonio M. Pascoal. "Formation control in the scope of the MORPH project. Part I: Theoretical foundations". In: *4th IFAC Workshop onNavigation, Guidance and Controlof Underwater VehiclesNGCUV 2015* 28.2 (2015), pp. 244–249.

[3]   Pedro Caldeira Abreu et al. "Formation Control in the scope of the MORPH project. Part II: Implementation and Results*". In: *IFAC4th IFAC Workshop onNavigation, Guidance and Controlof Underwater VehiclesNGCUV 2015* 48.2 (2015), pp. 250–255.

[4]   Ben Allen et al. "Autonomous Docking Demonstrations with Enhanced REMUS Technology". In: *OCEANS 2006*. IEEE, Sept. 2006, pp. 1–6.

[5]   Joel Andersson. "A General-Purpose Software Framework for Dynamic Optimization". PhD thesis. Arenberg Doctoral School, KU Leuven, 2013.

[6]   G. Antonelli, S Chiaverini, and N Sarkar. "External force control for underwater vehicle-manipulator systems". In: *IEEE Transactions on Robotics and Automation* 17.6 (2001), pp. 931–938.

[7]   Gianluca Antonelli, F Caccavale, and S Chiaverini. "A modular scheme for adaptive control of underwater vehicle-manipulator systems". In: *Proceedings of the 1999 American Control Conference (Cat. No. 99CH36251)* 5.June (1999), pp. 3008–3012.

[8]   Gianluca Antonelli and Elisabetta Cataldi. "Recursive adaptive control for an underwater vehicle carrying a manipulator". In: *2014 22nd Mediterranean Conference on Control and Automation, MED 2014* (2014), pp. 847–852.

[9]   Gianluca Antonelli and Stefano Chiaverini. "A fuzzy approach to redundancy resolution for underwater vehicle-manipulator systems". In: *Control Engineering Practice* 11.4 (2003), pp. 445–452.

[10] Gianluca Antonelli et al. "Tracking control for underwater vehicle-manipulator systems with velocity estimation". In: *IEEE Journal of Oceanic Engineering* 25.3 (2000), pp. 399–413.

[11]   Juan Julca Avila et al. "Experimental Investigation of the Hydrodynamic Coefficients of a Remotely Operated Vehicle Using a Planar Motion Mechanism". In: *Journal of Offshore Mechanics and Arctic Engineering* 134.2 (2012), p. 021601.

[12]   Juan Pablo Julca Avila and Julio Cezar Adamowski. "Experimental evaluation of the hydrodynamic coefficients of a ROV through Morison's equation". In: *Ocean Engineering* 38.17-18 (2011), pp. 2162–2170.

[13]   Juan Pablo Julca Avila et al. "Modeling and Identification of an Open-frame Underwater Vehicle: The Yaw Motion Dynamics". In: *Journal of Intelligent & Robotic Systems* 66.1-2 (Aug. 2011), pp. 37–56.

[14]   G. Baciu, J.C.K. Chou, and H.K. Kesavan. "Constrained multibody systems: graph-theoretic Newton-Euler formulation". In: *IEEE Transactions on Systems, Man, and Cybernetics* 20.5 (1990), pp. 1025–1048.

[15]   Arun K. Banerjee. "Comment on "Relationship Between Kane's Equations and the Gibbs-Appell Equations"". In: *Journal of Guidance Control and Dynamics* 10.6 (1987), pp. 596–597.

[16]   Nicolas Basalto et al. "Hausdorff clustering of financial time series". In: *Physica A: Statistical Mechanics and its Applications* 379.2 (2007), pp. 635–644. arXiv: 0504014 [physics].

[17]   Pedro Batista, Carlos Silvestre, and Paulo Oliveira. "A two-step control approach for docking of autonomous underwater vehicles". In: *International Journal of Robust and Nonlinear Control* 25.10 (July 2015), pp. 1528–1547.

[18]   Olivier a. Bauchau. *Flexible Multibody Dynamics*. Vol. 176. 2011, p. 749.

[19]   Olivier A Bauchau and André Laulusa. "Review of Contemporary Approaches for Constraint Enforcement in Multibody Systems". In: *Journal of Computational and Nonlinear Dynamics* 3.1 (2008), p. 011005.

[20]   Donald Berndt and James Clifford. "Using dynamic time warping to find patterns in time series". In: *Workshop on Knowledge Knowledge Discovery in Databases* 398 (1994), pp. 359–370.

[21]   Dimitri P Bertsekas. *Nonlinear programming*. 2nd. Athena Scientific, Sept. 2008.

[22]   Peter Betsch and Ralf Siebert. "Rigid body dynamics in terms of quaternions: Hamiltonian formulation and conserving numerical integration". In: *International Journal for Numerical Methods in Engineering* 79.4 (July 2009), pp. 444–473. arXiv: 1010.1724.

[23]   M Blanke, KP Lindegaard, and TI Fossen. "Dynamic model for thrust generation of marine propellers". In: *Manoeuvring and Control of Marine Craft 2000 (MCMC2000): 5th IFAC Conference on Manoeuvring and Control of Marine Craft* (2000).

[24]   Anthony M. Bloch, Jerrold E. Marsden, and Dmitry V. Zenkov. "Quasivelocities and symmetries in non-holonomic systems". In: *Dynamical Systems* 24.2 (2009), pp. 187–222.

[25] Marco Borri, Carlo Bottasso, and Paolo Mantegazza. "Equivalence of Kane's and Maggi's equations". In: *Meccanica* 25.4 (1990), pp. 272–274.

[26] Stephen Boyd et al. *Notes on Decomposition Methods*. 2007.

[27] David J. Braun and Michael Goldfarb. "Eliminating constraint drift in the numerical simulation of constrained dynamical systems". In: *Computer Methods in Applied Mechanics and Engineering* 198.37-40 (2009), pp. 3151–3160.

[28] Kathryn Eleda Brenan, S. L. Campbell, and Linda Ruth Petzold. *Numerical Solution of Initial-Value Problems in Differential-Algebraic Equations*. Society for Industrial and Applied Mathematics, Jan. 1995, p. 256.

[29] L. Brignone, M. Perrier, and C. Viala. "A fully autonomous docking strategy for Intervention AUVs". In: *OCEANS 2007 - Europe*. IEEE, June 2007, pp. 1–6.

[30] J.C Butcher. *Numerical Methods for Ordinary Differential Equations*. 2008.

[31] A.B. Byachkov and V.M. Suslonov. "MAGGI'S EQUATIONS IN TERMS OF QUASI-COORDINATES". In: *Regular and Chaotic Dynamics* 7.3 (2002), p. 269.

[32] M. Caccia, G. Indiveri, and G. Veruggio. "Modeling and identification of open-frame variable configuration unmanned underwater vehicles". In: *IEEE Journal of Oceanic Engineering* 25.2 (Apr. 2000), pp. 227–240.

[33] Giuseppe Casalino et al. "MARIS: A national project on marine robotics for interventions". In: *2014 22nd Mediterranean Conference on Control and Automation, MED 2014* (2014), pp. 864–869.

[34] Giuseppe Casalino et al. "Underwater Intervention Robotics: An Outline of the Italian National Project MARIS". In: *Marine Technology Society Journal* 50.4 (2016), pp. 98–107.

[35] Huiguo Chen, Yingmin Li, and Zheqian Wu. "Dynamic time warping distance method for similarity test of multipoint ground motion field". In: *Mathematical Problems in Engineering* 2010 (2010).

[36] Zhaomeng Cheng, Hai-Tao Zhang, and Ming-Can Fan. "Consensus and rendezvous predictive control for multi-agent systems with input constraints". In: *Proceedings of the 33rd Chinese Control Conference*. IEEE, July 2014, pp. 1438–1443.

[37] a Chouakria-Douzal and P Nagabhushan. "Improved fréchet distance for time series". In: *Data Science and Classification* (2006), pp. 13–20.

[38] David Johan Christensen et al. "Collective Modular Underwater Robotic System for Long-Term Autonomous Operation". In: *IEEE International Conference on Robotics and Automation (ICRA)*. Seattle, Washington: IEEE, 2015.

[39] Pierre Courrieu. "Fast Computation of Moore-Penrose Inverse Matrices". In: *Neural Information Processing - Letters and Reviews* 8.2 (2008), pp. 25–29. arXiv: 0804.4809.

[40] S. Cowen, S. Briest, and J. Dombrowski. "Underwater docking of autonomous undersea vehicles using optical terminal guidance". In: *Oceans '97. MTS/IEEE Conference Proceedings* 2 (1997).

[41] Nuno A. Cruz et al. "A lightweight docking station for a hovering AUV". In: *2017 IEEE Underwater Technology (UT)*. IEEE, 2017, pp. 1–7.

[42] G. De Novi et al. "A new approach for a Reconfigurable Autonomous Underwater Vehicle for Intervention". In: *2009 3rd Annual IEEE Systems Conference* (Mar. 2009), pp. 23–26.

[43] Edward Desloge. "Reply by Author to David A. Levinson and Arun K. Banerjee". In: *Journal of Guidance, Control, and Dynamics* 13.2 (1990), pp. 382–383.

[44] Edward A Desloge. "A comparison of Kane's equations of motion and the Gibbs–Appell equations of motion". In: *American Journal of Physics* 54.5 (May 1986), pp. 470–472.

[45] Edward A. Desloge. "Relationship Between Kane's Equations and the Gibbs-Appell Equations". In: *Journal of Guidance Control and Dynamics* 10.1 (1987), pp. 120–122.

[46] Paolo Augusto Di Lillo et al. "Advanced ROV Autonomy for Efficient Remote Control in the DexROV Project". In: *Marine Technology Society Journal* 50.4 (July 2016), pp. 67–80.

[47] Anne Driemel and Sariel Har-peled. "Jaywalking Your Dog : Computing the Fréchet". In: 42.5 (2013), pp. 1830–1866.

[48] Fredrik Dukan, Martin Ludvigsen, and Asgeir J. Sørensen. "Dynamic positioning system for a small size ROV with experimental results". In: *OCEANS 2011 IEEE - Spain* (2011).

[49] M. Dunbabin et al. "Data muling over underwater wireless sensor networks using an autonomous underwater vehicle". In: *Proceedings 2006 IEEE International Conference on Robotics and Automation, 2006. ICRA 2006.* May. IEEE, 2006, pp. 2091–2098.

[50] Matthew Dunbabin et al. "Experiments with Cooperative Control of Underwater Robots". In: *The International Journal of Robotics Research* 28.6 (June 2009), pp. 815–833.

[51] Robert Edyvean. "Consequences of Fouling on Shipping". In: *Biofouling* (2010), pp. 217–225.

[52] Ole A Eidsvik and Ingrid Schjølberg. "Determination of Hydrodynamic Parameters for Remotely Operated Vehicles". In: *Proceedings of the ASME 2016 35th International Conference on Ocean, Offshore and Arctic Engineering*. Busan: ASME, 2016, pp. 1–10.

[53] YH Eng et al. "Identification of the Hydrodynamics Coefficients of an Underwater Vehicle using Free Decay Pendulum Motion". In: *Engineering Letters* 16.3 (2008), pp. 326–331.

[54] J.C. Evans et al. "Docking techniques and evaluation trials of the SWIM-MER AUV: an autonomous deployment AUV for work-class ROVs". In: *MTS/IEEE Oceans 2001. An Ocean Odyssey. Conference Proceedings (IEEE Cat. No.01CH37295)* 1 (2001), pp. 520–528.

[55] J. Evans et al. "Autonomous docking for Intervention-AUVs using sonar and video-based real-time 3D pose estimation". In: *Oceans 2003. Celebrating the Past ... Teaming Toward the Future (IEEE Cat. No.03CH37492)*. Vol. 4. IEEE, 2003, 2201–2210 Vol.4.

[56] Shuangshuang Fan et al. "Motion control of docking AUV in currents". In: *OCEANS 2015 - Genova*. IEEE, May 2015, pp. 1–7.

[57] Jay A. Farrell. *Aided Navigation: GPS with High Rate Sensors*. 1st ed. New York, New York, USA: McGraw-Hill, Inc., 2008.

[58] M.D. Feezor et al. "Autonomous underwater vehicle homing/docking via electromagnetic guidance". In: *IEEE Journal of Oceanic Engineering* 26.4 (2001), pp. 515–521.

[59] G. Ferrari-Trecate et al. "Model Predictive Control Schemes for Consensus in Multi-Agent Systems with Single- and Double-Integrator Dynamics". In: *IEEE Transactions on Automatic Control* 54.11 (Nov. 2009), pp. 2560–2572.

[60] Andreas Fink et al. *Studies in Classification, Data Analysis, and Knowledge Organization*. 2010, pp. 229–239.

[61] Thor I Fossen. *Handbook of Marine Craft Hydrodynamics and Motion Control*. 1st. Trondheim: Wiley and son, 2011.

[62] Tak Chung Fu. "A review on time series data mining". In: *Engineering Applications of Artificial Intelligence* 24.1 (2011), pp. 164–181.

[63] Lidia Furno, Mikkel Cornelius Nielsen, and Mogens Blanke. "Centralised versus decentralised control reconfiguration for collaborating underwater robots". In: *9th IFAC Symposium on Fault Detection, Supervision and Safety for Technical Processes SAFEPROCESS 2015*. Vol. 48. 21. Elsevier Ltd., 2015, pp. 732–739.

[64] Lidia Furno et al. "Self-reconfiguration of modular underwater robots using an energy heuristic". In: *IEEE International Conference on Intelligent Robots and Systems* 2017-Septe (2017), pp. 6277–6284.

[65] Jeremi Gancet et al. "Dexrov: Dexterous undersea inspection and maintenance in presence of communication latencies". In: *4th IFAC Workshop on Navigation, Guidance and Control of Underwater Vehicles NGCUV 2015* 28.2 (2015), pp. 218–223. arXiv: 9605103 [cs].

[66] Jeremi Gancet et al. "Dexterous Undersea Interventions with Far Distance Onshore Supervision: the DexROV Project". In: *10th IFAC Conference on Control Applications in Marine Systems CAMS 2016* 49.23 (2016), pp. 414–419.

[67] Javier García de Jalón, Alfonso Callejo, and Andrés F Hidalgo. "Efficient Solution of Maggi's Equations". In: *Journal of Computational and Nonlinear Dynamics* 7.2 (2012), p. 021003.

[68] Carlos E. García, David M. Prett, and Manfred Morari. "Model predictive control: Theory and practice-A survey". In: *Automatica* 25.3 (1989), pp. 335–348.

[69] Carl Friedrich Gauß. "Über ein neues allgemeines Grundgesetz der Mechanik." In: *Journal für die reine und angewandte Mathematik (Crelles Journal)* 1829.4 (Jan. 1829), pp. 232–235.

[70] C. W. Gear. "Differential Algebraic Equations, Indices, and Integral Algebraic Equations". In: *SIAM Journal on Numerical Analysis* 27.6 (Dec. 1990), pp. 1527–1534.

[71] C. W. Gear and L. R. Petzold. "ODE Methods for the Solution of Differential/Algebraic Systems". In: *SIAM Journal on Numerical Analysis* 21.4 (Aug. 1984), pp. 716–728.

[72] Pontus Giselsson and Anders Rantzer. "Distributed Model Predictive Control with suboptimality and stability guarantees". In: *49th IEEE Conference on Decision and Control (CDC)*. 0. IEEE, Dec. 2010, pp. 7272–7277.

[73] Colin Goodall. "Procrustes Methods in the Statistical Analysis of Shape". In: *Journal of the Royal Statistical Society* 53.2 (1991), pp. 285–339.

[74] Alexandra Grancharova and Tor A. Johansen. "Distributed quasi-nonlinear model predictive control by dual decomposition". In: *Proceedings of the 18th World Congress*. Vol. 18. PART 1. IFAC, 2011, pp. 1429–1434.

[75] Svein Gundersen et al. *Subsea Facilities -Technology Developments, Incidents and Future Trends*. Tech. rep. Høvik: DNV GL Oil & Gas, 2014, p. 80.

[76] Georg Hamel. "Die Lagrange-Eulerschen Gleichungen der Mechanik". In: *Zeitschrift Für Mathematik und Physik* 50.1 (1904), pp. 1–57.

[77] Nicholas Hansen et al. "Short-range sensor for underwater robot navigation using line-lasers and vision". In: *10th IFAC Conference on Manoeuvring and Control of Marine Craft MCMC 2015*. Vol. 28. 16. Elsevier B.V., 2015, pp. 113–120.

[78] Eirik Hexeberg Henriksen, Ingrid Schjølberg, and Tor Berge Gjersvik. "Adaptable Joystick Control System for Underwater Remotely Operated Vehicles". In: *10th IFAC Conference on Control Applications in Marine Systems CAMS 2016* 49.23 (2016), pp. 167–172.

[79] Eirik Hexeberg Henriksen, Ingrid Schjølberg, and Tor Berge Gjersvik. "The UnderWater modular open robot simulation engine". In: *Autonomous Underwater Vehicles 2016, AUV 2016* (2016), pp. 261–267.

[80] Hans D. Höhne et al. "On Temporal Alignment of Sentences of Natural and Synthetic Speech". In: *IEEE Transactions on Acoustics, Speech, and Signal Processing* 31.4 (1983), pp. 807–813.

[81] Ronald L. Huston. "Comment on "Relationship Between Kane's Equations and the Gibbs-Appell Equations"". In: *Journal of Guidance Control and Dynamics* 11.2 (1988), pp. 191–191.

[82] R.G. Hutchins and J.P.C. Roque. "Filtering and control of an autonomous underwater vehicle for both target intercept and docking". In: *Proceedings of International Conference on Control Applications* (1995), pp. 1162–1163.

[83] A. V. Inzartsev, A. M. Pavin, and N. I. Rylov. "Development of the AUV automatic docking methods based on echosounder and video data". In: *2017 24th Saint Petersburg International Conference on Integrated Navigation Systems (ICINS)*. IEEE, May 2017, pp. 1–6.

[84] A.V. Inzartsev et al. "Investigation of Autonomous Docking System Elements for Long Term AUV". In: *Proceedings of OCEANS 2005 MTS/IEEE*. Vol. 2005. IEEE, 2005, pp. 1–6.

[85] ITTC. *ITTC – Recommended Procedures and Guidelines - Resistance test. 7.5-02-02-01 (Revision 03)*. Tech. rep. 2011, p. 13.

[86] Pakpong Jantapremjit and Philip A. Wilson. "Optimal Control and Guidance for Homing and Docking Tasks using an Autonomous Underwater Vehicle". In: *IEEE International Conference on Intelligent Robots and Systems*. 2007, pp. 3672–3677.

[87] Elżbieta Jarz-bowska. "Quasi-coordinates based dynamics modeling and control design for nonholonomic systems". In: *Nonlinear Analysis: Theory, Methods & Applications* 71.12 (2009), e118–e131.

[88] Young Seon Jeong, Myong K. Jeong, and Olufemi A. Omitaomu. "Weighted dynamic time warping for time series classification". In: *Pattern Recognition* 44.9 (2011), pp. 2231–2240.

[89] Jian Gao, Changxin Liu, and Yingxiang Wang. "Backstepping adaptive docking control for a full-actuated autonomous underwater vehicle with onboard USBL system". In: *2014 Oceans - St. John's*. 51279164. IEEE, Sept. 2014, pp. 1–6.

[90] G Jones. "The battle against marine biofouling: a historical review". In: *Advances in Marine Antifouling Coatings and Technologies*. Ed. by Claire Hellio and Diego Yebra. Elsevier, 2009, pp. 19–45.

[91] R. E. Kalaba and Firdaus E. Udwadia. "Lagrangian mechanics, Gauss's principle, quadratic programming, and generalized inverses: new equations for nonholonomically constrained discrete mechanical systems". In: *Quarterly of Applied Mathematics* 52.2 (1994), pp. 229–241.

[92] J. Kalwa et al. *The European R&D-project MORPH: Marine robotic systems of self-organizing, logically linked physical nodes*. Vol. 9. PART 1. IFAC, 2012, pp. 226–231.

[93] Joerg Kalwa et al. "The European Project MORPH: Distributed UUV Systems for Multimodal, 3D Underwater Surveys". In: *Marine Technology Society Journal* 50.4 (July 2016), pp. 26–41.

[94] J Kalwa et al. "The MORPH concept and its application in marine research". In: *2013 MTS/IEEE OCEANS - Bergen*. IEEE, June 2013, pp. 1–8.

[95] T R Kane. "Dynamics of Nonholonomic Systems". In: *Journal of Applied Mechanics* 28.4 (1961), pp. 574–578.

[96] T. R. Kane and C. F. Wang. "On the Derivation of Equations of Motion". In: *Journal of the Society for Industrial and Applied Mathematics* 13.2 (1965), pp. 487–492.

[97] N. Kato and M. Endo. "Guidance and Control of Unmanned, Untethered Submersible for Rendezvous and Docking with Underwater Station". In: *Proceedings OCEANS* 3.2 (1989).

[98] T. Kawasaki et al. ""Marine Bird", a new experimental AUV - results of docking and electric power supply tests in sea trials". In: *Oceans '04 MTS/IEEE Techno-Ocean '04 (IEEE Cat. No.04CH37600)*. Vol. 3. IEEE, 2004, pp. 1738–1744.

[99] E. Kelasidi, K. Y. Pettersen, and J. T. Gravdahl. "Modeling of underwater snake robots moving in a vertical plane in 3D". In: *IEEE International Conference on Intelligent Robots and Systems* Iros (2014), pp. 266–273.

[100] E Kelasidi et al. "Modeling of underwater snake robots". In: *2014 IEEE International Conference on Robotics and Automation (ICRA)*. IEEE, May 2014, pp. 4540–4547.

[101] Eamonn J. Keogh and Michael J. Pazzani. "Scaling up dynamic time warping for datamining applications". In: *Proceedings of the sixth ACM SIGKDD international conference on Knowledge discovery and data mining - KDD '00* (2000), pp. 285–289.

[102] Tamás Keviczky and Karl Henrik Johansson. "A Study On Distributed Model Predictive Consensus". In: *Proceedings of the 17th World Congress*. Vol. 41. 2. IFAC, 2008, pp. 1516–1521. arXiv: 0802.4450.

[103] Peter W. Kimball et al. "The ARTEMIS under-ice AUV docking system". In: *Journal of Field Robotics* 35.2 (Mar. 2018), pp. 299–308.

[104] P. King et al. "CATCHY an AUV ice dock". In: *OCEANS 2009, MTS/IEEE Biloxi - Marine Technology for Our Future: Global and Local Challenges* (2009).

[105] Emil Klintberg and Sebastien Gros. "A primal-dual Newton method for distributed Quadratic Programming". In: *53rd IEEE Conference on Decision and Control*. IEEE, Dec. 2014, pp. 5843–5848.

[106] A. M. Kohl et al. "A control-oriented model of underwater snake robots exposed to currents". In: *2015 IEEE Conference on Control Applications (CCA)*. IEEE, Sept. 2015, pp. 1585–1592.

[107] Hayato Kondo et al. "Passive acoustic and optical guidance for underwater vehicles". In: *Program Book - OCEANS 2012 MTS/IEEE Yeosu: The Living Ocean and Coast - Diversity of Resources and Sustainable Activities* (2012).

[108] Attila Kozma, Janick V Frasch, and Moritz Diehl. "A distributed method for convex quadratic programming problems arising in optimal control of distributed systems". In: *52nd IEEE Conference on Decision and Control*. IEEE, Dec. 2013, pp. 1526–1531.

[109] Attila Kozma et al. "An improved distributed dual newton-CG method for convex quadratic programming problems". In: *Proceedings of the American Control Conference* (2014), pp. 2324–2329.

[110] Szymon Krupinski et al. "Investigation of autonomous docking strategies for robotic operation on intervention panels". In: *OCEANS 2008*. IEEE, 2008, pp. 1–10.

[111] Jack Kuipers. *Quaternions and rotation sequences: a primer with applications to orbits, aerospace, and virtual reality*. 1st ed. Vol. 37. 01. Princeton University Press, 1999, p. 371.

[112] a Kurdila, J G Papastavridis, and M P Kamat. "Role of Maggi's equations in computational methods for constrained multibody systems". In: *Journal of Guidance, Control, and Dynamics* 13.1 (1990), pp. 113–120.

[113] Kyungmin Kwak et al. "Manta ROV docking sequence using 3-D Omnidirectional antenna's signal attenuation". In: *2017 14th International Conference on Ubiquitous Robots and Ambient Intelligence (URAI)*. IEEE, June 2017, pp. 858–859.

[114] J.C. Lambiotte et al. "Results from mechanical docking tests of a Morpheus class AUV with a dock designed for an OEX class AUV". In: *Oceans '02 Mts/Ieee* 1 (2002), pp. 260–265.

[115] Cornelius Lanczos. *The Variational Principles of Mechanics*. 4th. Dover Publications, 1970, p. 418.

[116] David M. Lane et al. "Persistent autonomy: the challenges of the PANDORA project". In: *9th IFAC Conference on Manoeuvring and Control of Marine Craft*. Vol. 45. 27. IFAC, 2012, pp. 268–273.

[117] André Laulusa and Olivier A Bauchau. "Review of Classical Approaches for Constraint Enforcement in Multibody Systems". In: *Journal of Computational and Nonlinear Dynamics* 3.1 (2008), p. 011004.

[118] Pan-Mook Lee Pan-Mook Lee, Bong-Hwan Jeon Bong-Hwan Jeon, and Sea-Moon Kim Sea-Moon Kim. "Visual servoing for underwater docking of an autonomous underwater vehicle with one camera". In: *Oceans 2003. Celebrating the Past ... Teaming Toward the Future (IEEE Cat. No.03CH37492)* 2 (2003), pp. 677–682.

[119] David a Levinson. "Relationship Between Kane's Equations and the Gibbs-Appell Equations - Comment". In: *Journal of Guidance Control and Dynamics* 10.6 (1987), pp. 593–593.

[120] Dejun Li, Tao Zhang, and Canjun Yang. "Terminal Underwater Docking of an Autonomous Underwater Vehicle Using One Camera and One Light". In: *Marine Technology Society Journal* 50.6 (Nov. 2016), pp. 58–68.

[121] Peng Li and Zheng H. Zhu. "Line-of-sight nonlinear model predictive control for autonomous rendezvous in elliptical orbit". In: *Aerospace Science and Technology* 69 (2017), pp. 236–243.

[122] Yong Li et al. "Dipolar field based 3-dimensional homing guidance algorithm for autonomous underwater vehicles". In: *2016 IEEE Chinese Guidance, Navigation and Control Conference (CGNCC)*. IEEE, Aug. 2016, pp. 1126–1131.

[123] Pal Liljeback and Richard Mills. "Eelume: A flexible and subsea resident IMR vehicle". In: *OCEANS 2017 - Aberdeen*. IEEE, June 2017, pp. 1–4.

[124] Khin Nwe Lwin et al. "Autonomous docking experiment in the sea for visual-servo type undeater vehicle using three-dimensional marker and dual-eyes cameras". In: *2016 55th Annual Conference of the Society of Instrument and Control Engineers of Japan (SICE)*. IEEE, Sept. 2016, pp. 1359–1365.

[125] Gian Antonio Maggi. *Principii della Teoria Matematica del Movimento dei Corpi: Corso di Meccanica Razionale*. 1st ed. Milano: Ulrico Hoepli, 1896, p. 522.

[126] Frederic Maire et al. "A Vision Based Target Detection System for Docking of an Autonomous Underwater Vehicle". In: *Proceedings of the 2009 Australasian Conference on Robotics and Automati on*. December. 2009, p. 7.

[127] Toshihiro Maki et al. "Docking method for hovering type AUVs by acoustic and visual positioning". In: *Proceedings of Underwater Technology Symposium*. 2013.

[128] Spyros Maniatopoulos, Dimitra Panagou, and Kostas J Kyriakopoulos. "Model Predictive Control for the navigation of a nonholonomic vehicle with field-of-view constraints". In: *2013 American Control Conference*. IEEE, June 2013, pp. 3967–3972.

[129] DB Marco, Alfredo Martins, and AJ Healy. "Surge motion parameter identification for the NPS Phoenix AUV". In: *1st Int. Workshop on Autonomous Underwater Vehicles for Shallow Water and Coastal Environment*. Lafayette, IN: IARP, 1998, pp. 197–210.

[130] Alfredo Martins et al. "Autonomous Surface Vehicle Docking Manoeuvre with Visual Information". In: *Proceedings 2007 IEEE International Conference on Robotics and Automation*. April. IEEE, Apr. 2007, pp. 4994–4999.

[131] Francesco Maurelli et al. "The PANDORA project: A success story in AUV autonomy". In: *OCEANS 2016 - Shanghai* (2016).

[132] Robert S. McEwen et al. "Docking Control System for a 54-cm-Diameter (21-in) AUV". In: *IEEE Journal of Oceanic Engineering* 33.4 (Oct. 2008), pp. 550–562.

[133] Volker Mehrmann. "Index Concepts for Differential-Algebraic Equations". In: *Encyclopedia of Applied and Computational Mathematics*. 1. Berlin, Heidelberg: Springer Berlin Heidelberg, 2015, pp. 676–681. arXiv: 1209.1711.

[134] Stefano Mintchev et al. "An underwater reconfigurable robot with bioinspired electric sense". In: *2012 IEEE International Conference on Robotics and Automation*. IEEE, May 2012, pp. 1149–1154.

[135] Stefano Mintchev et al. "Towards docking for small scale underwater robots". In: *Autonomous Robots* 38.3 (Mar. 2015), pp. 283–299.

[136] Richard Moeckel and Brad Murray. "Measuring the distance between time series". In: *Physica D: Nonlinear Phenomena* 102.3-4 (1997), pp. 187–194.

[137] Nader Mohamed et al. "Monitoring underwater pipelines using sensor networks". In: *Proceedings - 2010 12th IEEE International Conference on High Performance Computing and Communications, HPCC 2010* (2010), pp. 346–353.

[138] Lindasalwa Muda, Mumtaj Begam, and I. Elamvazuthi. "Voice Recognition Algorithms using Mel Frequency Cepstral Coefficient (MFCC) and Dynamic Time Warping (DTW) Techniques". In: *Journal of Computing* 2.3 (2010), pp. 138–143. arXiv: 1003.4083.

[139] Meinard Müller. "Dynamic Time Warping". In: *Information Retrieval for Music and Motion*. Berlin, Heidelberg: Springer Berlin Heidelberg, 2007, pp. 69–84.

[140] Cory S. Myers and Lawrence R. Rabiner. "A Level Building Dynamic Time Warping Algorithm for Connected Word Recognition". In: *IEEE Transactions on Acoustics, Speech, and Signal Processing* 29.2 (1981), pp. 284–297.

[141] Myo Myint et al. "Dual-eyes Vision-based Docking System for Autonomous Underwater Vehicle: an Approach and Experiments". In: *Journal of Intelligent & Robotic Systems* (Oct. 2017).

[142] Sathish Natarajan and Rajagopalan Srinivasan. "Multi-model based process condition monitoring of offshore oil and gas production process". In: *Chemical Engineering Research and Design* 88.5-6 (2010), pp. 572–591.

[143] Ghazi Al-naymat. "SparseDTW: A Novel Approach to Speed up Dynamic Time Warping". In: 2007 (2009), pp. 117–127. arXiv: arXiv:1201.2969v1.

[144] Mikkel Cornelius Nielsen, Mogens Blanke, and Ingrid Schjølberg. "Efficient Modelling Methodology for Reconfigurable Underwater Robots". In: *10th IFAC Conference on Control Applications in Marine Systems CAMS 2016*. Vol. 49. 23. Elsevier B.V., 2016, pp. 74–80.

[145] Mikkel Cornelius Nielsen, Tor Arne Johansen, and Mogens Blanke. "Cooperative Rendezvous and Docking for Underwater Robots using Model Predictive Control and Dual Decomposition". In: *2018 European Control Conference (ECC)*. Limassol, Cyprus: IEEE, 2018, p. 6.

[146] Mikkel Cornelius Nielsen et al. "Constrained multi-body dynamics for modular underwater robots — Theory and experiments". In: *Ocean Engineering* 149.February 2018 (2018), pp. 358–372.

[147] Mikkel Cornelius Nielsen et al. "Experimental Validation of Dynamic Multi-Body Modelling for Reconfigurable Underwater Robots". In: *Oceans 2016 MTS/IEEE*. 2016, p. 6.

[148] Parviz E Nikravesh. "Some Methods for Dynamic Analysis of Constrained Mechanical Systems: A Survey". In: *Computer Aided Analysis and Optimization of Mechanical System Dynamics*. Berlin, Heidelberg: Springer Berlin Heidelberg, 1984, pp. 351–368.

[149] N. M. Nouri, K. Mostafapour, and R. Bahadori. "An apparatus to estimate the hydrodynamic coefficients of autonomous underwater vehicles using water tunnel testing". In: *Review of Scientific Instruments* 87.6 (2016), p. 065106.

[150] M.H. Oh and J.H. Oh. "Homing and Docking Control of AUV Using Model Predictive Control". In: *The Proceedings of the Fifth ISCPE Pacific/Asia Offshore Mechanics Symposium, Daejean, Korea* (2002), pp. 130–142.

[151] Reza Olfati-Saber, J. Alex Fax, and Richard M. Murray. "Consensus and cooperation in networked multi-agent systems". In: *Proceedings of the IEEE* 95.1 (2007), pp. 215–233. arXiv: 1009.6050.

[152] N Palomeras and JC García. "A distributed architecture for enabling autonomous underwater intervention missions". In: *4th Annual IEEE International System Conference* (2010), pp. 159–164.

[153] Narcís Palomeras et al. "I-AUV Docking and Panel Intervention at Sea". In: *Sensors* 16.10 (Oct. 2016), p. 1673.

[154] Narcís Palomeras et al. "Toward persistent autonomous intervention in a subsea panel". In: *Autonomous Robots* 40.7 (2016), pp. 1279–1306.

[155] Pan-Mook Lee, Bong-Hwan Jeon, and Chong-Moo Lee. "A docking and control system for an autonomous underwater vehicle". In: *Oceans '02 MTS/IEEE*. IEEE, 2002, pp. 1609–1614.

[156] Dimitra Panagou and Kostas J. Kyriakopoulos. "Control of underactuated systems with viability constraints". In: *Proceedings of the IEEE Conference on Decision and Control* 1 (2011), pp. 5497–5502.

[157] Dimitra Panagou and Kostas J. Kyriakopoulos. "Dynamic positioning for an underactuated marine vehicle using hybrid control". In: *International Journal of Control* 87.2 (Feb. 2014), pp. 264–280.

[158] Dimitra Panagou, Spyros Maniatopoulos, and Kostas J. Kyriakopoulos. "Control of an Underactuated Underwater Vehicle in 3D Space under Field-of-View Constraints". In: *3rd IFAC Workshop on Navigation, Guidance and Control of Underwater Vehicles* 45.5 (2012), pp. 25–30.

[159] J G Papastavridis. *ANALYTICAL MECHANICS*. World Scientific Publishing Co Pte. Ltd, 2014, p. 1416.

[160] JOHN G. PAPASTAVRIDIS. "Maggi's equations of motion and the determination of constraint reactions". In: *Journal of Guidance, Control, and Dynamics* 13.2 (Mar. 1990), pp. 213–220.

[161] John G. Papastavridis. "On the nonlinear Appell's equations and the determination of generalized reaction forces". In: *International Journal of Engineering Science* 26.6 (1988), pp. 609–625.

[162] Sankara Papavinasam. *The Oil and Gas Industry*. 2014, pp. 1–39.

[163] Hyeongjun Park, Stefano Di Cairano, and Ilya Kolmanovsky. "Model Predictive Control for Spacecraft Rendezvous and Docking with a Rotating / Tumbling Platform and for Debris Avoidance". In: *American Control Conference* (2011), pp. 1922–1927.

[164] Hyeongjun Park, Stefano Di Cairano, and Ilya Kolmanovsky. "Model Predictive Control of spacecraft docking with a non-rotating platform". In: *Proceedings of the 18th World Congress*. Vol. 18. PART 1. IFAC, 2011, pp. 8485–8490.

[165] Hyeongjun Park et al. "Analysis and Experimentation of Model Predictive Control for Spacecraft Rendezvous and Proximity Operations with Multiple Obstacle Avoidance". In: *AIAA/AAS Astrodynamics Specialist Conference* September (2016), pp. 1–17.

[166] Jin-Yeong Park Jin-Yeong Park et al. "Experiment on Underwater Docking of an Autonomous Underwater Vehicle 'ISiMI' using Optical Terminal Guidance". In: *OCEANS 2007 - Europe* (2007).

[167] Jin-Yeong Park et al. "Experiments on vision guided docking of an autonomous underwater vehicle using one camera". In: *Ocean Engineering* 36.1 (Jan. 2009), pp. 48–61.

[168] R. Penrose. "A generalized inverse for matrices". In: *Mathematical Proceedings of the Cambridge Philosophical Society* 51.3 (1955), pp. 406–413.

[169] M. Pereira and C. Ankjaergaard. "Legislation affecting antifouling products". In: *Advances in Marine Antifouling Coatings and Technologies*. Elsevier, 2009. Chap. 10, pp. 240–259.

[170] Pedro R. Peres-Neto and Donald A. Jackson. "How well do multivariate data sets match? The advantages of a procrustean superimposition approach over the Mantel test". In: *Oecologia* 129.2 (2001), pp. 169–178.

[171] François Petitjean, Alain Ketterlin, and Pierre Gançarski. "A global averaging method for dynamic time warping, with applications to clustering". In: *Pattern Recognition* 44.3 (2011), pp. 678–693.

[172] Francois Petitjean et al. "Dynamic Time Warping Averaging of Time Series Allows Faster and More Accurate Classification". In: *Proceedings - IEEE International Conference on Data Mining, ICDM* 2015-Janua.January (2015), pp. 470–479.

[173] J.-C. Piedboeuf. "Kane's equations or Jourdain's principle?" In: *Proceedings of 36th Midwest Symposium on Circuits and Systems*. 7. IEEE, 1993, pp. 1471–1474.

[174] Luca Pivano, Thor Inge Fossen, and Tor Arne Johansen. "Nonlinear Model Identification of a Marine Propeller Over Four-Quadrant Operations". In: *IFAC Proceedings Volumes* 39.1 (2006), pp. 315–320.

[175] Mario Prats and J Pérez. "An open source tool for simulation and supervision of underwater intervention missions". In: *Intelligent Robots and . . .* (2012).

[176] Mario Prats et al. "Reconfigurable AUV for intervention missions: A case study on underwater object recovery". In: *Intelligent Service Robotics* 5.1 (2012), pp. 19–31.

[177]   Mario Prats et al. "Reconfigurable AUV for intervention missions: a case study on underwater object recovery". In: *Intelligent Service Robotics* 5.1 (Oct. 2011), pp. 19–31.

[178]   *Price of inspection of corrosion in Denmark.*

[179]   Dave Pyle et al. "Leveraging a large UUV platform with a docking station to enable forward basing and persistence for light weight AUVs". In: *OCEANS 2012 MTS/IEEE: Harnessing the Power of the Ocean* (2012).

[180]   S. Joe Qin and Thomas A. Badgwell. "An Overview of Nonlinear Model Predictive Control Applications". In: *Nonlinear Model Predictive Control* 26 (2000), pp. 369–392. arXiv: `arXiv:1011.1669v3`.

[181]   SJ Joe Qin et al. "A survey of industrial model predictive control technology". In: *Control Engineering Practice* 11 (2003), pp. 733–764. arXiv: `arXiv:1402.6991v1`.

[182]   Morgan Quigley et al. "ROS: an open-source Robot Operating System". In: *ICRA* 3.Figure 1 (2009), p. 5.

[183]   L. Rabiner, A. Rosenberg, and S. Levinson. "Considerations in dynamic time warping algorithms for discrete word recognition". In: *IEEE Transactions on Acoustics, Speech, and Signal Processing* 26.6 (Dec. 1978), pp. 575–582.

[184]   G.J.S. Rae and S.M. Smith. "A Fuzzy Rule Based Docking Procedure For Autonomous Underwater Vehicles". In: *OCEANS 92 Proceedings@m_ Mastering the Oceans Through Technology* 2 (1992), pp. 539–546.

[185]   Anders Rantzer. "Dynamic dual decomposition for distributed control". In: *Proceedings of the American Control Conference* (2009), pp. 884–888.

[186]   Chotirat Ann Ratanamahatana and Eamonn Keogh. "Three Myths about Dynamic Time Warping Data Mining". In: *Proceedings of the 2005 SIAM International Conference on Data Mining.* 2005, pp. 506–510.

[187]   T.M. Rath and R. Manmatha. "Word image matching using dynamic time warping". In: *2003 IEEE Computer Society Conference on Computer Vision and Pattern Recognition, 2003. Proceedings.* 2 (2003), pp. II–521–II–527.

[188]   P. Ridao et al. "On the identification of non-linear models of unmanned underwater vehicles". In: *Control Engineering Practice* 12.12 SPEC. ISS. (Dec. 2004), pp. 1483–1499.

[189]   Dan E. Rosenthal. "Comment on "Relationship Between Kane's Equations and the Gibbs-Appell Equations"". In: *Journal of Guidance Control and Dynamics* 10.6 (1987), pp. 595–596.

[190]   Andrew Ross, Thor I Fossen, and Tor Arne Johansen. "Identification of underwater vehicle hydrodynamic coefficients using free decay tests". In: *IFAC Conference on Control Applications in Marine Systems.* 2004, pp. 363–368.

[191]   Hiroaki Sakoe and Seibi Chiba. "Dynamic Programming Algorithm Optimization for Spoken Word Recognition". In: *IEEE Transactions on Acoustics, Speech, and Signal Processing* 26.1 (1978), pp. 43–49. arXiv: `arXiv:1011.1669v3`.

[192]   Stan Salvador and Philip Chan. "FastDTW : Toward Accurate Dynamic Time Warping in Linear Time and Space". In: *Intelligent Data Analysis* 11 (2007), pp. 561–580.

[193]   Albert Sans-Muntadas et al. "Navigation and probability assessment for successful AUV docking using USBL". In: *10th IFAC Conference on Manoeuvring and Control of Marine Craft MCMC 2015*. Ed. by Roberto Galeazzi and Mogens Blanke. Vol. 28. 16. Copenhagen, Denmark: International Federation of Automatic Control, 2015, pp. 204–209.

[194]   Mohan Santhakumar and Jinwhan Kim. "Modelling, simulation and model reference adaptive control of autonomous underwater vehicle-manipulator systems". In: *Control, Automation and Systems (ICCAS), 2011 11th International Conference on*. 2011, pp. 643–648.

[195]   P.J. Sanz et al. "Recent progress in the RAUVI project: A Reconfigurable autonomous underwater vehicle for intervention". In: *ELMAR, 2010 Proceedings*. September. IEEE, 2010, pp. 471–474.

[196]   Pedro J. Sanz et al. "TRIDENT An European Project Targeted to Increase the Autonomy Levels for Underwater Intervention Missions". In: *2013 OCEANS - San Diego*. San Diego, CA: IEEE, 2013, p. 10.

[197]   Pedro J. Sanz et al. *TRIDENT: A framework for autonomous underwater intervention missions with dexterous manipulation capabilities*. Vol. 7. PART 1. IFAC, 2010, pp. 187–192.

[198]   Yoshiki Sato et al. "Autonomous docking of hovering type AUV to seafloor charging station based on acoustic and visual sensing". In: *2017 IEEE Underwater Technology (UT)*. IEEE, 2017, pp. 1–6.

[199]   Riccardo Scattolini. "Architectures for distributed and hierarchical Model Predictive Control - A review". In: *Journal of Process Control* 19.5 (2009), pp. 723–731.

[200]   I Schjølberg and TI Fossen. "Modelling and Control of Underwater Vehicle-Manipulator Systems". In: *in Proc. rd Conf. on Marine Craft maneuvering . . .* 1994 (1994).

[201]   Ingrid Schjølberg et al. "Next Generation Subsea Inspection, Maintenance and Repair Operations". In: *10th IFAC Conference on Control Applications in Marine Systems (CAMS 2016)*. Vol. 49. 23. Elsevier B.V., 2016, pp. 434–439.

[202]   Enrico Simetti et al. "Autonomous Underwater Intervention: Experimental Results of the MARIS Project". In: *IEEE Journal of Oceanic Engineering* 34.4 (2017), pp. 1–20.

[203]   H. Singh et al. "An integrated approach to multiple AUV communications, navigation and docking". In: *OCEANS 96 MTS/IEEE Conference Proceedings. The Coastal Ocean - Prospects for the 21st Century*. Vol. 1. IEEE, 1996, pp. 59–64.

[204] Hanumant Singh et al. "An intelligent dock for an autonomous ocean sampling network". In: *IEEE Oceanic Engineering Society. OCEANS'98. Conference Proceedings (Cat. No.98CH36259)*. Vol. 3. IEEE, 1998, pp. 1459–1462.

[205] P. Sotiropoulos et al. "AUV docking system for existing underwater control panel". In: *OCEANS 2009-EUROPE*. IEEE, May 2009, pp. 1–5.

[206] Milica Stojanovic and Pierre-Philippe J. Beaujean. "Acoustic Communication". In: *Springer Handbook of Ocean Engineering* (2016), pp. 359–386.

[207] R. Stokey et al. "A docking system for REMUS, an autonomous underwater vehicle". In: *Oceans '97. MTS/IEEE Conference Proceedings* 2 (1997), pp. 1132–1136.

[208] Roger Stokey et al. "Enabling technologies for REMUS docking: An integral component of an autonomous ocean-sampling network". In: *IEEE Journal of Oceanic Engineering* 26.4 (2001), pp. 487–497.

[209] Kasper Stoy, David Brandt, and David J Christensen. *Self-Reconfigurable Robots: An Introduction*. 1st ed. MIT Press, 2010.

[210] Donny Sutantyo et al. "Optical-guided autonomous docking method for underwater reconfigurable robot". In: *2013 IEEE Conference on Technologies for Practical Robot Applications (TePRA)*. IEEE, Apr. 2013, pp. 1–6.

[211] J. Sverdrup-Thygeson et al. "Modeling of underwater swimming manipulators". In: *10th IFAC Conference on Control Applications in Marine Systems CAMS 2016* 49.23 (2016), pp. 81–88.

[212] J. Sverdrup-Thygeson et al. "The underwater swimming manipulator - a bio-inspired AUV". In: *2016 IEEE/OES Autonomous Underwater Vehicles (AUV)*. IEEE, Nov. 2016, pp. 387–395.

[213] Jorgen Sverdrup-Thygeson et al. "The Underwater Swimming Manipulator—A Bioinspired Solution for Subsea Operations". In: *IEEE Journal of Oceanic Engineering* (2017), pp. 1–16.

[214] Mizuyo Takamatsu and Satoru Iwata. "Index reduction for differential-algebraic equations by substitution method". In: *Linear Algebra and Its Applications* 429.8-9 (2008), pp. 2268–2277.

[215] Herbert G. Tanner and Kostas J. Kyriakopoulos. "Mobile manipulator modeling with Kane's approach". In: *Robotica* 19.06 (2001), pp. 675–690.

[216] Tao Zhang et al. "AUV terminal docking experiments based on vision guidance". In: *OCEANS 2016 MTS/IEEE Monterey*. IEEE, Sept. 2016, pp. 1–5.

[217] T. J. Tarn, G. a. Shoults, and S. P. Yang. "A dynamic model of an underwater vehicle with a robotic manipulator using Kane's method". In: *Autonomous Robots* 3.2-3 (1996), pp. 269–283.

[218] Ken Teo, Edgar An, and Pierre Philippe J Beaujean. "A robust fuzzy autonomous underwater vehicle (AUV) docking approach for unknown current disturbances". In: *IEEE Journal of Oceanic Engineering* 37.2 (2012), pp. 143–155.

[219] Christoph Alexander Thieme and Ingrid Bouwer Utne. "A risk model for autonomous marine systems and operation focusing on human–autonomy collaboration". In: *Proceedings of the Institution of Mechanical Engineers, Part O: Journal of Risk and Reliability* 231.4 (2017), pp. 446–464.

[220] Christoph Alexander Thieme, Ingrid Bouwer Utne, and Ingrid Schjølberg. "A Risk Management Framework for Unmanned Underwater Vehicles Focusing on Human and Organizational Factors". In: *ASME 2015 34th International Conference on Ocean, Offshore and Arctic Engineering.* ASME, May 2015, V003T02A075.

[221] Goce Trajcevski et al. "Dynamics-aware similarity of moving objects trajectories". In: *Proceedings of the 15th annual ACM international symposium on Advances in geographic information systems - GIS '07* (2007), p. 1.

[222] Firdaus E. Udwadia and Phailaung Phohomsiri. "Explicit equations of motion for constrained mechanical systems with singular mass matrices and applications to multi-body dynamics". In: *Proceedings of the Royal Society A: Mathematical, Physical and Engineering Sciences* 462.January (2006), pp. 2097–2117.

[223] Firdaus E. Udwadia and Phailaung Phohomsiri. "Explicit Poincaré equations of motion for general constrained systems. Part I. Analytical results". In: *Proceedings of the Royal Society A: Mathematical, Physical and Engineering Sciences* 463.2082 (June 2007), pp. 1421–1434.

[224] Firdaus E. Udwadia and Phailaung Phohomsiri. "Explicit Poincaré equations of motion for general constrained systems. Part II. Applications to multi-body dynamics and nonlinear control". In: *Proceedings of the Royal Society A: Mathematical, Physical and Engineering Sciences* 463.2082 (2007), pp. 1435–1446.

[225] Firdaus E. Udwadia and Aaron D. Schutte. "A unified approach to rigid body rotational dynamics and control". In: *Proceedings of the Royal Society A: Mathematical, Physical and Engineering Science* 468.2138 (2012), pp. 395–414.

[226] Firdaus E. Udwadia and Aaron D. Schutte. "An Alternative Derivation of the Quaternion Equations of Motion for Rigid-Body Rotational Dynamics". In: *Journal of Applied Mechanics* 77.4 (2010), p. 044505.

[227] P Vaidya. "Prognosis - subsea oil and gas industry". In: *Annual Conference of thePrognostics and Health Management Society 2010* (2010), pp. 1–10.

[228] I. Vasilescu et al. "AMOUR V: A Hovering Energy Efficient Underwater Robot Capable of Dynamic Payloads". In: *The International Journal of Robotics Research* 29.5 (2010), pp. 547–570.

[229] I. Vasilescu et al. "Autonomous Modular Optical Underwater Robot (AMOUR) Design, Prototype and Feasibility Study". In: *Proceedings of the 2005 IEEE International Conference on Robotics and Automation.* IEEE, 2005, pp. 1603–1609.

[230] I. Vasilescu et al. "Data Collection, Storage, and Retrieval with an Underwater Sensor Network". In: *SenSys* (2005), pp. 154–165.

[231] Andreas Wächter and Lorenz T Biegler. "On the implementation of an interior-point filter line-search algorithm for large-scale nonlinear programming". In: *Mathematical Programming* 106.1 (Mar. 2006), pp. 25–57.

[232] Chao Wang et al. "Multi-LED parallel transmission for long distance underwater VLC system with one SPAD receiver". In: *Optics Communications* 410.November 2017 (2018), pp. 889–895.

[233] Avishai Weiss et al. "Model predictive control for spacecraft rendezvous and docking: Strategies for handling constraints and case studies". In: *IEEE Transactions on Control Systems Technology* 23.4 (2015), pp. 1638–1647.

[234] K.a. White et al. "Performance results of a fuzzy behavioral altitude flight controller and rendezvous and docking of an autonomous underwater vehicles with fuzzy control". In: *Proceedings of Symposium on Autonomous Underwater Vehicle Technology*. IEEE, 1996, pp. 117–124.

[235] Edmund Taylor Whittaker. *Treatise on the analytical dynamics of particles and rigid bodies; with an introduction to the problem of three bodies.* Vol. 1. Cambridge, University Press, 1917, p. 460.

[236] Philip a. Wilson. "Autonomous Homing and Docking Tasks for an Underwater Vehicle". In: *8th IFAC Conference on Manoeuvring and Control of Marine Craft* 42.18 (2009), pp. 304–309.

[237] Marius Wirtz, Marc Hildebrandt, and Christopher Gaudig. "Design and test of a robust docking system for hovering AUVs". In: *2012 Oceans*. IEEE, Oct. 2012, pp. 1–6.

[238] Marek Wojtyra and Janusz Fra-czek. "Solvability of reactions in rigid multibody systems with redundant nonholonomic constraints". In: *Multibody System Dynamics* 30.2 (2013), pp. 153–171.

[239] M. F. Yahya and M. R. Arshad. "Position-based visual servoing for underwater docking of an autonomous underwater vehicle". In: *2016 IEEE International Conference on Underwater System Technology: Theory and Applications (USYS)*. IEEE, 2016, pp. 121–126.

[240] Yang Ke et al. "A Dynamic Model of ROV with a Robotic Manipulator Using Kane's Method". In: *2013 Fifth International Conference on Measuring Technology and Mechatronics Automation* (2013), pp. 9–12.

[241] Ke Yang et al. "A dynamic model of an underwater quadruped walking robot using Kane's method". In: *Journal of Shanghai Jiaotong University (Science)* 19.2 (2014), pp. 160–168.

[242] Ke Yang et al. "Dynamic model of underwater snake-like robot using Kane's method". In: *Journal of Shanghai Jiaotong University (Science)* 19.2 (2014), pp. 146–154.

[243] Zhaoquan Zeng et al. "A Survey of Underwater Optical Wireless Communications". In: *IEEE Communications Surveys & Tutorials* 19.1 (2017), pp. 204–238. arXiv: arXiv:1011.1669v3.

[244]   Zhang Zhang, Kaiqi Huang, and Tieniu Tan. "Comparison of similarity mea-sures for trajectory clustering in outdoor surveillance scenes". In: *Proceedings - International Conference on Pattern Recognition* 3 (2006), pp. 1135–1138.